1-1-2018

Complex Network Analysis for Early Detection of Failure Mechanisms in Resilient Bio-Structures

Reena R. Patel

Complex network analysis for early detection of failure mechanisms in resilient bio-structures

By

Reena R. Patel

A Dissertation
Submitted to the Faculty of
Mississippi State University
in Partial Fulfillment of the Requirements
for the Degree of Doctor of Philosophy
in Computational Engineering
in the Bagley College of Engineering

Mississippi State, Mississippi

December 2018

Complex network analysis for early detection of failure mechanisms in resilient bio-structures

By

Reena R. Patel

Approved:

David S. Thompson
(Major Professor)

Guillermo A. Riveros
(Committee Member)

Edward A. Luke
(Committee Member)

Hongjoo Rhee
(Committee Member)

Hyeona Lim
(Committee Member)

Manav Bhatia
(Graduate Coordinator)

Jason M. Keith
Dean
Bagley College of Engineering

Name: Reena R. Patel

Date of Degree: December 14, 2018

Institution: Mississippi State University

Major Field: Computational Engineering

Major Professor: Dr. David S. Thompson

Title of Study: Complex network analysis for early detection of failure mechanisms in resilient bio-structures

Pages of Study: 167

Candidate for Degree of Doctor of Philosophy

Bio-structures owe their remarkable mechanical properties to their hierarchical geometrical arrangement as well as heterogeneous material properties. This dissertation presents an integrated, interdisciplinary approach that employs computational mechanics combined with flow network analysis to gain fundamental insights into the failure mechanisms of high performance, light-weight, structured composites by examining the stress flow patterns formed in the nascent stages of loading for the rostrum of the paddlefish. The data required for the flow network analysis was generated from the finite element analysis of the rostrum. The flow network was weighted based on the parameter of interest, which is stress in the current study. The changing kinematics of the structural system was provided as input to the algorithm that computes the minimum-cut of the flow network. The proposed approach was verified using two classical problems three- and four-point bending of a simply-supported concrete beam. The current study also addresses the methodology used to prepare data in an appropriate format for a seamless transition from finite element

binary database files to the abstract mathematical domain needed for the network flow analysis. A robust, platform-independent procedure was developed that efficiently handles the large datasets produced by the finite element simulations. Results from computational mechanics using Abaqus and complex network analysis are presented. The complex network strategy successfully identified failure mechanisms in the bio-structure by identifying strain localization in regions of tension, and buckling/crushing in regions of compression. The transdisciplinary strategy used in this study identified the failure mechanisms early, when the material was still in the linearly elastic regime, thereby tremendously reducing the computational time and cost as compared to running a finite element analysis to failure. This work also developed five proof-of-concept, bio-inspired models with varying lattice complexity based on the rostrum. Performance of these bio-inspired models was analyzed with respect to the stress and deformation. Numerical experiments were carried out on one of the bio-inspired model to demonstrate the application of newly developed similitude laws for blast loading. This research has laid the groundwork for an efficient design-test-build cycle for rapid prototyping of novel bio-inspired structures by using flow network analysis, finite element analysis, and similitude laws.

Key words: bio-structure, biomimicry, rostrum, paddlefish, flow network, finite element

DEDICATION

To my husband, Rujul, for teaching me the logic behind programming and his invariable support, and my kids, Rishan and Raeya, for sharing their mother with her research! Also to my Father, Ravindrakumar, and Father-in-law, Manharlal, for believing that I could... I couldn't have done this without you. Thank you for all your support along the way.

ACKNOWLEDGEMENTS

Firstly, I would like to thank my family and friends for always being there for me in this long journey. Secondly, and most importantly, I would like to thank the U. S. Army Engineer Research and Development Center (ERDC) Long Term Training program for providing me the opportunity to pursue my dream! The support provided by the ERDC family in general during the entire process has been greatly appreciated. The encouraging words of wisdom by coworkers kept me going. I sincerely thank my advisor, Dr. David S. Thompson, for his continuous support, patience, enthusiasm, and immense knowledge throughout this research. His guidance helped me develop a good work ethic and settle for nothing but the BEST. My most sincere thanks goes to my co-advisor and mentor, Dr. Guillermo A. Riveros. His guidance motivated me not only in the research process, but also in obtaining financial support for this research work. Dr. Riveros's ability to discuss and ask questions every day is unquestionable! I would particularly like to thank Ms. Indu Shukla, Dr. Bela Soni, and Dr. Mihan McKenna for their continuous support and encouragment. The idea for this research was developed from long conversations with Dr. John F. Peters, which led me to attend the presentation given by Dr. Tordesillas during her 2015 visit to ERDC. The flow network part of the research was a result of interactions with Dr. Peters, Dr. Riveros, and Dr. Tordesillas.

I would also like to thank my committee for their insightful comments, encouragement, and questions on this dissertation.

This work was financially supported by the by U.S. Army Engineer Research and Development Center (ERDC) under PE 0601102, Project T22 "Research in Soil and Rock Mechanics", Task 01, and the Information Technology Laboratory. The support and resources from the ERDC Department of Defense Supercomputing Resource Center, under the subproject Environmental Quality Modeling and Simulation are gratefully acknowledged. The findings and opinions in this dissertation belong solely to the author, and are not necessarily those of the sponsor.

TABLE OF CONTENTS

LIST OF TABLES

LIST OF FIGURES

LIST OF SYMBOLS, ABBREVIATIONS, AND NOMENCLATURE

$Paddlefish$ The American paddlefish (Polyodon spathula) is a species of basal ray-finned fish closely related to sturgeons in the order Acipenseriformes.

$Rostrum$ Some fish have permanently protruding rostrums which evolved from their upper jawbones. Paddlefish, goblin sharks and hammerhead sharks have rostrums packed with electroreceptors which signal the presence of prey by detecting weak electrical fields.

t target node

s source node

$G(V, E)$ Flow network graph, V and E represent vertices and edges of the graph

(u, v) Arc of a flow network graph

C capacity of an edge of the flow network graph

E Young's modulus

S scale factor

TNT Trinitrotoulene

σ stress or pressure

ϵ strain

ρ density

v velocity

A acceleration

U displacement

e energy

m, M mass

F force

t time

d deformation

I cross sectional moment of intertia

$MassDensity$ Mass per unit volume

σ_{vm} Von-Mises stress

$\sigma_{xx}, \sigma_{yy}, \sigma_{zz}$ normal stress component

$\tau_{xy}, \tau_{yz}, \tau_{zx}$ shear stress component

FEM Finite element method

$MFMC$ Maximum-flow/minimum-cut

DOF degrees of freedom

CT X-ray computed tomography

CHAPTER I

INTRODUCTION

Life has evolved from a single cell to complex biomolecules through the process of evolution based on functional needs. A distinguishing feature that is prevalent in bio-structures is their unique hierarchical architecture, which imparts superior characteristics such as strength, toughness, low weight, etc. As compared to more complex, man-made materials, bio-structures are constructed from the simplest building blocks available in nature. Looking at nature from an engineers eye and reverse engineering the superior attributes of bio-structures may help to develop structural designs possessing broader use limits in a variety of application areas [4]. For example, the teeth of piranha have exceptional ability to cut through flesh. Meyers et al. proposed the design of a scissor inspired from the teeth of piranha [5]. The design of shock absorbers has been inspired by the head of woodpecker [6].

This research proposes to gain fundamental insight into the design and engineering of high performance, lightweight, structured composites by examining the geometrical and material properties of the paddlefish nose or rostrum (Figure 1.1). The motivation behind this research effort is an earlier feasibility study that concluded that the non-uniform geometry of the rostrum is a natural toughening mechanism used to mitigate failure [7].

The rostrum exhibited better energy dissipation and load bearing capacity when compared to a homogenous material with a similar geometry. The rostrum of the paddlefish has a lattice-like, bone structure embedded in soft tissue that appears to contribute to its unique strength and resilience. A fundamental understanding of how this lattice-like architecture functions has the potential to provide novel insights into applications over a wide range of disciplines. This work addresses the emergent need to develop new material designs that are strong, tough, lightweight, and energy dissipative that can be used to protect and support rapid deployment of the warfighter. Possible applications include protective panels, novel building materials, body and vehicle armor, and ship design among others.

Figure 1.1

Paddlefish (Public domain image from Wikipedia)

1.1 Paddlefish

The paddlefish (Polyondon spathula) can be easily distinguished by the presence of an elongated rostrum as seen in Figure 1.2. It is among the most primitive of bony-finned fishes (Osteichthyes, Actinopterygil) and, together with sturgeon, comprises an order of secondary cartilaginous fishes, the Acipenseriformes [8]. They were once abundant in most central US river systems. Their population decline is attributed to habitat loss and degradation, and overharvest [9]. They are commercially exploited for their eggs, or roe (caviar) [10–12]. Additionally, sedimentation and river modification are other reasons for their declining population. Paddlefish are extremely mobile and have been known to travel more than 200 miles in river systems [13]. Figure 1.3 displays the population distribution of paddlefish as of 2009 [1].

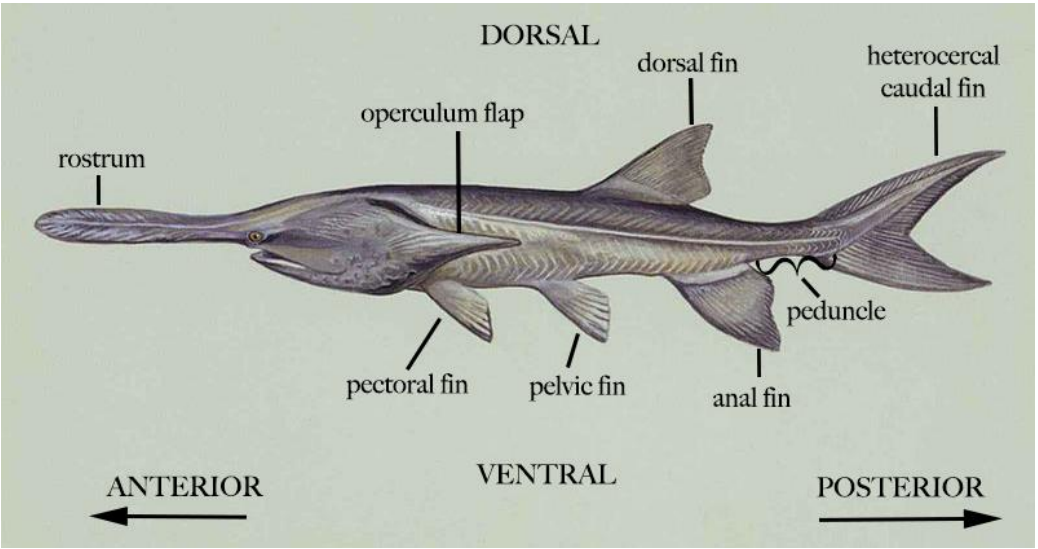

Figure 1.2

General morphology of the American paddlefish (By Atsme - Own work, CC0, https://commons.wikimedia.org/w/index.php?curid=36033611)

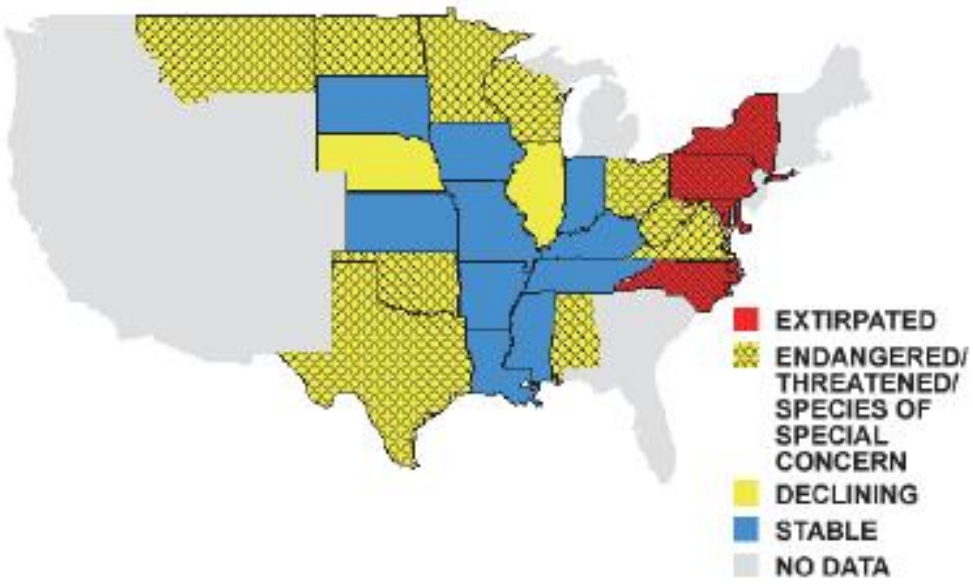

Figure 1.3

Paddlefish population distribution [1]

1.2 Rostrum Characteristics

Many biological structures have a complex interplay between intricate geometry and heterogeneous materials [14, 15] that produces uncertainty as to what is dictating the structural response. For example, the rostrum of the paddlefish is a unique structure comprised of a network of tissue, cartilage, and interlocking star-shaped bones called stellate bones. Figure 1.4 displays the stellate bone arrangement in the rostrum of the paddlefish. Figure 1.5 (a) displays the outer soft tissue layer of the rostrum. Figure 1.5 (b) shows the cross section of the rostrum highlighting its three components. Figure 1.5 (c) shows the inner hard cartilage of the rostrum, which has an elastic modulus of an order of magnitude stiffer than the tissue. Figure 1.5 (d) shows the inner soft cartilage of the rostrum whose elastic

modulus is an order of magnitude softer than the hard cartilage. As displayed in Figure 1.5, the rostrum is characterized by a hierarchical geometrical lattice architecture and varying material properties.

1.3 Rostrum function

Early researchers believed that the rostrum was used to dig for food [16–21] or remove organisms from vegetation [22, 23]. This theory was put aside when paddlefish were found to be filter feeders [24, 25]. In fact, the rostrum serves multiple functions depending on the age of the fish. In the juvenile stage, the shape of the rostrum is linear and is almost one-third of the body length. The primary function of the rostrum at the juvenile stage is sensory. Paddlefish have been known to swim and feed efficiently in both laminar and turbulent flows. This has been attributed to their ability to detect the type of flow owing to the sensory function of the rostrum [26]. The sensory function also aids in the detection of tiny zooplankton without the need for sight [27]. Additionally, paddlefish make feeding strikes at dipoles in response to weak low-frequency electrical currents [28]. During the sub-adult stage, the shape of the rostrum is spatulate and its primary function is hydrodynamic. During this stage, the paddlefish are active filter feeders. During filter feeding, paddlefish take an enormous amounts of water while swimming with their mouths wide open. The gill rakers, which are composed of extensive comb-like filaments, assist in filtering the tiny zooplankton from the water. Paddlefish swim faster during filter feeding and use the forward body velocity to transport water at high speed to filter food quickly and efficiently. Adult paddlefish may be able to survive without the rostrum, but they feed less efficiently

Figure 1.4

Paddlefish rostrum and stellate bone arrangement
(http://www.lmrcc.org/paddlefish-primitive-fish-inspiring-future-technology/)

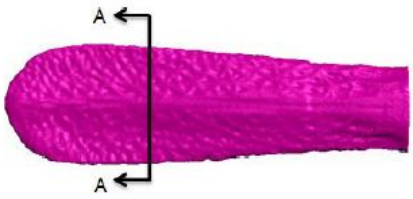

(a) Tissue

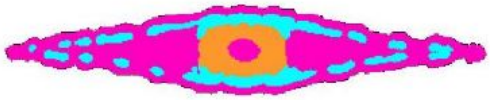

(b) Cross-section (A-A, displayed in Figure 2(a)) of rostrum displaying three parts

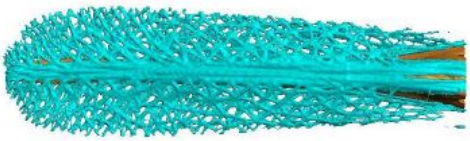

(c) Hard cartilage

(d) Soft cartilage

Figure 1.5

Components of rostrum

and are comparatively thinner. Figure 1.6 shows a paddlefish with rostrum injuries [10]. The size, shape, and position of rostrum assist in generating lift [29]. When paddlefish filter feed, the additional weight of the water would pose stability issues in absence of the lift generated by the rostrum. In the adult stage, the shape of the rostrum is linear and the primary function is mechanical.

1.4 Research hypothesis

In order to understand the superior performance of the rostrum, it is essential to identify the failure mechanisms at early stages of loading when the material is in the linearly elastic regime. The hypothesis of this research are described below.

Figure 1.6

Rostrum injuries [2]

1.4.1 Hypothesis-1

The rostrum is resilient because of enhanced toughening mechanisms. The toughening mechanisms in the rostrum may be attributed to the complex arrangement of lattice (fractal-like) skeletal structure. By using the flow network approach, the failure mechanisms in the rostrum's complex geometry can be identified earlier when the material is still in the linearly elastic regime.

This research hypothesis will be tested using computational mechanics experiments that employ explicit formulations on models that are constructed from higher-order finite elements with millions of degrees of freedom. Although finite element simulations provide the overall distribution of stresses in the system, the underlying kinematics that governs the formation of the strong and weak links in the system are hard to identify. This research will investigate the emergent failure resistant mechanisms of the rostrum. Because of the complex nature of the biological structure, a novel transdisciplinary research approach is required to gain fundamental understanding of the role of the lattice structure in resilient bio-structures. To fully understand the effect of local topological interaction on the global structural response of the system at the onset of loading, the model will be formulated as a network flow problem. The theoretical approach proposed in this research will be validated using analytical experiments on classical engineering problems for which the solution is known, i.e., three- and four-point bending on a simply-supported concrete beam.

1.4.2 Hypothesis-2

If the failure mechanisms of the lattice-based, bio-structural systems are dependent on their geometrical arrangements, then structures with more complex geometries will be more resilient than structures with lower complexity.

To test this hypothesis, finite element experiments were carried out on conceptual prototypes of bio-inspired, mechanical system models with different lattice patterns based on the rostrum of the paddlefish. The performance of the bio-inspired structural systems were quantified in terms of deformation and stresses.

1.5 Research objectives

Based on the research hypothesis the objectives of the current research work are as follows:

1. Conduct finite element analysis on the rostrum using the commercial software Abaqus to study the effect of changing displacement boundary conditions. The models for the finite element analysis were developed from computerized tomography (CT) scans.
2. Formulate the rostrum as a network flow problem from the nodes and connectivity information obtained from the finite element analysis. Verify the flow network approach using two classical problems, i.e., three- and four-point bending of a simply-supported concrete beam. Demonstrate the use of the flow network approach for early detection of failure mechanisms when the rostrum is subjected to an external loading condition.
3. Analyze the stress and deformations experienced by notional bio-inspired structural systems developed based on the rostrum. The stress and deformations are obtained from the finite element analysis conducted on the bio-inspired structural systems.
4. Use the Buckingham *Pi* theorem to develop a set of non-dimensional *Pi* terms to scale the model to larger size and provide mathematical relations for scaling. Demonstrate the use of the non-dimensional Pi terms for one of the bio-inspired structural systems.

1.6 Significant contributions

The following are the novel contributions of this research:

1. Insight was gained into the phenomena of failure mechanisms in bio-structures as they are subjected to external load using a state of the art transdisciplinary approach. Although significant research has been conducted on bio-structures, there is still a lack of knowledge on what contributes to that superior performance. This research has identified the failure patterns in bio-structure in the nascent stages of loading when the material is still in the linearly elastic regime. A significant contribution of this research is to gain insight into the phenomena of failure mechanisms in bio-structures as they are subjected to external load using a state of the art transdisciplinary approach.

2. The new methodolody has successfully identified strain localization in tensile regions, and buckling/crushing in compressive regions for the model of the rostrum. Additionally the flow network approach was able to identify the failure sites as the locations where the material and geometry of the structural system changes, i.e., high stress concentration regions. This knowledge may lead to development of superior bio-inspired structural systems.

3. The strategy developed using the Buckingham *Pi* theorem will provide the foundation for using different materials for mimicking the resiliency of bio-structures.

4. The developed methodology identifies the failure site earlier and does not require running non-linear finite element analyses to failure or the use of complex damage models. Hence, this new methodology will result in a reduction of computational cost, time, and complexity for an efficient design-test-build cycle for rapid prototyping of bio-inspired models.

1.7 Publications and presentations

The findings of the proposed research were disseminated in the publications and presentations listed below:

1.7.1 Publications

1. R. R. Patel, G. A. Riveros, D. S. Thompson, F. J. Acosta, C. Colon, E. J. Perkins, J. J. Hoover, J. F. Peters, *Performance analysis of resilient bioinspired structural systems*, Proc. SPIE 10593, Bioinspiration, Biomimetics, and Bioreplication VIII, 105930J (27 March 2018); https://doi.org/10.1117/12.2295941.

2. R. R. Patel, G. A. Riveros, D. S. Thompson ,J. J. Hoover, E. J. Perkins, J. F. Peters, A. Tordesillas, *Early detection of failure mechanisms in resilient bio-structures: A complex network study*, ERDC-TR-17-11, 01 October 2017.

3. R. R. Patel, D. Valles, G. A. Riveros, D. S. Thompson, E. J. Perkins, J. J. Hoover, J. F. Peters, A. Tordesillas, *Stress flow analysis of bio-structures using finite element method and flow network approach*, Finite Elements in Analysis and Design (in press).

4. R. R. Patel, D. S. Thompson, G. A. Riveros, J. F. Peters, *Dimensional analysis for impact response of Bio-structures (Rostrum of Polyodon Spathula (Paddlefish)) through application of Buckingham Pi theorem*, Mathematics and Computers in Simulation (in review).

5. R. R. Patel, G. A. Riveros, D. S. Thompson, E. J. Perkins, J. J. Hoover, J. F. Peters, A. Tordesillas, *A transdisciplinary approach for analyzing stress flow patterns in bio-structures*, SIAM Journal of Applied Mathematics (in review).

1.7.2 Presentations

1. R. R. Patel, G. A. Riveros, D. S. Thompson, F. J. Acosta, C. Colon, E. J. Perkins, J. J. Hoover, *Performance Analysis of Resilient Bioinspired Structural Systems*, SPIE 2018, Denver, CO, March 6 2018.

2. Presented a seminar to the faculty and graduate students from Mathematics, Engineering, Physics, and Biology departments at Colorado State University, Fort Collins, CO, March 7 2018.

3. R. R. Patel, G. A. Riveros, D. S. Thompson, F. J. Acosta, E. J. Perkins, J. J. Hoover, J. F. Peters and A. Tordesillas, *A transdisciplinary approach to identify stress flow patterns in resilient bio-structures*, RD18, Vicksburg, MS, May 2018.

4. R. R. Patel, G. A. Riveros, D. S. Thompson, F. J. Acosta, C. Colon, E. J. Perkins, J. J. Hoover, *Computational Mechanics Analysis of High Performance Bio-inspired structures*, 82nd Annual meeting of The Mississippi Academy of Sciences, Hattiesburg, MS, 22-23 February 2018.

5. R. R. Patel, G. A. Riveros, D. S. Thompson, *Fundamentals of load transfer mechanisms in bio-structures: A Complex Network Approach* , Poster and oral presentation at The Mississippi Academy of Sciences 79th Annual meeting, Hattiesburg, MS, 23-24 February 2017 .

6. Technical presentation at the American Society of Civil Engineers Vicksburg branch meeting, June 7, 2017.

7. R. R. Patel, G. A. Riveros, D. S. Thompson, *Load transfer mechanisms of bio-structures: A complex network approach*, 33rd Annual Southern Biomedical Engineering Conference, Gulfport, MS, 17-19 March 2017.

8. Technical presentation at the Army User Group Review in Vicksburg, MS, August 2016.

9. R. R. Patel, G. A. Riveros, J. J. Hoover, E. J. Perkins, D. S. Thompson, *Early detection of failure mechanisms in resilient bio-structures: A complex network study* SIAM Workshop on Network Science, Boston, MA, 15-16 July 2016.

1.8 Dissertation outline

An in-depth literature review is presented that focuses on structural hierarchy in nature, application of flow network, computational mechanics experiments on bioinspired structural systems, scaling of bio-inspired hierarchical structures using the concepts of dimensional analysis and similutide, and the previous research conducted on the rostrum of the paddlefish. The approach developed for early detection of failure mechanisms is discused along with details of the flow network analysis and implementation of the methodology. This approach was verified using two classical problems for which the solutions are known. Results obtained by implementing the flow network approach on the rostrum are presented. A performance evaluation of the platform independent software developed for implementing the research approach is also discussed. The Results chapter demonstrates the use of the flow network approach on the rostrum to identify failure mechanisms by indentifying strain localization in regions of tension, and buckling/crushing in regions of compression. A performance evaluation of five bio-inspired models is presented using stress and deformation as metrics. Also included is the application of similitude laws for blast loading on one of the bio-inspired models. The appendix demonstrates the application of similitude

laws to represent the deformation of a structure in response to a blast load in terms of non-dimensional Pi terms by application of the Buckingham Pi theorem.

CHAPTER II

LITERATURE REVIEW

The field of bio-inspired material design is fairly young and largely unexploited. Nature has optimized complex bio-structures over billions of years to have remarkable resiliency, strength, and lightweight composition. This chapter provides an in-depth literature review of structural hierarchy in nature with an example on how design of a prominent structure is inspired from a bio-structure. An overview of flow networks and their current use in multiple application areas is provided since this research uses them to identify stress flow patterns in a resilient bio-structure.

2.1 Structural Hierarchy in Nature

Nature has progressed from a simple cell to complex organisms through evolution. The resulting natural bio-structures have acquired unique strength and multi-function capabilities through exposure to dynamic forces. Biological structural systems are made from the simplest chemical building blocks available in nature and achieve their optimal state as an evolutionary response to being subjected to variable loading conditions. They are of interest for engineering applications because of their superior mechanical performance [30]. Additionally, they provide a wide platform for biomimicry for the purpose of designing new materials [31, 32].

Scientist and engineers have often taken inspiration from nature to generate sophisticated solutions to engineering problems. Alexandre Gustave Eiffel utilized the enormous load bearing capacity of the femur bone and the stability it provides for the design of the Eiffel tower [33, 34]. It is a classic example of optimization of strength and weight. In an attempt to gain insights for designing advanced structural materials with enhanced flexural behavior, Meisam et al. [35] studied the asymmetric flexural response of bamboo under various loading conditions. The superior mechanical properties of bamboo were attributed to its unique functionally-graded hierarchical structure. Bargmann et al. [36] analyzed the mechanical behavior of hierarchical bovine dental structure. Dental enamel is a load bearing natural bio-composite that has evolved to resist fracture and wear. The most remarkable property of enamel is its longevity in the presence of cracks in spite of its high mineral content. This highly mineralized tissue avoids brittleness because of its hierarchical structure and its nanocomposite nature comprising of soft organic matter [37]. Analysis of the structural-mechanical properties of enamel could lead to improved choices for dental restoratives [38] or the development of body armor [37]. Burns et al. [39] mimicked the hierarchical design of the structural joints found in trees across multiple length scales bridging both the laminate and structural properties of fiber-reinforced composite materials for aerospace applications. Although some of the wood ingredients (e.g., lignin and hemi-cellulose) are brittle, the tree branch-trunk connections have numerous vital design features that deliver high strength and toughness [40–42]. They created a composite T-joint based on inspiration from tree branch joints by integrating laminate-level and structural design concepts into a single design. This bio-inspired composite T-joint resulted in

tensile strength enhancement as compared to a conventionally designed T-joint. Johnson et al. [43] conducted numerical simulations of bio-inspired, nacre-like composite plates. Nacre, found in mollusk shells, is a biological material that demonstrates exceptional mechanical properties owing to its complex hierarchical structure systematized over numerous length scales [44,45]. Johnson and coworkers [43] observed improved performance of nacre-like plates as compared to standard bulk plates under a blast loading. Tran et al. [46] demonstrated that a square, bio-inspired composite plate based on the nacre structure could be utilized to improve the blast response of glass fibre/vinylester resin composites exposed to underwater impulsive loading. They found that the bio-inspired composite structure relieved the stress concentration by spreading out the damage over a large area.

2.2 Flow Networks

Flow networks can be used to study processes in physical, biological, social, and information systems. Almost any problem that has a flow of information can be represented in terms of a flow network. The flow of stresses in a structural system can be interpreted as a flow network, which can facilitate the investigation of questions about failure mechanisms. The flow of information at a given point in the system is the rate at which the information (i.e., variables such as stresses, displacements, kinetic energy, elastic or plastic strain in the structural system) travels. In computer science, flow networks can be used to represent communication networks, data organization, the flow of computation, etc. Flow networks have been used to examine interactions within various complex systems such as traffic flow, energy flow through food webs in an ecosystem, fluid or gas flow through pipelines, infor-

mation flow through communication networks, current flow through electrical networks, etc.

A flow network was first used in 1930 to analyze the Russian railway system [47]. During the cold war, the US military was interested in finding the minimum number of locations that the railway system could be disrupted that would prevent movement between the Soviet Union and Eastern Europe [47]. Vitali et al. [48] utilized flow networks to analyze the community structure of company ownership and control. Their work reveals the worldwide structure of corporate control. Barrat et al. [49] focused on scientific collaboration networks and the world-wide air-transportation network, which are examples of social and large infrastructure systems, respectively. Their work provides an enhanced explanation of the hierarchies and organizational principles using the architecture of weighted networks and delivers a quantitative and broad methodology to comprehend the complex architecture of real weighted networks. Bullmore et al. [50] reviewed several studies that analyzed the behavior of complex brain networks. Their work highlights the key concepts and technical challenges in this rapidly developing field. Dewil et al. [51] showed how the maximum covering and patrol routing problem can be modeled as a minimum cost network flow problem. A classic routine for state troopers is to patrol the locations that are prone to crashes. Additionally, these sensitive locations are only active during particular time frames. Owing to the limited availability of resources, these locations cannot be patrolled at all times. Hence, an optimization problem that routes patrol cars in a manner that maximizes the coverage of such sensitive areas appears to be appropriate [52]. It is advantageous to have an efficient and effective solution methodology to solve the maximum

covering and patrol routing problem since this problem frequently appears as a subproblem in larger problems.

Numerous studies have focused on the mechanical response of granular material subjected to stresses and strains [53]. The transmission of forces in granular material occurs through a network of inter-grain contacts. This contact network is dual natured, one being strong and the other being weak [54, 55]. The process by which the material selects which particles belong to the strong and weak force chains is unclear [56]. Lin and Tordesillas [57] have utilized the concepts and techniques of network optimization theory in order to acquire an enhanced knowledge of force transmission in dense granular materials. They analyzed the behavior of a deforming granular material under the application of a quasi-static biaxial compression loading at different stages. The changing kinematics of the system at the different stages were studied by representing them as flow networks. The flow networks constructed from the evolving network of grain contacts were analyzed via the maximum flow problem and the minimum-cost/maximum-flow problem. This study identified the flow bottlenecks and also established a necessary and sufficient condition for the minimum cut of the maximum flow to be unique. The bottlenecks in the flow network develop in proximity to the persistent shear band, which is a widely studied phenomenon in dense granular materials. As the grains rearrange under the application of a quasi-static loading, some contacts break and new contacts are formed. A thorough analysis of the complex contact networks at the various equilibrium states of the loading history is conducted to determine the extent to which force transmission is optimized in a granular

system. Lin and Tordesillas [57] attempt to uncover and understand what quantity is being optimized (if any) when the material deforms and its constituent particles are rearranged.

2.3 Computational mechanics experiments on bio-inspired, high performance structural systems

Owing to its phenomenal development, virtual engineering has emerged as a promising field that helps to ensure that a product performs as designed under realistic conditions. In the field of engineering, computational mechanics experiments are generally performed using finite element computer programs (e.g. Simulia, Nastran, Ansys, Adina, etc.) Computational mechanics experiments assist in developing a fundamental understanding of progressively complex problems with increasing accuracy. Numerous "what if" scenarios can be simulated at a fraction of the cost that would be required to perform scaled physical experiments. Civil and marine applications require the design of lightweight, high-performance materials that can withstand high impulsive loading conditions [46]. Tran et al. [46] performed a finite element, fluid-structure interaction simulation to analyze the failure of monolithic composite panels subjected to impact loading conditions. Their numerical study compared the performance of a baseline composite panel to a bio-inspired design with respect to total deformation and composite damage. Tran et al. utilized the commercial finite element code Abaqus/Explicit to carry out their numerical analysis. Their analysis provided insight and guidelines for future work on manufacturing bio-inspired, high performance composite panels for protection and demonstrated that the bio-inspired composite structure helps to relieve stress concentrations by spreading the induced damage over large areas. This performance enhancement was acquired through

introduction of layer waviness to one of the in-plane directions with a triangular wave function.

Wei et al. [58] performed fluid-structure interaction simulations to simulate scale experiments [59]. Their work focused on gaining insights into the deformation and failure mechanisms of monolithic as well as sandwich composite panels. Their model was able to calculate deformation histories, fiber/matrix damage patterns, and inter-lamina delamination in both monolithic and sandwich composite panels. Furthermore, their numerical results compared well with scale experiments [59]. Flores et al. [60] conducted a multi-scale, finite element analysis of a novel material inspired by the mechanics and structure of wood cell-walls. The overall constitutive behavior of the alumina/magnesium alloy fiber was modelled as a single material defined by a large number of representative volume elements. Their numerical experiments indicated that the new composite displays enhanced toughness when the hierarchical design of wood cells was utilized. This research provides insights into how trees and plants optimize their microstructures at the cellulose level so as to absorb a large amount of strain energy prior to failure.

Vernery et al. [61] developed a computational framework to establish a relationship between structure and the overall mechanical response of bio-inspired flexible composites. Their study analyzed fish skin that possessed desirable mechanical properties like compliance, resistance to penetration, lightweight, etc. Individual fish scales have a tendency to resist penetration thereby providing a physical barrier against predator attacks. Also, the organization of the fish scales at larger length scales delivers a skin that provides flexibility for swimming. These attributes are highly desired for the next generation of body

armor. The equations derived from this work were utilized to gain insight into the non-linear response of the fish skin. They observed a highly anisotropic bending and torsional response of the fish skin during indentation tests and swimming. The authors pointed out that novel scaled structures developed using fish skin will have a broad spectrum of applications ranging from ultra-light and flexible armor systems to important future technological developments comprising flexible electronics or the design of smart and adaptive morphing structures for aerospace applications. Johnson et al [43] carried out a numerical investigation of nacre-like composite plates under blast loading. Their numerical study identified a significant improvement in blast resistance performance of nacre-like plates as compared to bulk plates. Moreover, a reduction in peak velocity and maximum deflection of the back face was witnessed for nacre-like plates. The superior performance of nacre-like plates was attributed to their hierarchical structure, which facilitates a globalized energy absorption by interlayered interlocking and delamination.

2.4 Scaling Bio-Inspired Hierarchical Structures

Scientists and engineers are often posed with the challenge of replicating the behavior of a system at a different length scale because of customer requirements or design parameters. The structural hierarchy observed in a natural material is built via a bottom up approach, which makes it difficult to replicate in large-scale manufacturing [62]. Moreover, natural materials are made from weak/fragile components, but exhibit remarkably high levels of toughness and strength. This advantage has generated considerable interest in research centering on bio-inspired materials. Biological materials often perform multiple

functions. They are a result of combined biological, mechanical and other processes and represent a local optimization with respect to a set of design requirements and constraints. Pugno's [63] work on scaling up the adhesion characteristics of a spider to the size of a human gives a very interesting example illustrating the power of utilizing biomimetics at larger scales. This study utilized a mathematical formulation for optimizing the laws that govern adhesion to develop a plausible solution for the attachment/detachment phenomena required for developing Spiderman gloves. Pugno's work highlights the fact that instead of mimicking nature, the focus must be getting inspiration from nature.

Another interesting application is presented in the work of Menon and Sitti [64] in which two climbing robots were designed based on inspiration derived from the climbing abilities of the gecko. The first robot was designed for macro-scale application areas on Earth as well as space. The second robot is based on microscopic-scale application areas. Through the application of compliant micro/nano-scale, high aspect ratio beta-keratin structures on their feet, geckos efficiently climb any surface with a controlled area [65]. This work is a classic example of utilizing hierarchical structures to fit application areas by scaling the design parameters required for manufacturing the product.

2.4.1 Dimensional Analysis

One of the elementary methodologies that is valuable in the preliminary stages of modeling a problem is the investigation of the appropriate quantities upon which the problem is dependent and the manner in which they are dimensionally related [66]. The principles of dimensional analysis were properly recognized in the early 20th century by the formal

proof of the Buckingham Pi theorem [67]. Simply stated, equations must be dimensionally homogeneous, i.e., an equation must have balanced units. This observation forms the basis of dimensional analysis. It provides an elegant platform to understand physical data without taking into consideration the dimensions thereby enabling the user to deduce how a scaled system will behave. Matuszak's [68] work focused on dimensional analysis for different sets of problems that highlight the principles of dimensional analysis, transforming equations to a dimensionless form, analyzing equations derived from experiments, and identifying the limitations of equations in dimensionless form. Traditionally, dimensional analysis was primarily used for experimental research. The scope of this technique has broadened to include the analysis of model equations. A complex problem is dependent on a number of variables and parameters. As the number of parameters and the dependencies grow, it becomes a challenge to track the dependence on parameters and properties. Dimensional analysis simplifies this process by reducing the number of independent variables through the appropriate selection of non-dimensional groups..

The flavor and power of this tool can be seen in the calculations made by the British applied mathematician G. I. Taylor in the late 1940s to estimate the yield of the first atomic explosion [66], which was classified information, using photographs of the blast in conjunction with dimensional analysis. Carpenteri et al. [69] employed dimensional analysis in their work on crack propagation in concrete. These derived scaling laws can help engineers gain an understanding on how size and material property variations impact crack growth. Clayton's work [70] utilizes dimensional analysis to lay a foundation that provides a systematized structure for organizing and comparing future multiscale simulations and

validation experiments. Clayton efficiently used the principles of dimensional analysis to analyze the ballistic penetration resistance of ceramic materials using the datasets from six independent experimental studies. The technique of dimensional analysis also provides a means for developing the equations of the problem under study as seen in Zong et al. [71]. Their work utilized dimensional analysis to formulate two equations for calculating the head loss in self-cleaning screen filters in drip irrigation systems when tap and sand water mixtures were used. Eleven parameters that impacted the head loss were used in their analysis. Buckingham's technique was used to represent these parameters as eight dimensionless groups. The resulting equations were calibrated using experimental data. The authors reported that the equations developed from this study provided good predictions as compared to other similar equations found in the literature.

2.4.2 Similitude

The theory of similitude has been employed extensively for testing engineering models. A model and prototype are said to have similitude if they have the geometric similarity, kinematic similarity and dynamic similarity [66]. Two objects are geometrically similar if they have the same shape. They may not be the same size, but one can be obtained from the other by either enlarging or reducing. Kinematic similarity is achieved when the fluid streamlines around the prototype and the scaled model are geometrically similar. Dynamic similarity requires the ratios of all forces acting on the fluid particles and boundary surfaces for the protype and the scaled model be constant. Figure 2.1 displays the three conditions required for a model to have similitude with a prototype. Hydraulics and aerospace engi-

neering are the two main application areas where similitude is used for scale model testing for fluid flow problems. Any new design concept needs to be scrutinized using rigorous theoretical and experimental verification before it enters the production phase. Tests are generally performed on a model that has formal similarity to the prototype. The behavior of the prototype can be predicted based on the behavior of the model using an appropriate set of relationships [72].

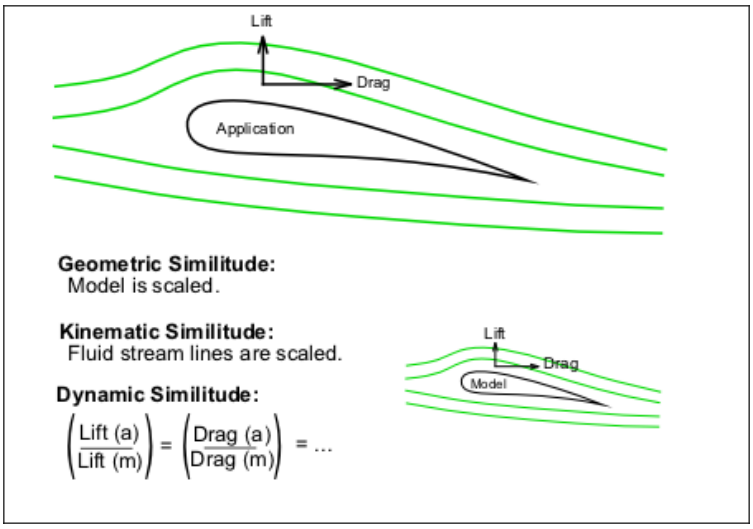

Figure 2.1

Criteria for model to have similitude with a prototype (Public domain image from Wikipedia).

Similarity of systems is defined by a unique set of characteristic equations that ensures that these equations are valid for all similar systems [73, 74]. Creating similarity amongst systems assists in forecasting performance of a system based on the results obtained from other similar systems that can be studied more easily than the original system.

Safoniuk et al. [75] used the Buckingham Pi theorem to scale up a three-phase fluidized bed. Their study made use of dynamic and geometric similitude to derive the scaling laws. Chouchaoui et al. [76] developed scaling laws for the elastic behavior of a laminated cylindrical tube subjected to various loading conditions. Yazdi and Rezaeepazhand [77] utilized similitude to design scale models to calculate the flutter pressure of delaminated composite beam-plates under the influence of supersonic airflow. Ramu et al. [78] established a structural similitude for elastic models built using different materials. The scaling laws derived in their research have been validated using analytical methods on simple test problems. Their work also made use of finite element analysis to validate the similitude relationships between the model and the prototype. Simitses et al. [79–82] carried out several research efforts focused on symmetrically laminated plates to identify the similarity conditions between the model and the prototype. Their research makes use of scaling laws to design scaled models and uses theoretical methods to compute the model data to predict the behavior of the prototype. Their method is restrictive because an exact or analytical form of the solution has to be derived prior to using this methodology for a given set of problems. Ungbhakorn and Singhatanadgid [83] derived the similitude invariant for anti-symmetrically laminated plates by applying the similitude transformation directly to the governing differential equations of buckling. Their work derived the scaling laws for buckling loads on laminated plates with biaxial loading conditions.

2.5 Failure analyses in structural systems

This section provides an overview of the methods currently used for analyzing failure in structural system. Analysis of the response of the structural system to external forces is pivotal in determining if the structural design will be able to withstand the internal stresses generated by the loads other than the design loads. Several techniques are available to measure the response of the structural system to external forces. Existing methods such as acoustic emission [84–90] and digital image correlation [91–100] provide a means to measure/quantify/determine the strains/deformations experimentally. From the modelling perspective, there are continuum-based [101–103] and discrete or lattice-based [104–106] approaches. These approaches satisfy the physical laws governing the system and provide the information required for analysis of the structural system. However, obtaining information regarding the influence of local topology on the global performance of the system requires additional information. Although Tordesillas et al. [107] and Lefort et al. [108] have successfully used mathematical approaches to identify patterns that are formed by the local topological interactions that govern the global response of the system; their work is conducted at the mesoscale. To the author's knowledge, advanced mathematical algorithms have not been used with continuum-based models to gain fundamental insight into the failure mechanisms of bio-structures. Since bio-structures are geometrically optimized at the coarsest level of hierarchy, the information obtained at the local topology level will provide new insights that could be utilized to identify optimal geometrical configurations that make bio-structures resilient and lightweight.

2.5.1 Shear bands in dense granular media

The formation of shear bands is a unique characteristic of degradation and failure in many materials. Although considerable research has been focused on understanding them, the origin and formation of shear bands still remains a mystery [107, 109, 110]. At the onset of loading, the ultimate shear band pattern was observed to be encoded in the grain kinematics [109]. Tordesillas et al. [109] seek to investigate the development of bottlenecks in transmission of force through the contact network by applying network flow theory [111, 112]. In this case the flow network is formed from the contact network of the material [111, 113, 114]. Tordesillas's [111] work maps the contact network at each equilibrium state in the deformation history to a flow network and solves the maximum-flow/minimum-cut problem. The bottlenecks in the force transmission that are recognized by the minimum-cut disclose that the localization of deformation into shear bands is a progressive phenomenon of degradation that starts almost at the onset of loading. Although the grains whose contacts form the bottlenecks are continuously changing from one equilibrium state to another, these bottlenecks eventually become spatially localized at the onset of loading history in the region where the persistent shear band finally forms. These findings are in agreement with the results from multiscale analysis of vortices from simulations and experiments in 2D [107, 115]. The formation and location of the bottlenecks is influenced by both local and global properties of the material. Tordesillas et al. conclude that the early identification of bottlenecks in force transmission open up new avenues for detection as well as manipulation of the approaching failure in granular systems.

2.5.2 Failure analysis in quasi-brittle materials

Macro cracks in quasi brittle material are formed by the combined effects of micro-crack propagation, interaction and coalescence, which are situated within the Fracture Process Zone (FPZ). Lefort et al. [108] employs statistical analysis to gain detailed insight into the evolution of the FPZ. Ripley's function [116] is utilized to identify patterns in image analyses. Ripley's K function is employed to characterize the randomness in the spatial spreading of point distributions. It has been widely used in spatial ecology and has also been used to identify the development and spreading of diverse patterns, e.g., cell migration [116], tree [117] and plant [118] dissemination, or disease spreading [119]. Ripley's function as applied to damage mechanics is described in detail in Lefort et al. [26]. The cracking process at the mesoscale of a concrete specimen is analyzed in detail. Lefort at al. conducted both numerical and experimental analyses on concrete. The numerical model used in their study is a lattice-based approach that produced good agreement with experiments integrated with acoustic emission analyses. This signifies that the numerical model could be used in conjunction with Ripley's post processing technique to examine the evolution of the correlation length upon failure. Numerical experiments were performed with direct tension as well as three-point bending tests. Their results show that the extracted correlation length is not constant during failure and is dependent on the type of loading applied to the same specimen. This research may open up new paths that would result in non-local continuum modeling at the macroscale level.

2.5.3 Comments on the mesoscale approach

The approaches used by Tordesillas et al. [111] and Lefort et al. [108] have been used at the mesoscale level to analyze failure mechanisms in two completely different structural systems. Experimental and numerical tests on structural systems produce abundant data that could be analyzed efficiently by employing advanced mathematical algorithms. Although these approaches were used for discrete models, they also laid the foundation for applying multidisciplinary approaches to identify failure patterns in structural systems. Both applications demonstrate that the local topological interactions are a major contributor to the global structural response. Obtaining this information at the onset of loading will open up avenues to obtain insight into the failure mechanisms and possibly suggest novel approaches to alter and modify the phenomena and location failure site. Also, if the location of failure is identified earlier than its occurrence, there is a possibility of developing a relationship that will define the amount of external forces required for the structural system to fail at that location. This information can be used not only to design new structural systems but also for assessment of existing critical infrastructure.

2.6 Previous research on the rostrum

Research conducted on the rostrum of the North American paddlefish revealed that it is distinct and complex with no functional counterpart in any other species. It is long, broad, and flat, rounded at the tip, and rhomboidal in cross-section. The cartilage endoskeleton consists of a central gelatin-filled tube, flanked by two buttresses, and supports a lattice-like network of small inter-connecting stellate bones [22–24]. The bone diameter is larger

near the center of the rostrum and smaller near the edge, but the pattern is not obvious. The relative size and shape of the rostrum are highly variable in juveniles [25], less so in sub-adults and adults [29]. Rostra in other species of fish consist of flat blades of solid cartilage (sawfishes and some sharks) or simple tubes of bone (swordfish, marlin, etc.) and do not vary appreciably in size or shape within species. Swimming enhancement induced by the rostrum has been extensively studied [1, 21, 120]. The modeling and analysis of the stress state and strain rate dependence behavior of cartilage have been conducted by Deang. et al. [121]. Allison et al. [122] characterized the rostrum's stellate bones. Recent computational analysis efforts revealed the rostrum has far greater attributes of energy dissipation and impact resistance when compared to man-made engineered systems [6]. The rostrum's lattice structure is the major contributor for the superior performance. However, the lattice is an indeterminate, non-linear structure with varying material types, and material properties, with non-uniform stiffness and irregularly-shaped members. Knowledge is lacking on how the geometrical assembly of the structure impacts its high-performance strength/toughness characteristics.

2.7 Summary

Bio-structures have, in general, demonstrated superior characteristics as they evolved to serve multiple and specific functions. Since bio-structures are made of heterogeneous materials and possess hierarchical geometry, it is difficult to identify the major contributor to their structural response. Also, owing to the complex geometry of the bio-structures, the computational mechanics experiments employed to analyze them will produce large data

sets. This research seeks to answer the following questions: Is the superior performance of bio-structures because of the heterogeneous material properties, is it the hierarchical geometry, or is it a combination of both? Is there a preferred configuration that shows optimum performance? Can it be identified through the application of the flow network approach?

The end product of this research is visualized to be a problem-driven, solution-centered approach that integrates mathematics, mechanics and computational sciences for a rapid design, test, and build cycle. Based on current work related to the proposed effort, the following observations can be made on the feasibility of the transdisciplinary computational mechanics/mathematics approach:

1. Although the scientific community has done significant research to analyze structures created by nature, there is still a considerable lack of understanding as to why bio-structures possess high-performance strength/toughness characteristics.
2. Flow networks have been used to study a variety of complex problems and patterns. They have also been used in conjunction with a discrete element model to unravel the location of the persistent shear band in dense granular media. However, this approach has not been used to study the complex geometrical hierarchical configuration of bio-structures.
3. Since the existing methods do not provide sufficient means to obtain a fundamental understanding of the redundant lattice architecture, a new transdisciplinary approach is required.
4. Dimensional analysis and similitude are a set of powerful mathematical tools that have been utilized in a broad range of applications. Scaling structural hierarchy from observations derived from finite element analysis and flow networks will provide a unique outlook towards an integrated use of these potent tools.
5. Similitude has generally been applied to scale models to reduce cost and complexity. In this research, similitude laws were utilized to scale up a model by conducting numerical and mathematical analysis on a smaller scale, bio-inspired model.

CHAPTER III

RESEARCH APPROACH

Computational mechanics experiments carried out on the rostrum revealed that the rostrum has exceptional energy dissipation and load bearing capacity as compared to man-made systems [6]. The motivation provided by these findings laid the foundation of this research work. This research proposes to gain fundamental insights into the design and engineering of high-performance, lightweight, structured composites by investigating the load-bearing characteristics of the hierarchical lattice architecture of the paddlefish rostrum. A fundamental understanding of how this lattice-like architecture functions has the potential to impact applications over a wide range of disciplines (e.g., protective panels, novel building materials, body and vehicle armor, and ship design among other possible uses). This chapter describes the research approach and illustrates the implementation of the approach on a demonstration model constructed from a small part of the rostrum.

3.1 Transdisciplinary research approach

Figure 3.1 provides a flowchart of the research work plan. Since bio-structures are composed of hierarchical lattice geometry and varying material properties, it is difficult to design experiments to determine the major contributor to their structural resiliency. Hence, it becomes necessary to understand the influence of local topology on the global structural

response. Based on these findings, a transdisciplinary research approach is required to investigate failure mechanisms of the rostrum.

As shown in Figure 3.1, the first step will involve the construction of a 3D model using multiple CT scans of the rostrum. A numerical representation was developed from the 3D model that was used for computational mechanics experiments on the rostrum subjected to external loading. For this research, the finite element experiments were performed using the commercial package Abaqus. Although the finite element simulations give an overall distribution of stresses in the system, the underlying detail provided by the changing kinematics of the systems that play a vital role in the load transfer mechanisms and formation of the strong and weak links in the network are missing. Towards this end, the loading of the rostrum was formulated as a network flow problem. The nodes and edges of the rostrum's network were extracted from the model used in the finite element analyses. The flow network was weighted based on the parameter of interest, which was Von-Mises stress. The kinematics of the structural system changes when it is under the influence of an external loading condition. The results from the finite element analysis were input to the network flow algorithm that computes the maximum flow of the stresses.

3.2 Computational mechanics experiment on rostrum

To obtain an understanding the material response of the rostrum, high performance computational mechanics simulations are performed using Abaqus 6.13 [123]. A general static analysis is conducted on the rostrum using Abaqus/standard. The complexity and volume of data involved in such an analysis requires the use of a high performance com-

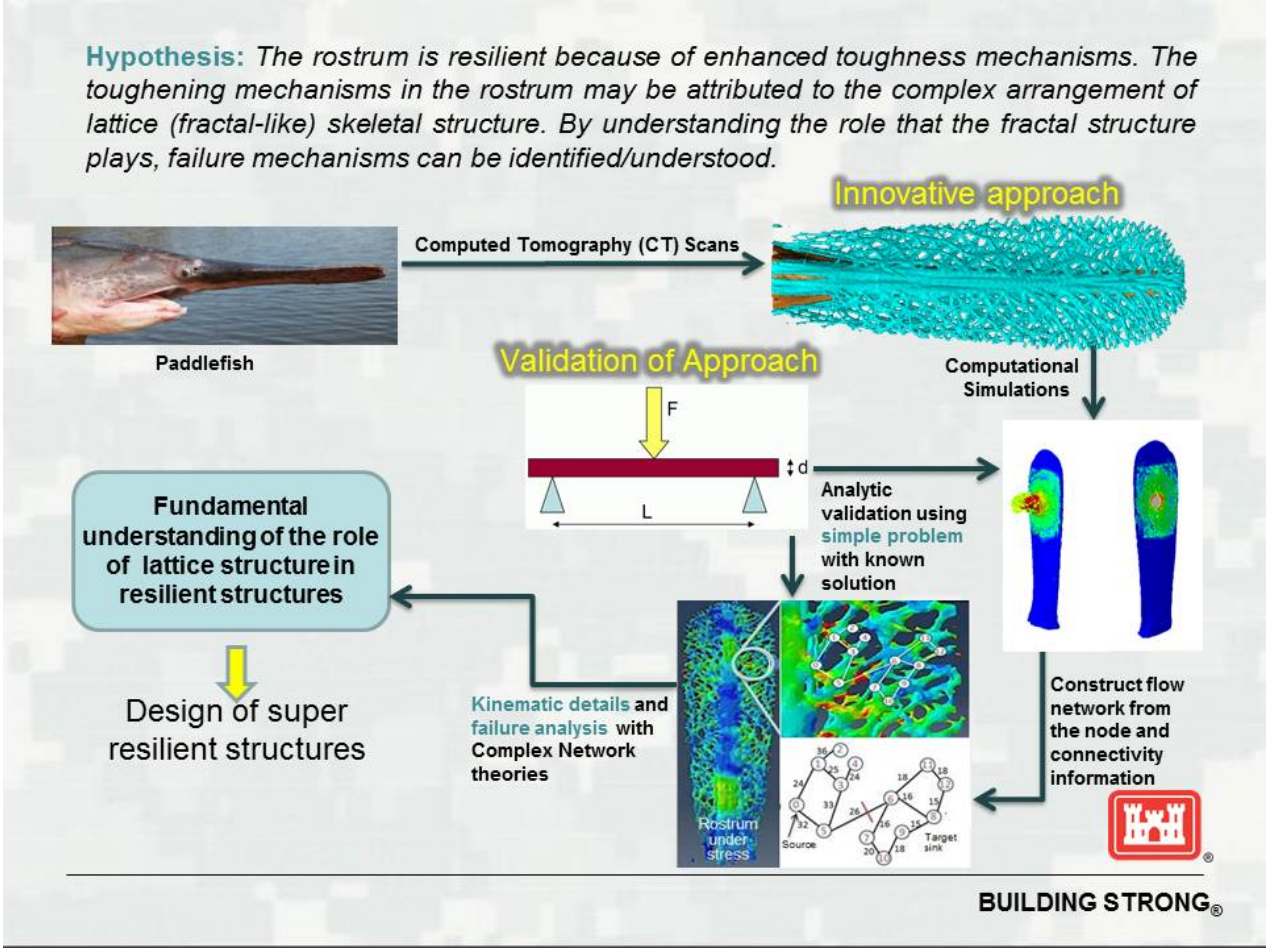

Figure 3.1

Transdisciplinary research flowchart

puting environment. Owing to the complexity of the geometry and the analysis, each job was executed on ERDC's High Performance Computing facilities located in Vicksburg, MS. Figure 3.2 shows the image of the Cray XE6 -1.5 PFLOPS (Garnet) located at the ERDC's High Performance Computing Modernization Program (HPCMP) Department of Defense (DoD) Supercomputing Resource Center (DSRC).

Figure 3.2

Garnet. Cray XE6 - 1.5 PFLOPS (Courtesy of ERDC-HPC-DSRC)

3.3 Flow network

The road network is the most practical implementation of flow networks. Road networks can be represented as a directed graph in order to identify the shortest path from point A to point B. In a similar manner, the flow of stresses in a structural system can be interpreted as a directed graph, which facilitates the investigation of questions about failure mechanisms. Intuitively, the flow of information at a given point in the system is the rate at which the information (i.e., variables such as stresses, displacements, kinetic en-

ergy, elastic or plastic strain in a structural system) travels. Each edge in a directed graph can be compared to a channel through which information passes and has a corresponding capacity that is representative of the maximum rate at which information can be passed through the edge (e.g., 100 gallons of liquid per second through a pipe or 11 amperes of electrical current through a wire). Vertices of the graph are the points where the edges connect. All vertices in the graph, except the source and sink, have information flowing through them (i.e., the rate at which information enters the vertex is identical to the rate at which information leaves the vertex). In other words, the flow is conserved in a manner similar to Kirchhoff's current law.

Complex networks separate the physics of the problem from the data and map the problem an abstract domain where calculations are performed. Then, the solution is mapped back to the physical domain. The research described here develops new methodologies that will provide the foundation for using flow network algorithms with efficient vector-based programming to tackle highly complex and evolving data obtained from finite element analysis and experiments.

To gain a fundamental understanding of the superior performance of the rostrum, the current research employs complex network analysis. A novel mathematical technique is employed to formulate the rostrum as a network flow problem [124, 125]. To achieve this, a flow network graph *G= (V, E)* is developed from the finite element model of the rostrum such that:

1. *V* represents the nodes obtained from the finite element model of the rostrum. As shown in Figure 3.3(a), for a hexahedral element in a finite element model, the nodes are 1, 2, ..., 8.

2. E represents the edges connecting the nodes in V and is obtained from the connectivity A between the nodes. The edges of the hexahedral element shown in Figure 3.3(a) are $\{(1, 2), (2, 3), (3, 4), (4, 1)\}$ for face 1.

3. Each edge, *(u,v)*$\in$ *E*, has a capacity *C* associated with it which is representative of the maximum amount of flow that could be transmitted through the edge. The capacity calculation for edge (1, 2) is shown in Figure 3.3(c). The capacity for edge (1, 2) is the average of the Von-Mises stresses at nodes 1 and 2.

4. The Von-Mises stresses (shown in Figure 3.4) at each node are calculated using the average of the integration points shown in Figure 3.3(d).

Two nodes are identified in the network to serve as the source *s* and sink *t* nodes such that the flow can be transmitted from the source node *s* to the sink node *t*. The selection of these nodes will be dependent on the boundary conditions that are applied to the rostrum. For example, if the rostrum is subjected to compression loading from the top and bottom, the source and sink nodes can be selected from the top and bottom loading surfaces, respectively. From Newton's third law of motion it can be inferred that the transmission of flow along each edge is symmetric. Hence, the flow from source to sink is identical if the source and sink nodes are swapped.

3.3.1 Flow networks and flows

A flow network is a directed graph *G(V,E)* consisting of a finite set of vertices together with a subset of ordered pairs of nodes that represent the edges. Each edge $(u, v) \in E$ has a non-negative capacity $c(u, v) \geq 0$. It is assumed that $c(u, v) = 0$ if $(u, v) \notin E$. Therefore, two nodes are identified in a flow network; a source *s* and a sink *t* [113, 126, 127]. It is also assumed that every node belongs to a certain path that connects the source and sink (i.e., for each node $v \in V$, there is a path $s \rightarrow v \rightarrow t$). In other words, the graph is connected.

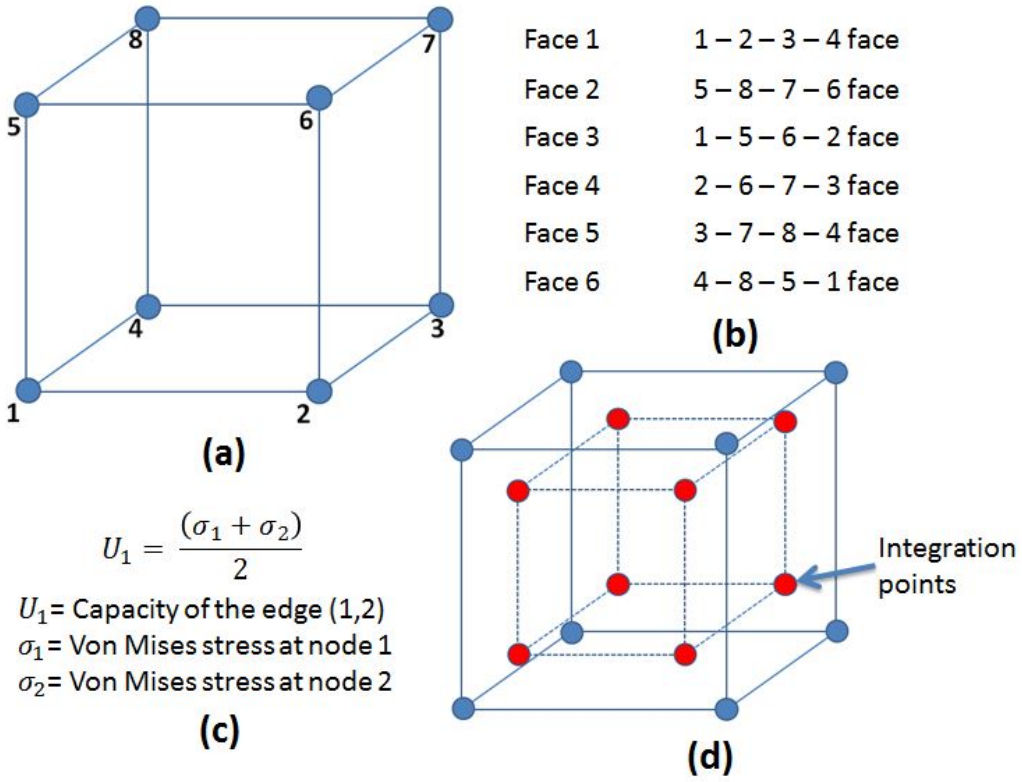

Figure 3.3

(a) Node numbering in an 8 node hexahedral element (b) Hexahedral element faces in a 8 node hexahedral element (c) Capacity calculation for edges in flow network graph (d) Integration points on a 8 node hexahedral.

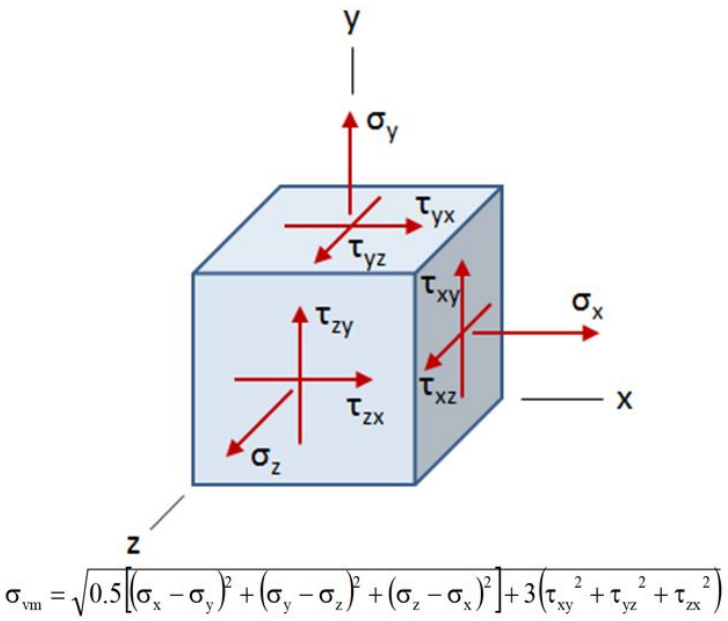

Figure 3.4

Von-Mises stress equation expressed by the six stress components.

A flow in G defined by the real-valued function $f : V \times V \rightarrow R$, is a feasible flow vector if it satisfies the following constraints:

1. Capacity Constraint: $\forall u, v \in V$, requires that $f(u, v) \leq c(u, v)$, the flow cannot exceed the capacity of the respective edge
2. Conservation of flow: $\forall u, v \in V - (s, t)$, requires that
   (a) $\Sigma_{v \in V} f(u, v) = 0$
   (b) The total flow entering a node must equal the total flow leaving that node provided the node is not a source or sink node
3. The total flow leaving the source node s must be equal to the total flow entering the sink node t

3.3.2 Maximum flow in a flow network

Given a flow network *G(V,E)*, with source *s* and sink *t* such that there are no incoming edges at the source and no outgoing edges at the sink, the maximum flow problem can be defined as follows:

A maximum flow *f*, from source *s* to sink *t*, is a function that satisfies the capacity and conservation constraints described above and its value is defined as follows:

$val(f) = max(f)$.

The maximum flow problem, as described above, can be solved by applying the Ford-Fulkerson algorithm [113].

3.3.3 Ford-Fulkerson Algorithm

For a connected graph *G(V,E)*, the flow *f* in *G*, which is the total flow that leaves the source node *s* and the total flow that enters the sink node *t*, is defined as follows:

$$\mid f \mid = \sum_{v \in V} f(s,v) = \sum_{v \in V} f(v,t).$$

The residual capacity of the node pair(u,v), or $c_f(u,v)$ is defined as:

$c_f(u,v) = c(u,v) - f(u,v)$.

The value of residual capacity is used to determine how much flow can be transmitted between a given set of nodes.

The residual network of *G* induced by *f* is the graph $G_f = (V, E_f)$ such that

$E_f = (u,v) \in V \times V : c_f(u,v) > 0$

For each edge $(u,v) \in E$ do

$f[u,v] \leftarrow 0$

$f[v,u] \leftarrow 0$

While $\exists$ (there exists) a path *p* from source *s* to sink *t* in the residual network G_f do

$\Delta \leftarrow min[c_f(u,v) : (u,v) \in p]$

For each edge (u,v) in *p* do

$f[u,v] \leftarrow f[u,v] + \Delta$

$f[v,u] \leftarrow -f[u,v]$

3.3.4 Maximum-flow/minimum-cut theorem

A cut of a flow network *G(V,E)* is defined as a set of vertices (E_1, E_2) that partition V into E_1 and $E_2 = V - E_1$ such that $s \in E_1$ and $t \in E_2$. If f is a flow, then the net flow across the cut (E_1, E_2) is defined as $f(E_1, E_2)$. The capacity of the cut (E_1, E_2) is $c(E_1, E_2)$.

A minimum $E_1 - E_2$ cut problem involves minimizing $c(E_1, E_2)$. That would mean the identification of E_1 and E_2 in such a manner so as to find the minimal capacity of the $E_1 - E_2$ cut.

In combinatorial optimization theory [124], the maximum-flow/minimum-cut theorem states that in a flow network *G(V,E)*, the maximum quantity of flow f travelling from the source node s to the sink node t is identical to the total weight of the edges in the minimum-cut. Essentially speaking; the smallest total weight of the edges which, if removed, would cause the source to be totally disconnected from the sink.

3.4 Analytical verification of research methodology

This section provides the verification of the flow network approach to identify failure mechanism. Two classical problems with known solution are chosen for verification. The customary technique for verifying a simulation is to employ a problem that is simple enough to have an analytical solution and similar enough to the phenomena that is being simulated so that a meaningful extrapolation to the actual problem is feasible. By doing so, the numerical and analytical solutions can be compared and fundamental shortcomings with either the methodology or the numerical approach used to solve the problem can be identified. To verify the current research methodology, two classical problems are chosen. The problem descriptions and methodology implementations follow in the subsections below.

3.4.1 Problem 1: Three-point bending of a simply-supported beam

To verify the flow network approach used in the current research, a simply-supported beam with a concentrated load at its midpoint, as shown in Figure 3.5, was chosen. A schematic of the beam with this loading condition and the shear and moment diagrams are shown in Figure 3.6 [3].

Abaqus was used to perform the finite element simulation for a concrete beam of length 216 in, width 36 in, and thickness 6 in. A mass density of $8.67e^{-011} slug/in^3$, Young's modulus of $3*10^6 psi$, and Poisson's ratio of 0.3 were used for the concrete material model. The Abaqus mesh used for validation model consisted of 73,278 quadratic tetrahedral elements comprising of 117,709 nodes. The Von-Mises stresses obtained from the finite

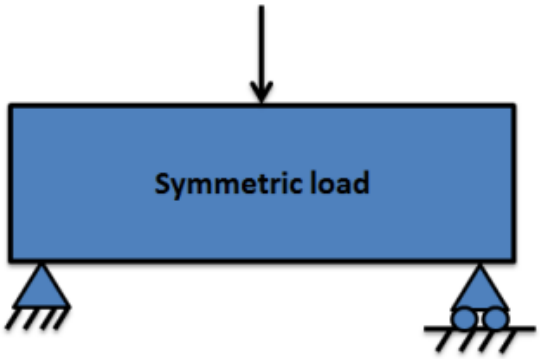

Figure 3.5

Three-point bending of a simply-supported concrete beam with symmetric loading at center

element simulations are plotted in Figure 3.7, which shows the overall stress distribution in the beam subjected to a pressure of 100 MPa at the center. The simulation was carried out using the dynamic, explicit method in Abaqus for a total time of 0.005 s. Geometric non-linearity effects were included.

The node and connectivity information were extracted from the finite element model using the procedure outlined in Figure 3.22 to construct a flow network. The network was weighted based on the Von-Mises stress values from the Abaqus results. The source and sink combinations were selected from the high stress areas on the top and bottom surfaces of the beam, respectively. The result of the network flow analysis is shown in Figure 3.8. The minimum-cut identified by the mathematical algorithm is represented by blue line in Figure 3.8. The minimum-cut denotes a set of edges in the flow network that inhibit the transmission of flow or form the bottlenecks of transmission, i.e., the flow network analysis highlights the regions of the beam where the failure mechanism initiates. For this problem,

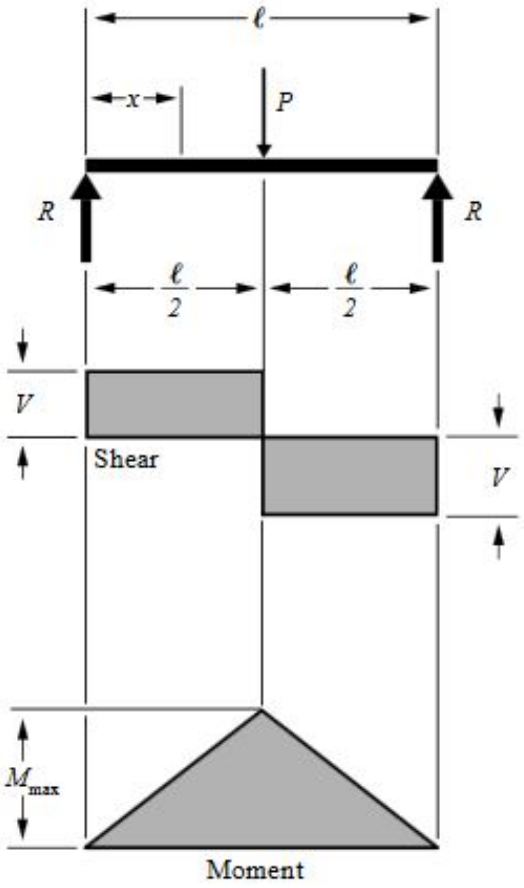

Figure 3.6

Shear and bending moment for a simply-supported beam with a concentrated load at the center [3]

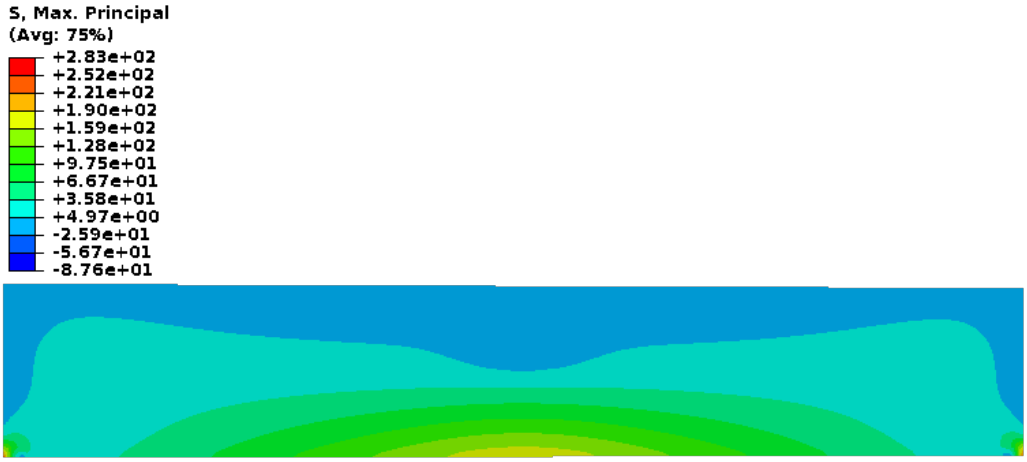

Figure 3.7

Maximum principal stresses for three-point bending of a simply-supported concrete beam

the network analysis shows the expected behavior of a beam subjected to a concentrated load at the center line. Failure for this classical problem initiates with a crack at the bottom face at the midspan of the beam that continues to grow as the load increases. Hence, the proposed methodology for detecting the failure mechanisms in the nascent stages of loading from the computational mechanics experiment and flow network approach was verified using a simple problem with a known solution. The flow network approach does not require running non-linear finite element analysis that uses damage models to failure. Early identification of failure using this approach results in reduction of computational cost, time, and complexity.

3.4.2 Problem 2: Four-point bending of a simply-supported beam

The dimensions and material of the model used for Problem 2 are identical to the concrete beam used in Problem 1. For this problem, the concrete beam was simply-

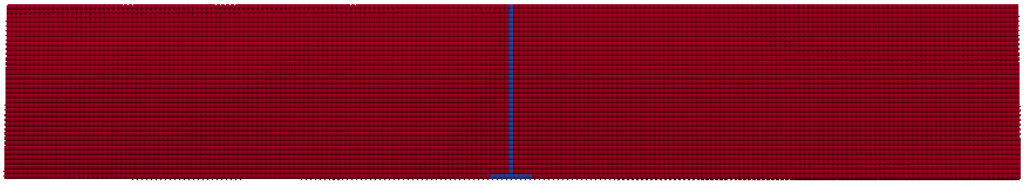

Figure 3.8

Flow network result for three-point bending of a simply-supported concrete beam

supported with two equal forces applied equidistant from the supports as shown in Figure 3.9 [128, 129]. A schematic of the beam with this loading condition and the shear and moment diagrams are shown in Figure 3.10 [3].

The maximum-flow/minimum-cut algorithm was employed to investigate seven scenarios. The source node in each scenario was chosen to be a vertex where the force is applied while the sink node was chosen to be a point in an area where a stress variation was visually identified based on the the maximum principal stresses shown in Figure 3.10. Seven sink nodes were selected. The network flow algorithm was executed seven times using these source-sink combinations. The results were superimposed since the material was in the linearly elastic regime.

Figure 3.12 shows the superimposed result produced by running the maximum-flow/minimum-cut algorithm. The minimum-cut has clearly identified the shear patterns on the left and right corners and flexure patterns in the center highlighted by the white lines in Figure 3.12. These shear and flexure patterns govern the phenomena of failure mechanism in this problem. The network flow strategy identified these patterns at the onset of loading when the

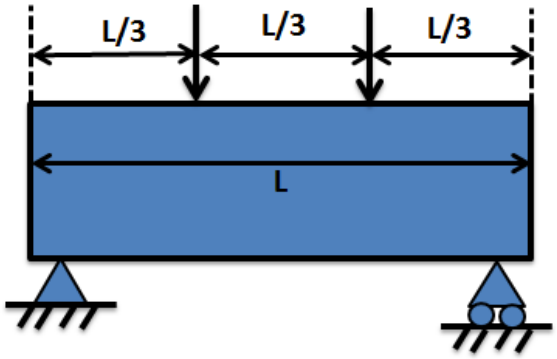

Figure 3.9

Four-point bending of a simply-supported-concrete beam

material was still in the linearly elastic regime and did not require running the finite element simulation to failure.

3.4.3 Summary

Verification and validation play an important role in scientific computing. They provide the foundation of building confidence in modeling and simulation. The results shown in this chapter have verified the proposed research approach using two classical problems for which the solutions were known. The following observations can be made about the research approach that uses flow network and finite element analysis for early detection of failure mechanism:

1. For the problem of three-point bending of a simply-supported concrete beam, the flow network approach captured the expected behavior of a beam subjected to a load at the center. The flow network approach successfully identified the regions of the beam where the failure mechanism initiates.
2. For the problem of of four-point bending of a simply-supported concrete beam, the flow network strategy clearly identified the shear patterns on the left and right corners and the flexure patterns in the center. The failure mechanism is governed by these shear and flexure patterns.

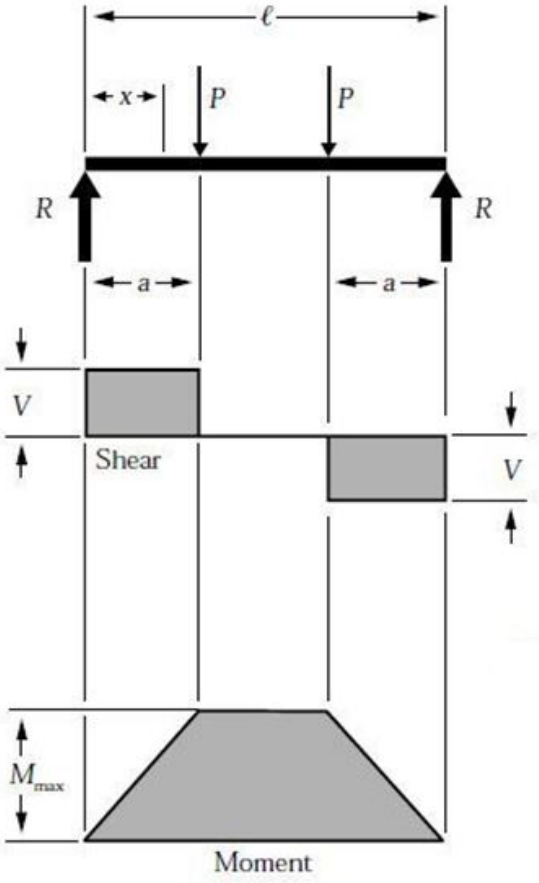

Figure 3.10

Shear and bending moment for four-point bending of a simply-supported concrete beam [3]

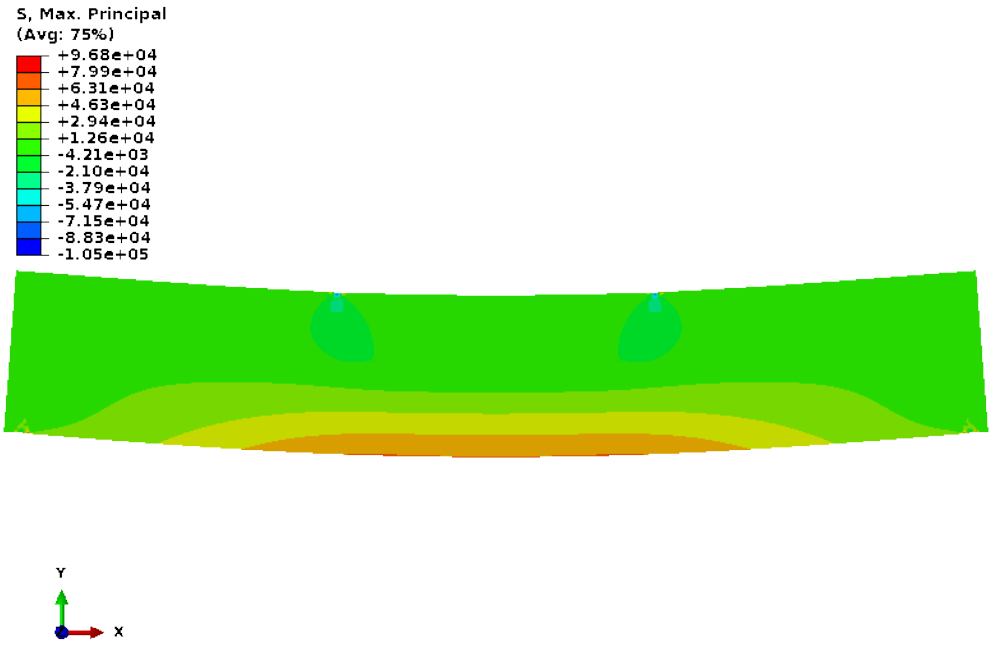

Figure 3.11

Maximum principal stresses for four-point bending of a simply-supported concrete beam

Figure 3.12

Flow network result for four-point bending of a simply-supported concrete beam

3. In both cases, the integrated flow network and finite element approach identified these patterns at the onset of loading when the material was still in the linearly elastic regime and did not require running a non-linear finite element analysis that employed damage models until the material failed. This results in reduction in computational cost, time, and complexity.

3.5 Rostrum model

An X-ray CT was performed on the paddlefish rostrum using the Phoenix v|tome|x. Figure 3.13 shows the rostrum of the paddlefish and the X-ray CT scan that was developed by combining multiple CT scans [121] from which the computational model was obtained. Figure 3.14 shows the tissue component of the rostrum, which is the outermost layer of the rostrum that encompasses the hard cartilage shown in Figure 3.15 and the innermost soft cartilage displayed in Figure 3.16. The soft cartilage is located in the central portion of the rostrum. The hard cartilage branches out from the center of the rostrum toward the edges of the rostrum as shown in Figure 3.15 and Figure 3.17. The computational models of the three parts were individually imported into the commercial software Abaqus. These complex parts were meshed using a combination of hexahedral and tetrahedral elements. The details of the mesh are provided in Table A.4.

3.6 Stress contours of the rostrum subjected to a blast load

Figure 3.18 displays the non-dimensionalized Von-Mises stress for the rostrum prototype. Further details of this analysis are provided in Appendix A. Finite element simulations were conducted for the rostrum subjected to a blast load. Von-Mises stresses on the three-components of the rostrum namely, the outermost soft tissure, the inner hard cartilage, and the innermost soft cartilage, are displayed in Figure 3.18. For illustrative

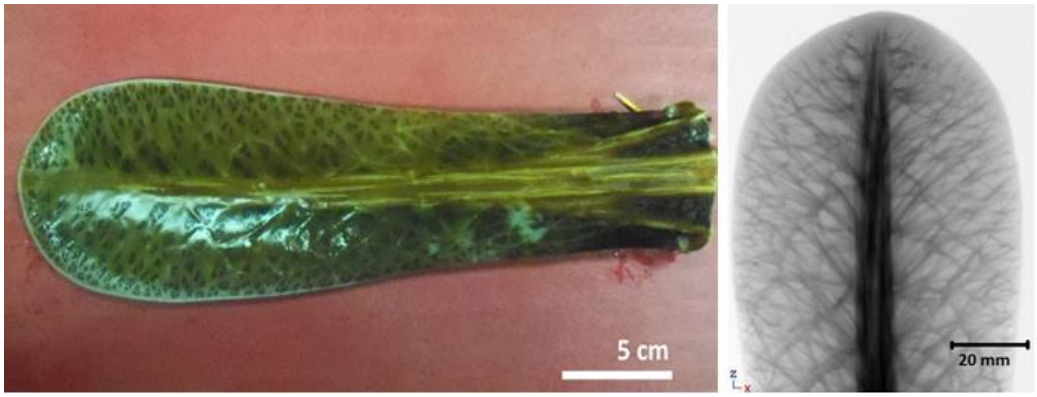

Figure 3.13

X-Ray CT scans performed on rostrum

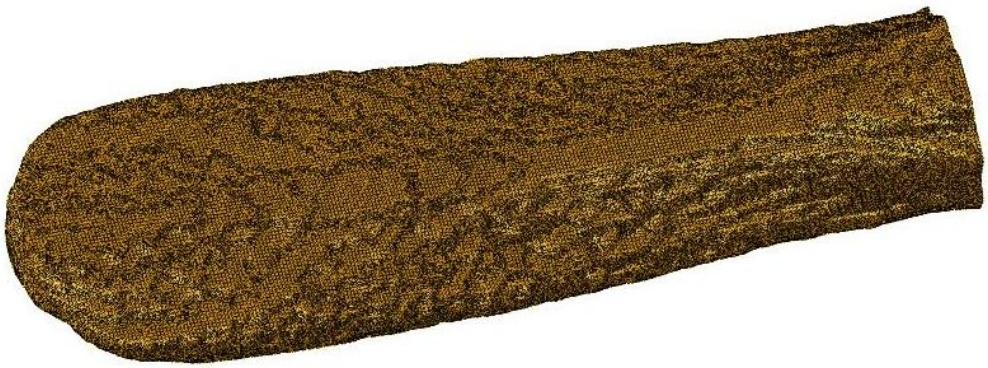

Figure 3.14

Tissue mesh

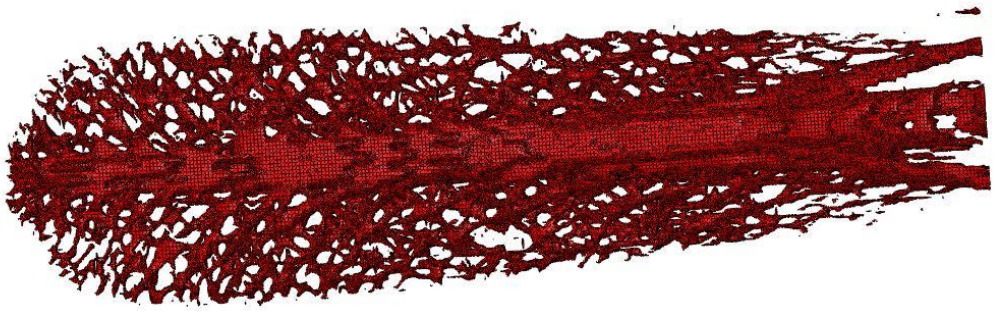

Figure 3.15

Hard cartilage mesh

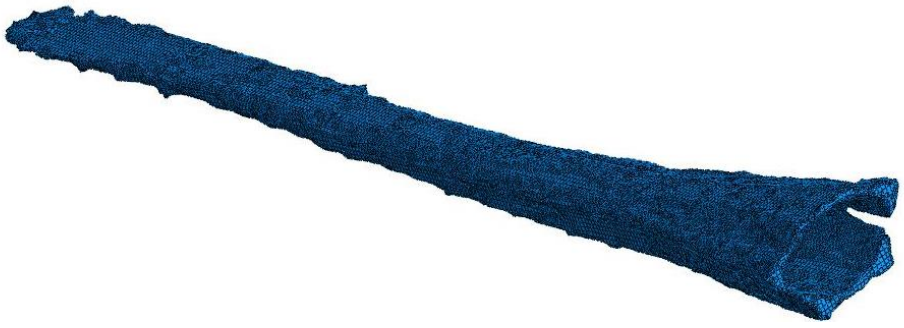

Figure 3.16

Soft cartilage mesh

Figure 3.17

Cross section of mesh assembly of the three components of rostrum (i.e., tissue, hard cartilage, and soft cartilage).

purposes, Section 3.7 describes the procedure by which a small part of the hard cartilage is represented as a flow network.

3.7 Demonstration model to represent the rostrum as a network flow problem

The output from the finite element model was provided as input to the complex network algorithm to gain insight into the underlying kinematics. For fractal and discrete systems, force chain networks are known to be the key for load transmission [55–57]. When the networks are short circuited, deformation ensues. While complex networks have been used to examine interactions within various complex systems as outlined in Chapter 2, this technique has not been used to study the failure mechanism in the complex geometrical hierarchical configurations characteristic of bio-structures.

The demonstration of the flow network approach through a toy network constructed from a small region of the rostrum is shown in Figure 3.19. Recall that, for a given flow

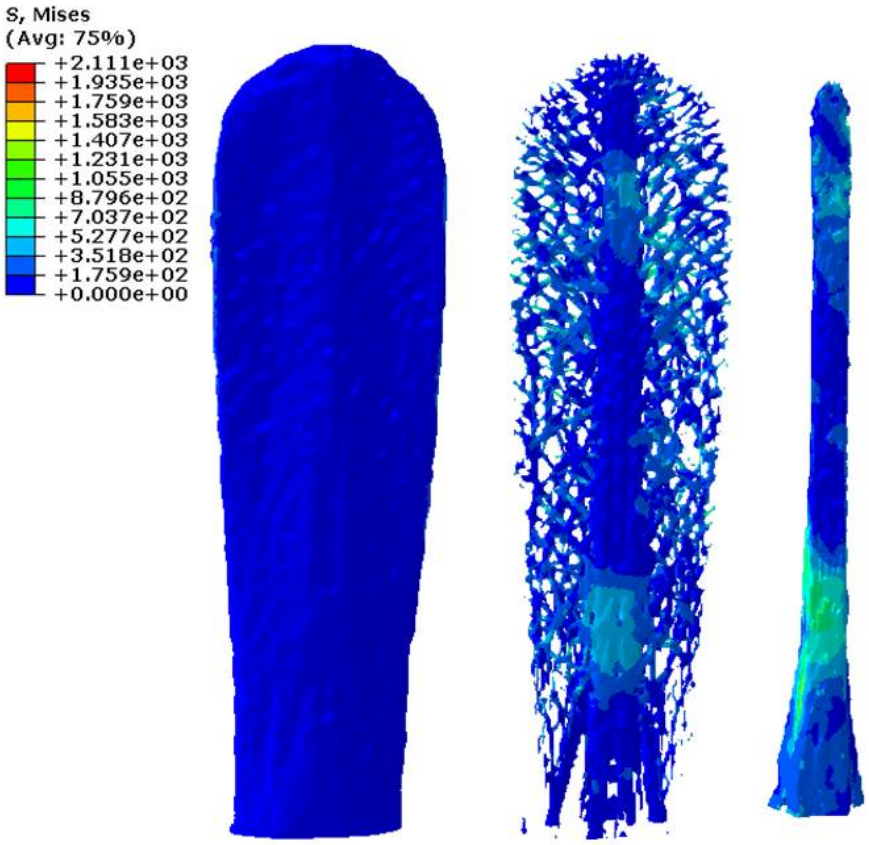

Figure 3.18

Non dimensional Von-Mises Stresses on top surface of the three component parts of the rostrum prototype subjected to blast load (Details of model and experiment is provided in Appendix A)

network, the maximum flow is equal to the capacity of the minimum-cut [130]. Using the Ford-Fulkerson algorithm described previously in Section 3.3.3, the capacity of the minimum-cut is determined. For example, for the flow network shown in Figure 3.19, the possible cuts are:

1. (1-2), 1-6)
2. (10-9), (7-9), 13-9)
3. (6-7)

The minimum source-sink cut is (6-7) which has a capacity of 26 (highlighted in red in Figure 3.19). Based on the flow patterns established at the onset of the load application, the complex network approach can aid in detecting the failure site much earlier (i.e., before the material fails or when the material is in the linearly elastic regime of the stress strain curve) than any computational or analytical methodologies.

The nodes V and the edges E of the flow network are obtained from the finite element model created in Abaqus using a python script. The capacity C of the edges is obtained from the output database file created from the finite element experiment. A DIMACS [131] format file is created using a C++ program developed specifically for this research. For the demonstration flow network shown in Figure 3.19, the DIMACS file is shown in Figure 3.20. The lines in Figure 3.20 that begin with "c" are comments. The problem line that begins with a "p", defines the type of problem that is being solved. In this case, it is the maximum flow problem, followed by the total number of nodes and links, which in this case are 13 and 15, respectively "p max 13 15". The comment line "c source" is followed by the line that begins with an "n" followed by the node number that represents

the source node “n 1 s”. The comment line “c sink” designates the sink node, Node 9, which is represented by “n 9 t”. The lines beginning with “a” describe the arcs or edges of the flow network. There are 15 arcs in the demonstration model.

This DIMACS file represents one static state extracted from the output database file. As the kinematics of the system changes, several DIMACS files will be generated to represent the changing state of the system under the influence of the external load. The DIMACS file created using the above procedure was input to the maximum-flow/minimum-cut algorithm described by Boykov and Kolmogorov [132]. Figure 3.21 shows the output obtained from using the maximum-flow/minimum-cut algorithm. As shown in Figure 3.21, the maximum flow is 26. Also, the nodes get flagged as either 0 or 1, i.e, they either belong to the source or the sink, respectively. The coordinate information of the nodes is extracted from the finite element input file. Paraview [133] is used to plot the output of the maximum-flow/minimum-cut algorithm.

Figure 3.22 shows the flowchart of the formulation of a small part of the rostrum as a network flow problem. The bio-structure (rostrum of paddlefish) is formulated as a network flow problem using the software developed for this study following the four steps outlined below. The key issue addressed in the current software is the requirement to link information between different tools used in the analysis. The flow network graph is generated from the binary output database files generated by the finite element analysis. This procedure is executed in four stages as shown in the flowchart in Figure 3.22. In stage 1, the flow network is constructed using the nodes and connectivity information from the finite element analysis. In stage 2, the flow network is weighted based on the parameter

of interest (stresses in the current study, also obtained from the finite element analysis). In stage 3, a DIMACS format file is created that represents the flow network graph. In stage 4, the DIMACS file is provided as input to the mathematical algorithm that calculates the minimum-cut of the flow network graph. The details of the procedure involved in the four stages are described subsequent subsections below.

3.7.1 Stage 1 – Obtain connectivity information

The finite element model of the bio-structure was created in Abaqus and a python script was employed to extract the connectivity information. This script was written in python since Abaqus supports data extraction and manipulations through this programming language both within its graphical user interface and through the command line. This script outputs the connectivity data to a text file. Table 3.1 displays the file produced by executing the python script on the computational model of rostrum. The connectivity information file shown in Table 3.1 comprises three columns. Column 1 displays the node ID. Column 2 is the total number of nodes to which the node displayed in column 1 is connected. Column 3 displays the IDs of the nodes to which the node displayed in column 1 is connected, i.e., the valent nodes.

3.7.2 Stage 2 – Obtain weight information from the finite element analysis

In stage 2, the weights or capacity for the flow network graph are obtained from the binary output database files produced by performing computational mechanics experiments on the bio-structure. The weights or capacity correspond to the parameter of interest, e.g., stress. A python script is also employed to carry out this task.

Table 3.1

Connectivity extracted from finite element model of bio-structure

Node ID	Total connecting nodes	ID of connecting nodes
1	6	3, 2, 4, 7, 30, 2073
2	11	3, 1, 4, 5, 6, 7, 8, 9, 30, 34, 36
3	9	1, 2, 4, 5, 6, 7, 10, 2073, 2074
4	12	2, 1, 3, 5, 30, 34, 33, 2073, 2074, 2075, 2092, 2093
5	7	2, 3, 6, 4, 34, 33, 35
6	6	3, 2, 5, 7, 9, 10
7	14	1, 2, 3, 8, 9, 6, 10, 36, 30, 37, 2073, 2094, 2095, 33091
8	5	2, 7, 9, 36, 330914
9	6	7, 8, 2, 6, 10, 330913
10	6	7, 6, 3, 9, 330915, 332045
11	6	13, 12, 14, 2076, 330984, 331025

3.7.3 Stage 3 – Generate DIMACS format files from connectivity and weight information

The third stage involves the production of a DIMACS formatted file [131] based on the weight or capacity of each node, as obtained in stage 2, and its connectivity information obtained in stage 1. In essence, the DIMACS file describes a network of interconnected nodes that forms an abstract structure known as a graph. A graph is a representation of information simplified as a collection of nodes, their weights, and the union between these nodes, which is known as an edge or a link. The DIMACS file for the notional flow network shown in Figure 3.19 is shown in Figure 3.20. The DIMACS file is created using a C++ program developed specifically for this research.

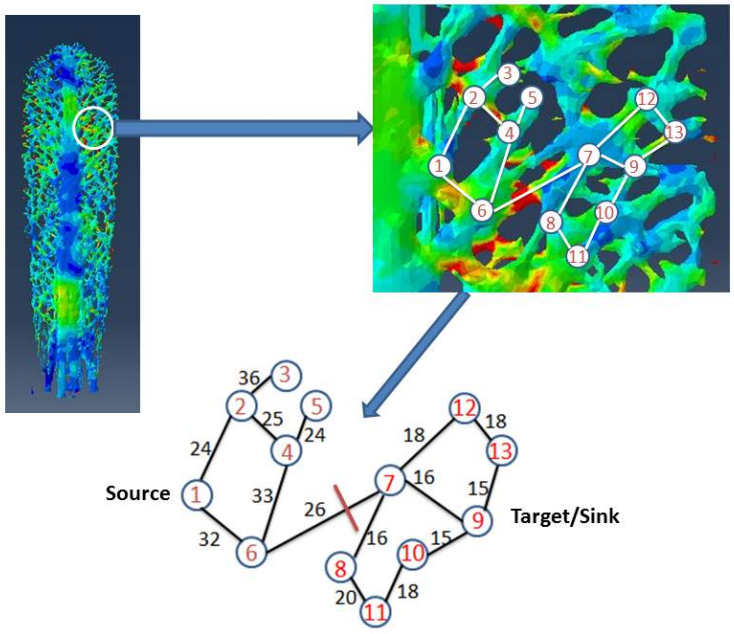

Figure 3.19

A demonstration model constructed from a small part of the rostrum to illustrate the modus operandi of maximum-flow/minimum-cut (MFMC) algorithm

```
c This is an example DIMACS format file
c created to represent the demonstration model
c Problem line (nodes, links)
p max 13 15
c source
n 1 s
c sink
n 9 t
a 1 2 24
a 1 6 32
a 2 3 36
a 2 4 25
a 6 4 33
a 4 5 24
a 6 7 26
a 7 12 18
a 7 9 16
a 7 8 16
a 8 11 20
a 13 9 15
a 10 9 15
a 12 13 18
a 11 10 18
c
c end of file
```

Figure 3.20

DIMACS format file for demonstration flow network represented by Figure 3.19

```
p max 13 10
c minimum cut, generated by BK
f 26
n 1 1
n 2 1
n 3 1
n 4 1
n 5 1
n 6 1
n 7 0
n 8 0
n 9 0
n 10 0
n 11 0
n 12 0
n 13 0
```

Figure 3.21

Output from the maximum-flow/minimum-cut algorithm

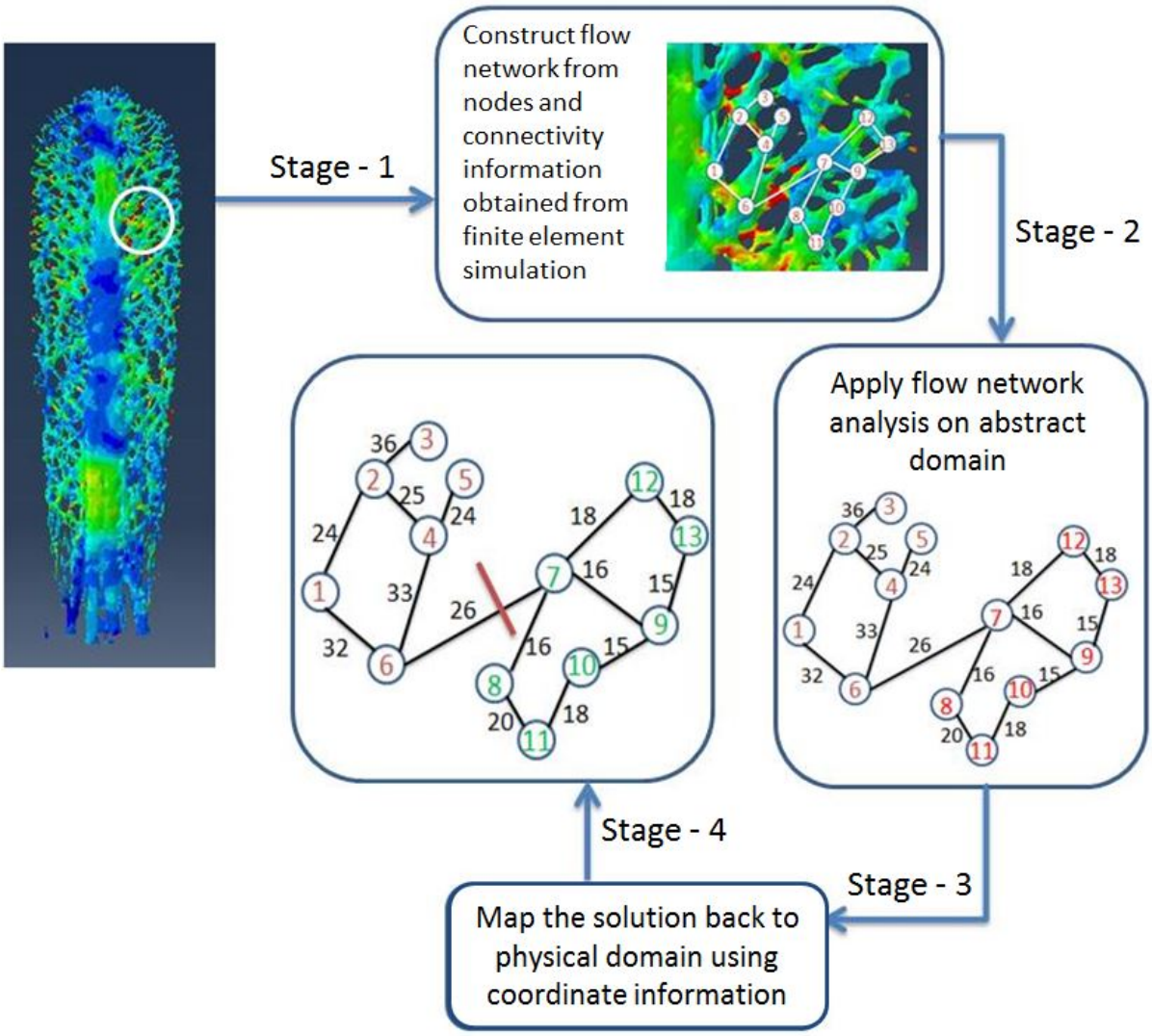

Figure 3.22

Flowchart depicting the formulation of a small part of rostrum as a network flow problem

3.7.4 Stage 4 – Run flow network analysis on the DIMACS file

The DIMACS file created using the procedure outlined in stage 3 is input to the maximum-flow/minimum-cut algorithm described in Boykov and Kolmogorov [132]. The theoretical worst case complexity of this algorithm is $O(nm^2|C|)$, where n represents the number of nodes, m represents the number of edges, and $|C|$ is the cost of the minimum-cut. Although the theoretical complexity of the algorithm is high, it outperforms standard algorithms used for identification of the minimum-cut in a graph [132]. Figure 3.21 shows the output obtained using the maximum-flow/minimum-cut algorithm. As shown in Figure 3.21, the maximum flow is 26. The maximum-flow/minimum-cut algorithm requires the source and sink to be in different subsets. Accordingly, the nodes get flagged as either 0 or 1 indicating that they belong to either the source or the sink, respectively. In a structural system, the maximum flow is the flow of stresses between nodes over all feasible routes without exceeding the strength of the system; furthermore, the minimum-cut will represent the location where the strength of the system is exceeded. The coordinate information for the nodes is extracted from the finite element input file. Paraview [133] is used to display the output of the maximum-flow/minimum-cut algorithm.

3.8 Summary

This chapter describes the integrated, interdisciplinary approach proposed in the current research. The capabilities of the software developed for this study can be summarized as follows:

1. The finite element model is developed in a Windows environment and the simulations are executed on ERDC's high performance computing systems because of the

size and complexity of the problem. The C++ program developed for this research is robust enough to tackle the issue of platform independency.

2. The rostrum is comprised of three component parts. When the data from the finite element simulations of the rostrum is mapped from the physical domain to the abstract domain, the software explicitly keeps track of the parts belonging to the different components. The software developed for analyzing the stress flow pattern is sufficiently robust to handle any structural system comprising variable constituent parts.

3. The numerical representation of the bio-structure has millions of degrees of freedom because of the geometrical complexity of the components. The nodes on the boundary of the components are shared by multiple regions. The C++ program keeps track of nodes belonging to a boundary region. The software has the capability to tackle highly complex and large datasets.

4. The user has the capability to view the results of the flow network computation for the three component parts of the rostrum together or separately.

CHAPTER IV

RESULTS

This chapter demonstrates the application of flow network approach for early identification of failure mechanisms in the rostrum of the paddlefish. Three displacement boundary conditions were used to analyze the effect of changing boundary conditions. A performance evaluation of five bio-inspired models was conducted using stress and deformation as metrics. This chapter also presents the application of similitude laws for blast loading on one of the bio-inspired models.

4.1 Identification of failure mechanisms in the rostrum of the paddlefish

Although computational mechanics experiments provide the overall distribution of stresses in the structural system, the information about the stress flow patterns formed in the nascent stages of loading are missing. Identification of the stress flow patterns in the linearly elastic regime may lead to novel insight into failure mechanisms through identification of the location of stress concentration areas developed in response to change in geometry or material properties. To obtain these stress patterns, the rostrum was formulated as a network flow model by utilizing the node and connectivity information from the finite element simulation. The network was weighted based on the Von-Mises stresses obtained from the output database file produced from the finite element experiments on

the rostrum. The maximum-flow/minimum-cut algorithm described in [132] was used to identify the stress flow patterns when the rostrum is subjected to a uniform pressure load. A seamless, platform-independent interface was developed to formulate the rostrum as network flow problem and compute the maximum-flow/minimum-cut of the network.

The flow network approach is used to validate the following research hypothesis stated in Chapter 1:

Testable Hypothesis-1: The rostrum is resilient because of enhanced toughening mechanisms. The toughening mechanisms in the rostrum may be attributed to the complex arrangement of lattice (fractal-like) skeletal structure. By using flow network approach, the failure mechanisms in the rostrum's complex geometry can be identified earlier when the material is still in the linearly elastic regime.

4.1.1 Finite element simulations

Finite element simulations were carried out on the rostrum of the paddlefish using the commercial software package Abaqus/Standard [123]. The simulations were performed on ERDC's High Performance Computing Modernization Program (HPCMP) Department of Defense (DoD) Supercomputing Resource Center (DSRC) located in Vicksburg, MS. The computational model was generated from the tomography (CT scan) of the paddlefish rostrum. Figure 3.14 through Figure 3.17 shows the outermost tissue, the inner hard cartilage, the innermost soft cartilage, and a cross section showing the mesh assembly. The component parts of the rostrum were individually imported into Abaqus. The parts were meshed using a combination of hexahedral and tetrahedral elements. The model used in the current

research comprises 119,712 hexahedral elements, 1,300,451 tetrahedral elements, 375,361 nodes, and 1,126,083 total degrees of freedom.

4.1.2 Material Properties

Nano-indentation experiments carried out on the rostrum revealed the material properties of the components of the rostrum [121]. Table 4.1 shows the three commercially available materials selected to represent the rostrum components shown in Figure 3.14 through Figure 3.17. Details of the materials used in the analysis are included in Appendix A.

Table 4.1

Commercial materials selected to model the components of rostrum.

Part	Commercial material	Elastic modulus
Tissue	Vinyl ester Epoxy	2.9 GPa
Hard Cartilage	Polyethylene Fibers	66 GPa
Soft Cartilage	Polyethylene/Epoxy(as isotropic)	49,762 MPa

4.1.3 Force and displacement boundary conditions

A uniform pressure of 50 MPa was applied on the top surface of the rostrum displayed in purple shading in Figure 4.1, Figure 4.2, and Figure 4.3. Three boundary conditions, i.e., fixed-plate, fixed-fixed, and cantilever beam, were selected to study of effects of boundary conditions on the stress flow pattern in the rostrum. The fixed-plate boundary condition was implemented on the rostrum by restraining the three components of displacement as

seen in Figure 4.1. The fixed-fixed boundary condition was implemented by restraining the displacement along two opposite edges of the rostrum as seen in Figure 4.2. The cantilever beam boundary condition was implemented by restraining the displacement along one edge of the rostrum as seen in Figure 4.3.

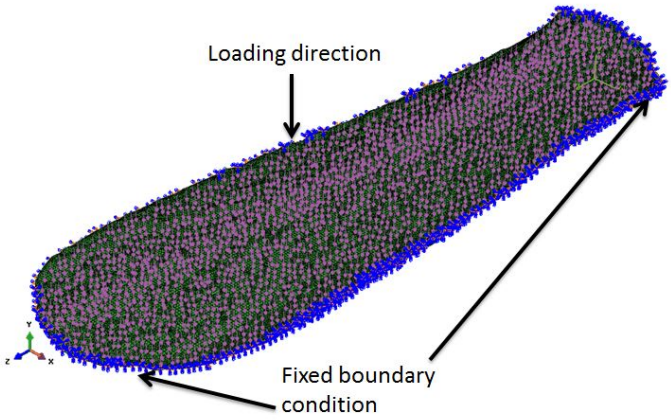

Figure 4.1

Fixed-plate boundary conditions implemented on the rostrum

4.1.4 Finite element experiment details

The Abaqus/Standard solver was used for conducting static analysis on the rostrum. The choice of Abaqus/Standard for performing these analyses is justified based on the algorithm that it employs for static and low-speed dynamic events wherein highly accurate stress solutions are required. Gravity is applied in the negative y-direction. Geometric non-linearity was taken into account in the simulations.

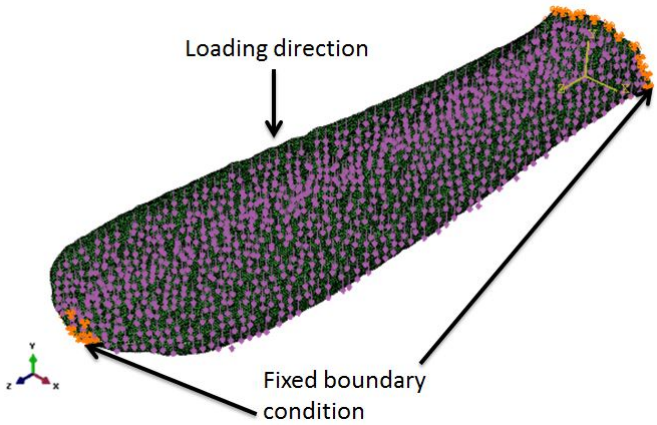

Figure 4.2

Fixed-fixed boundary conditions implemented on the rostrum

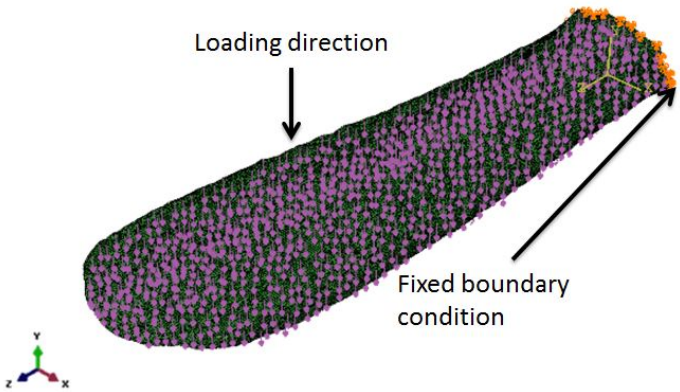

Figure 4.3

Cantilever beam boundary conditions implemented on the rostrum

4.1.5 Flow network analysis on the rostrum

Source and sink nodes were identified and provided as input to the maximum-flow/minimum-cut algorithm. The source and sink nodes were identified at the edges and center of the maximum displacement area on the top and bottom surfaces of the rostrum represented by red coloring in Figure 4.4. For the fixed-plate and fixed-fixed boundary condition, the same combinations of sources and sinks were used. For the cantilever beam boundary condition, the high stress areas were selected on the top and bottom surfaces to represent the source and sink nodes as shown in Figure 4.5. As verified earlier for the four-point simply-supported beam, the flow network algorithm was executed multiple times using the source-sink combination shown in Figure 4.4 and Figure 4.5 for each of the three boundary conditions in the current study. The results for each boundary condition were superimposed as the material was in the linearly elastic regime. Reversing the selection of source and sink nodes from the top to the bottom surfaces does not change the results obtained using the maximum-flow/minimum-cut algorithm. The network flow analysis indicates that the failure sites for the structural systems are located in the area where the minimum-cut is found as verified earlier in Chapter 3 for three- and four- point bending of a simply-supported concrete beam.

4.1.5.1 Flow network analysis of the soft cartilage of the rostrum

Figure 4.6(a) shows the maximum principal stresses on the bottom surface of the soft cartilage of the rostrum for the fixed-plate boundary condition. Although the stresses progressively increase in the early stages of loading, they were evenly distributed across the

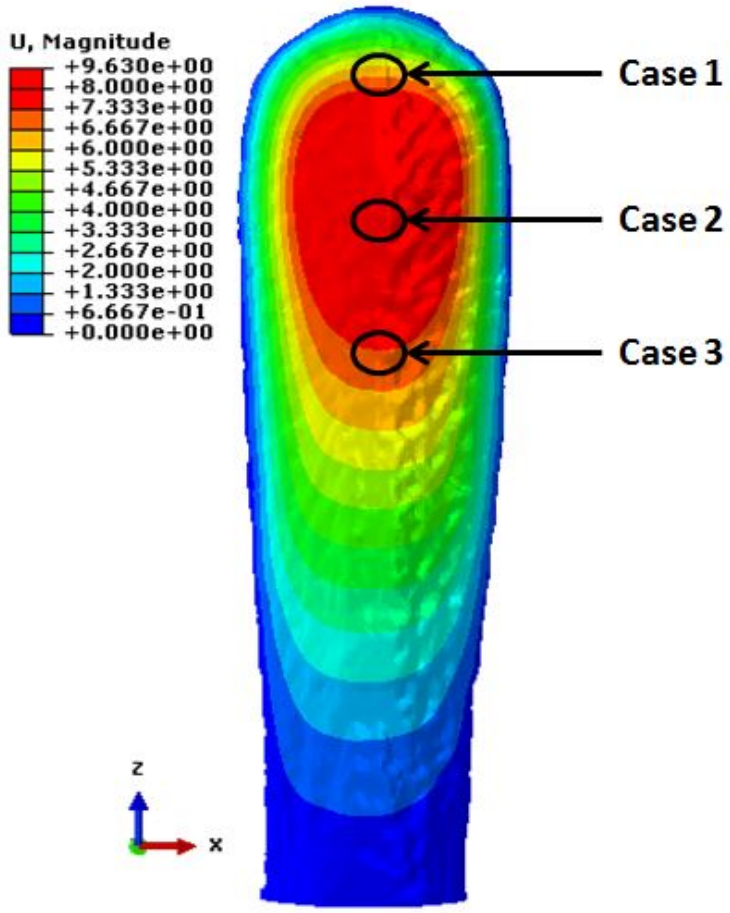

Figure 4.4

Displacement contours of the rostrum subjected to uniform pressure loading with a fixed-plate boundary condition showing the location of source/sink for fixed-plate and fixed-fixed boundary condition

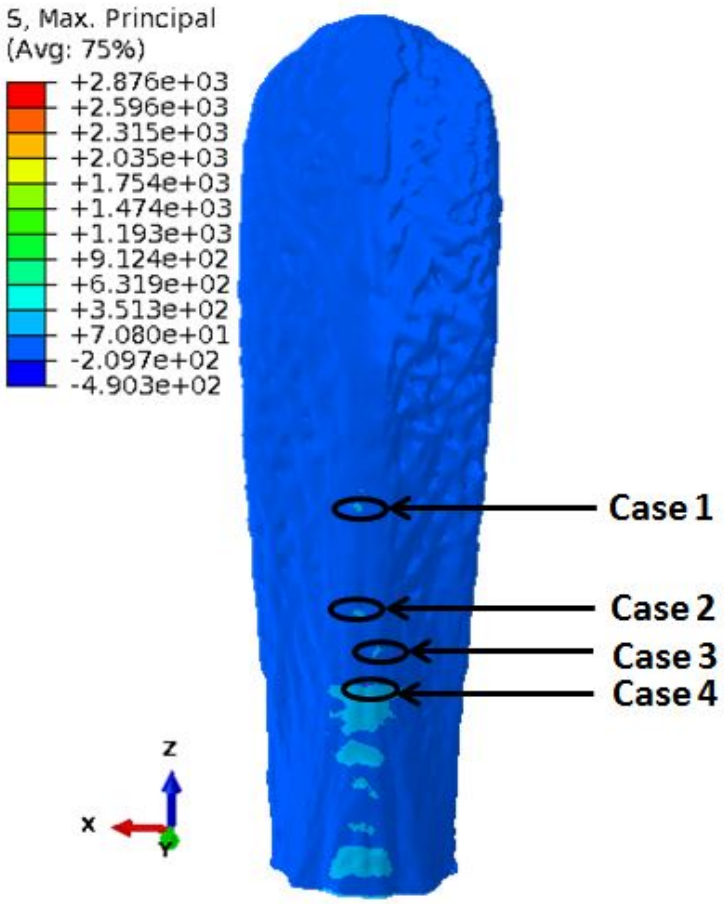

Figure 4.5

Stress contours of the rostrum subjected to uniform pressure loading with a cantilever beam boundary condition showing the location of source/sink

entire bottom surface thereby providing no insight into the failure mechanism. In contrast, Figure 4.6(b) displays the output obtained by executing the maximum-flow/minimum-cut algorithm using the source/sink combination shown Figure 4.4 and superimposing the results as previously validated for the case of four-point bending of a concrete beam in Section 3.4.2. Recall that the minimum-cut embodies a set of vertices that inhibits the transmission of information, i.e., stresses in the current analysis. The minimum-cut on the bottom surface of the soft cartilage occurs along the edges where there is a change in geometry and material properties. Based on the previous analysis for four-point bending of a simply-supported beam discussed in Section 3.4.2, which demonstrated that failure initiated on the minimum-cut, it is anticipated that failure will occur along these edges. The red regions at the tip and base of the bottom surface are also located in areas where the material properties change. The maximum-flow/minimum-cut algorithm has detected these candidate failure sites in the nascent stages of loading when the material is in the linearly elastic regime. The flow network approach reduced the computational cost and time since the finite element analysis did not have to be run until the structural system failed.

Figure 4.7(a) shows the maximum principal stresses on the bottom surface of the soft cartilage of the rostrum for the fixed-fixed boundary condition. Higher stresses are observed at the tip and base of the soft cartilage due to the fixed-fixed boundary condition. Figure 4.7(b) displays the output from maximum-flow/minimum-cut algorithm. The interface between the red and blue regions represents the locations of the minimum-cut. It is located at the tip, base, and along the edges where there is a change in material property as observed for the fixed-plate boundary condition.

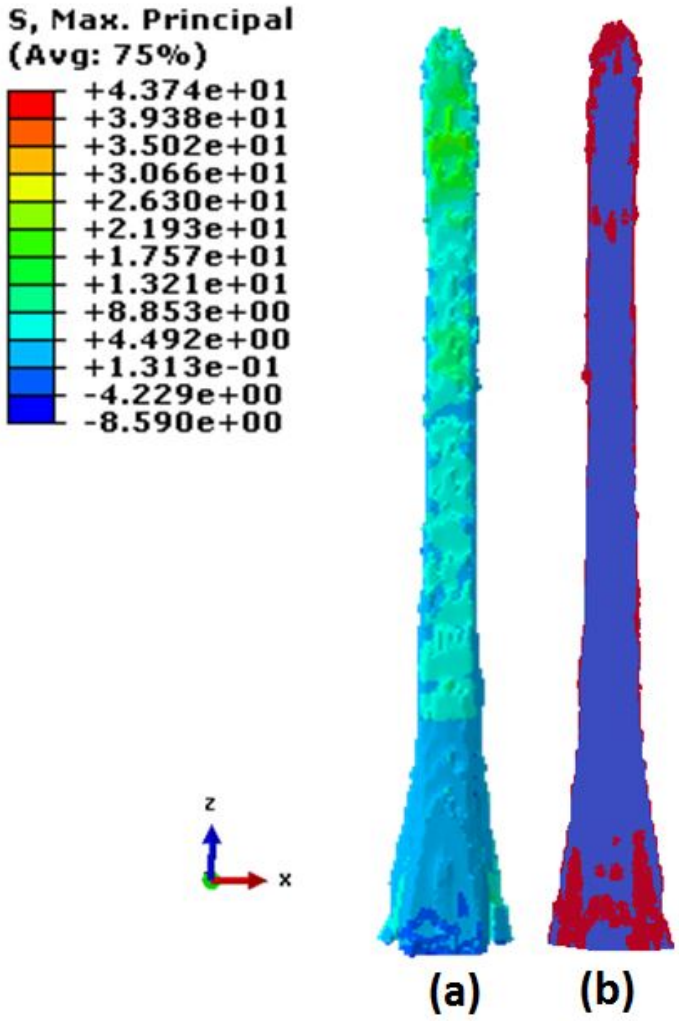

Figure 4.6

(a) Maximum principal stress obtained from finite element analysis (b) Minimum-cut obtained from flow network analysis on bottom surface of rostrums soft cartilage. The nodes are colored by their respective locations on the source (red) or sink (blue) side of the minimum-cut (Fixed-plate boundary condition).

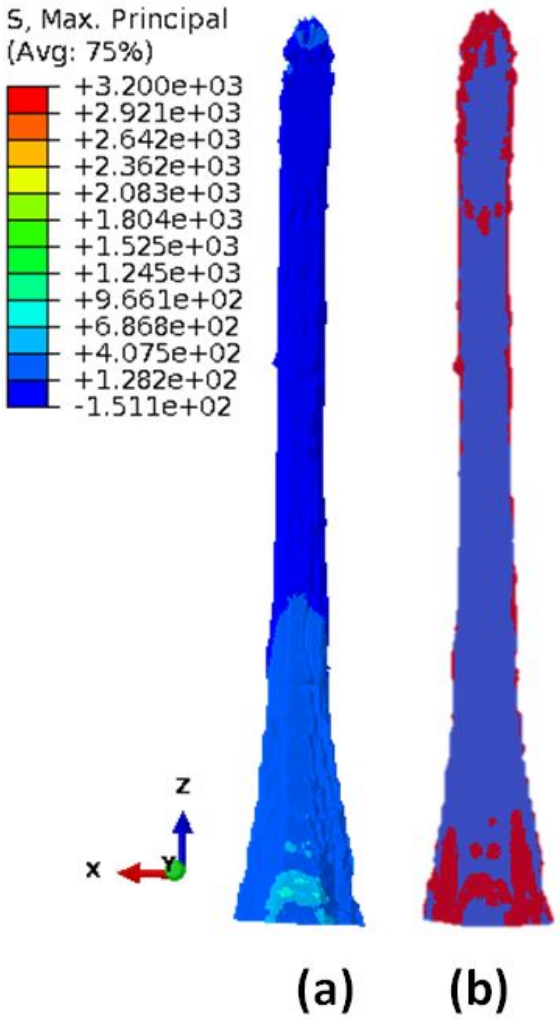

Figure 4.7

(a) Maximum principal stress obtained from finite element analysis (b) Minimum-cut obtained from flow network analysis on bottom surface of rostrums soft cartilage. The nodes are colored by their respective locations on the source (red) or sink (blue) side of the minimum-cut (Fixed-fixed boundary condition).

Figure 4.8(a) shows the maximum principal stresses on the bottom surface of the soft cartilage of the rostrum for the cantilever beam boundary condition. Higher stresses are observed at the tip of the bottom surface of the soft cartilage. This can be attributed to the cantilever beam boundary condition. Also, the peak stress value in the finite element analysis is lower for the cantilever beam boundary condition. This may be because the rostrum in its natural installation is optimized for performance for this type of restraint. The stresses progressively decrease from the base to the tip of the soft cartilage. Figure 4.8(b) displays the output from maximum-flow/minimum-cut algorithm. The minimum-cut is located at the tip, base, and along the edges in the regions where there is a change in material property as observed for the fixed-plate and fixed-fixed boundary conditions.

Figure 4.9(a) shows the maximum principal stresses on the top surface of the soft cartilage of the rostrum for the fixed-plate boundary condition. As observed previously in Figure 4.6(a), the finite element analysis shows the stresses progressively increase as the external load increases as expected. Figure 4.9(b) shows the minimum-cut obtained by running the maximum-flow/minimum-cut algorithm. The interface between the red and blue nodes is the location of the minimum-cut. The failure for the top surface of the rostrum will initiate along these edges as indicated by the network flow analysis. As before, there is a change in the material properties in these regions. Also, the red region at the base of the top surface occurs in the areas where there is a contact between components with different material properties. Hence, the flow network strategy has identified the regions where the failure mechanisms are expected to initiate.

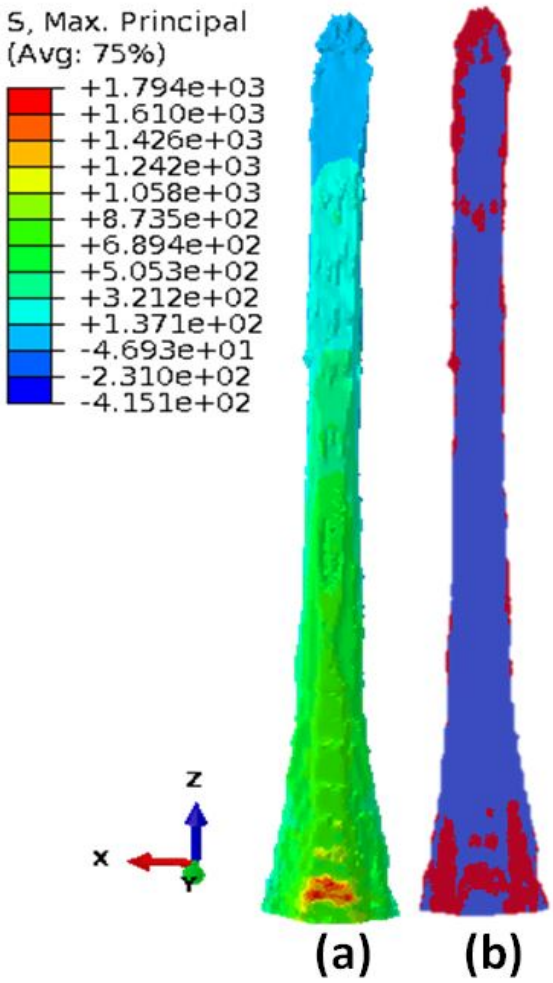

Figure 4.8

(a) Maximum principal stress obtained from finite element analysis (b) Minimum-cut obtained from flow network analysis on bottom surface of rostrums soft cartilage. The nodes are colored by their respective locations on the source (red) or sink (blue) side of the minimum-cut (Cantilever beam boundary condition).

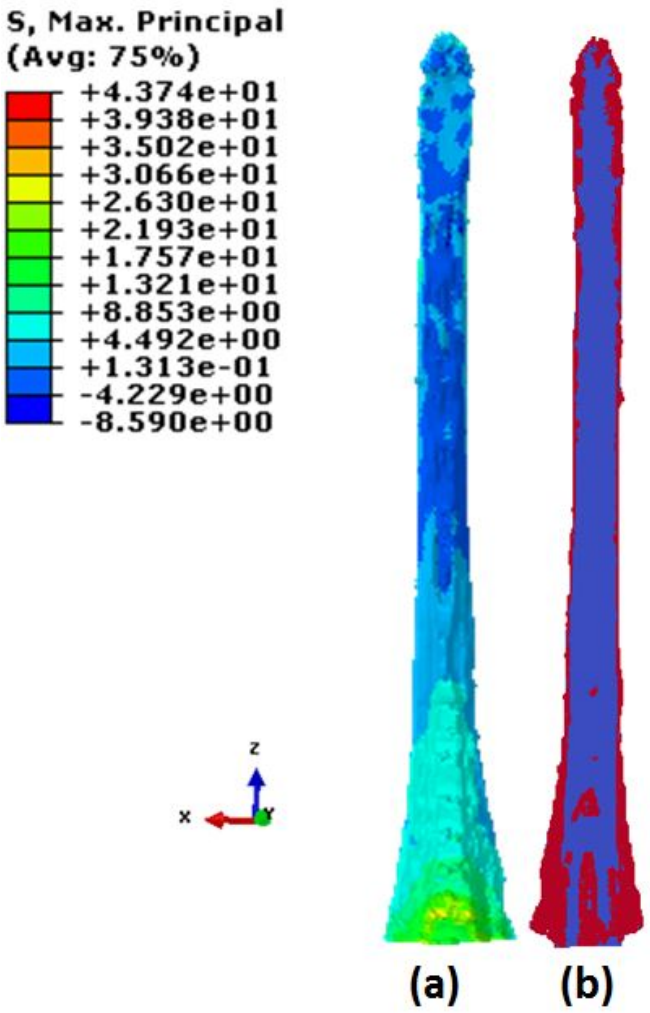

Figure 4.9

(a) Maximum principal stress obtained from finite element analysis (b) Minimum-cut obtained from flow network analysis on top surface of rostrum's soft cartilage. The nodes are colored by their respective locations on the source (red) or sink (blue) side of the minimum-cut (Fixed-plate boundary condition).

Figure 4.10(a) shows the maximum principal stresses on the top surface of the soft cartilage of the rostrum for the fixed-fixed boundary condition. A clear variation in the stress values is observed in the center region of the top surface because of the fixed-fixed boundary condition. Figure 4.10(b) shows the minimum-cut obtained by the maximum-flow/minimum-cut algorithm. The interface between the red and blue nodes is the location of the minimum-cut. The failure for the top surface of the rostrum will initiate along the edges based on the network flow analysis. There is a change in the material properties in this region. Also the red region at the base of the top surface occurs in the areas where there is a contact between components with different material properties. Hence, the flow network strategy has identified the local regions where the failure mechanisms are expected to initiate. The stress pattern from the maximum-flow/minimum-cut is similar for the fixed-plate and fixed-fixed bounday conditions.

Figure 4.11(a) shows the maximum principal stresses on the top surface of the soft cartilage of the rostrum for cantilever beam boundary condition. An even distribution of stress is seen on the top surface of the rostrum's soft cartilage for the cantilever beam boundary condition. Figure 4.11(b) shows the minimum-cut obtained by running the maximum-flow/minimum-cut algorithm. Based on the flow network analysis, failure on the top surface of the soft cartilage will initiate along the edges where there is a change in the material properties as observed for the fixed-plate and fixed-fixed boundary conditions earlier as indicated by the flow network analysis. Also the red region at the base of the top surface occurs in the areas where there is a contact between components with different material properties. Hence, the flow network strategy has identified the local regions where the

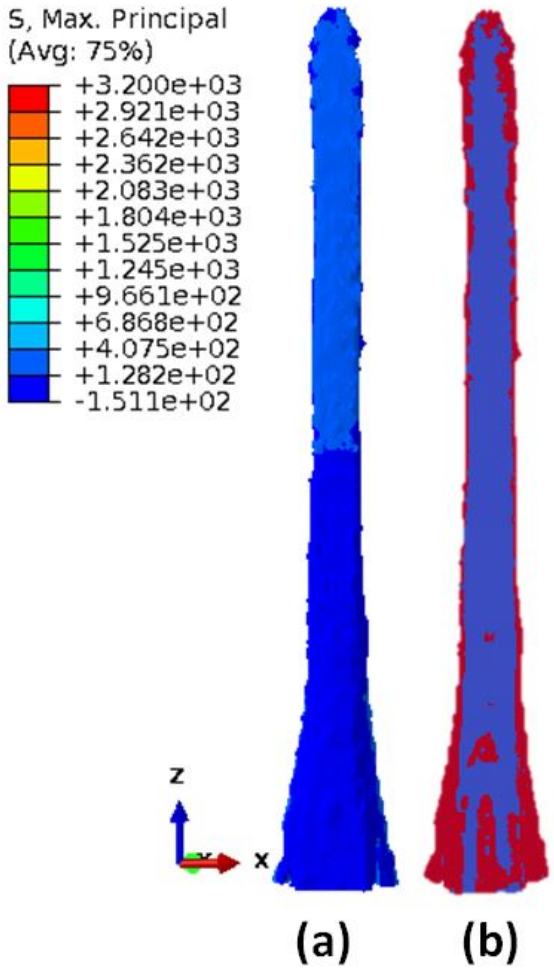

Figure 4.10

(a) Maximum principal stress obtained from finite element analysis (b) Minimum-cut obtained from flow network analysis on top surface of rostrum's soft cartilage. The nodes are colored by their respective locations on the source (red) or sink (blue) side of the minimum-cut (Fixed-fixed boundary condition).

failure mechanisms are expected to initiate. The stress flow pattern from the maximum-flow/minimum-cut is relatively insensitive to the type of boundary condition - fixed-plate, fixed-fixed, and cantilever. This suggests that the network flow analysis is capturing an intrinsic characteristic of the structural system that is independent of the boundary conditions.

4.1.5.2 Flow network analysis on the hard cartilage of the rostrum

Figure 4.12(a) shows the maximum principal stresses on the bottom surface of the hard cartilage part of the rostrum for the fixed-plate boundary condition. The overall stresses progressively increase with the increase in external loading as expected. Figure 4.12(b) displays the minimum-cut obtained from the maximum-flow/minimum-cut algorithm. The nodes are colored by their respective locations on the source (red) or sink (blue) side of the minimum-cut. The failure sites are located in the interface between the red and blue nodes. As seen in Figure 4.12(b), these regions are located in the center part of the hard cartilage. Since the lattice of the hard cartilage is not a continuous pattern, failure will not travel though the lattice region. The minimum-cut picks up a region in the lattice where the stress concentration is high and the nodes are prone to failure. The center part of Figure 4.12(b) clearly displays the strain localization, which is a typical mode of failure of a structural system under tensile loading. Hence, the research strategy implemented in the current work successfully identifies the failure mechanisms in the nascent stages of loading.

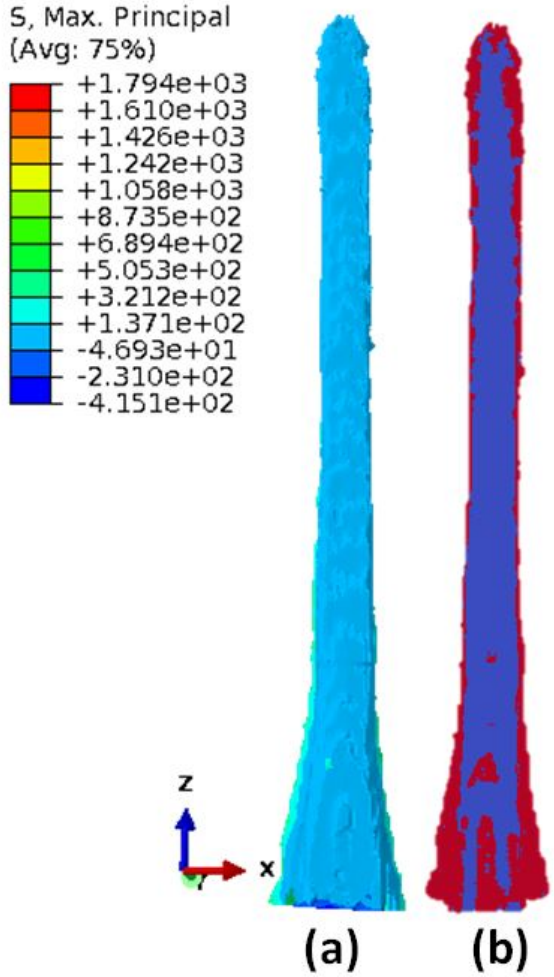

Figure 4.11

(a) Maximum principal stress obtained from finite element analysis (b) Minimum-cut obtained from flow network analysis on top surface of rostrum's soft cartilage. The nodes are colored by their respective locations on the source (red) or sink (blue) side of the minimum-cut (Cantilever beam boundary condition).

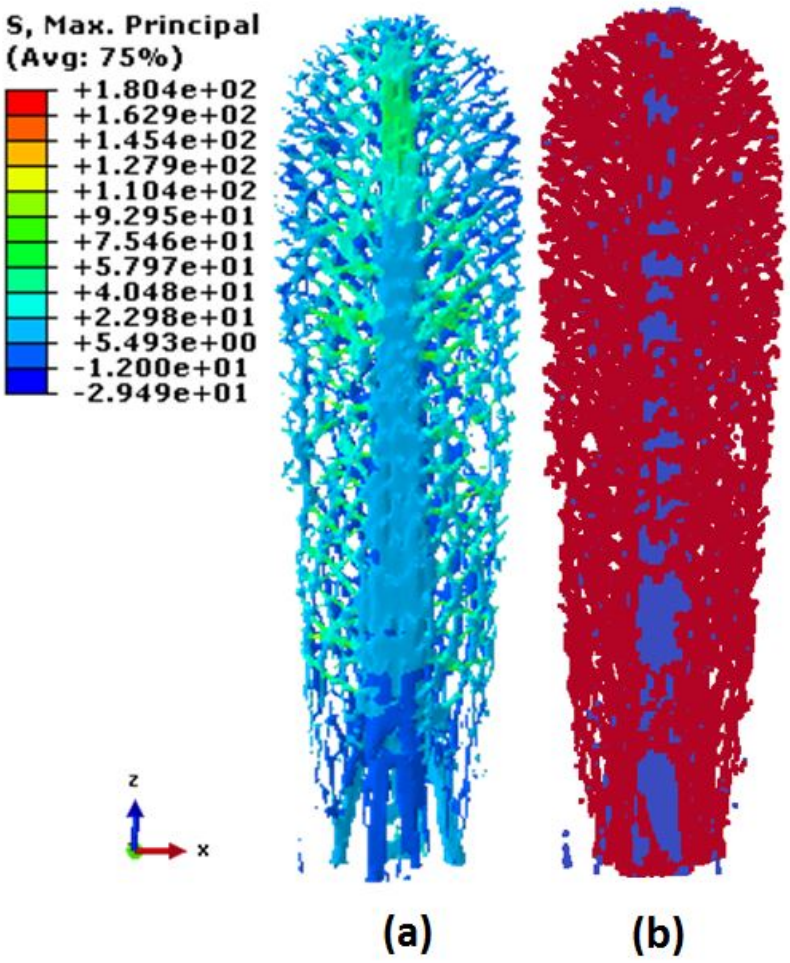

Figure 4.12

(a) Maximum principal stress obtained from finite element analysis (b) Minimum-cut obtained from flow network analysis on bottom surface of rostrum's hard cartilage. The nodes are colored by their respective locations on the source (red) or sink (blue) side of the minimum-cut (Fixed-plate boundary condition).

Figure 4.13(a) shows the maximum principal stresses on the bottom surface of the hard cartilage part of the rostrum for fixed-fixed boundary condition. A clear variation in stress is seen along the center bone of the hard cartilage. This may be the result of the fixed-fixed boundary condition. On the other hand, the stress flow pattern obtained by the maximum-flow/minimum-cut algorithm is visually similar to the one obtained with the fixed-plate boundary condition. The minimum-cut is located in the regions where the center bone attaches to the lattice structure and there is a variation in geometry of the structural system as seen in Figure 4.13(b). Also, strain localization is clearly visible in the center region of the hard cartilage very similar to that observed for the fixed-plate boundary condition.

Figure 4.14(a) shows the maximum principal stresses on the bottom surface of the hard cartilage part of the rostrum for cantilever beam boundary condition. Higher stresses are observed towards the base of the hard cartilage. This is the result of the cantilever beam boundary condition. On the other hand, the pattern obtained by the maximum-flow/minimum-cut algorithm is visually similar to the ones obtained with the fixed-plate and fixed-fixed boundary conditions. The minimum-cut is located in the regions where the center bone attaches to the lattice structure and there is a variation in geometry as seen in Figure 4.14(b). Also, strain localization is clearly visible in the center region of the hard cartilage very similar to that observed for the fixed-plate and fixed-fixed boundary condition.

Figure 4.15(a) displays the maximum principal stresses on the top surface of the hard cartilage of the rostrum for fixed-plate boundary condition. Although the finite element analysis gives the overall distribution of stresses in the structural system, the underlying

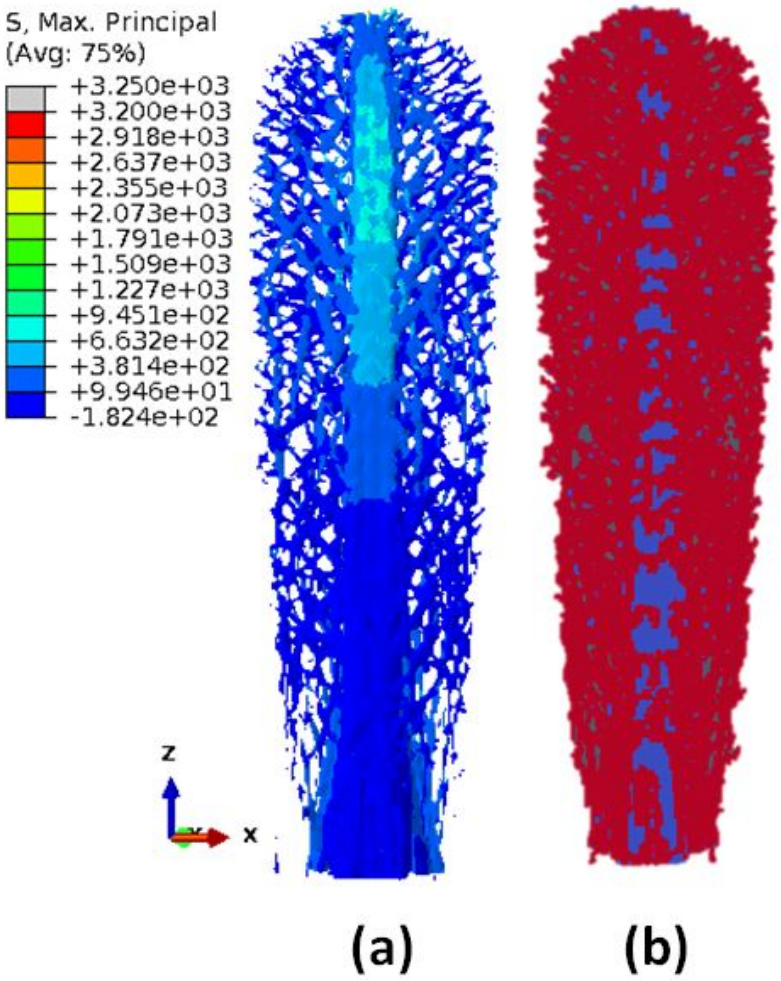

Figure 4.13

(a) Maximum principal stress obtained from finite element analysis (b) Minimum-cut obtained from flow network analysis on bottom surface of rostrum's hard cartilage. The nodes are colored by their respective locations on the source (red) or sink (blue) side of the minimum-cut (Fixed-fixed boundary condition).

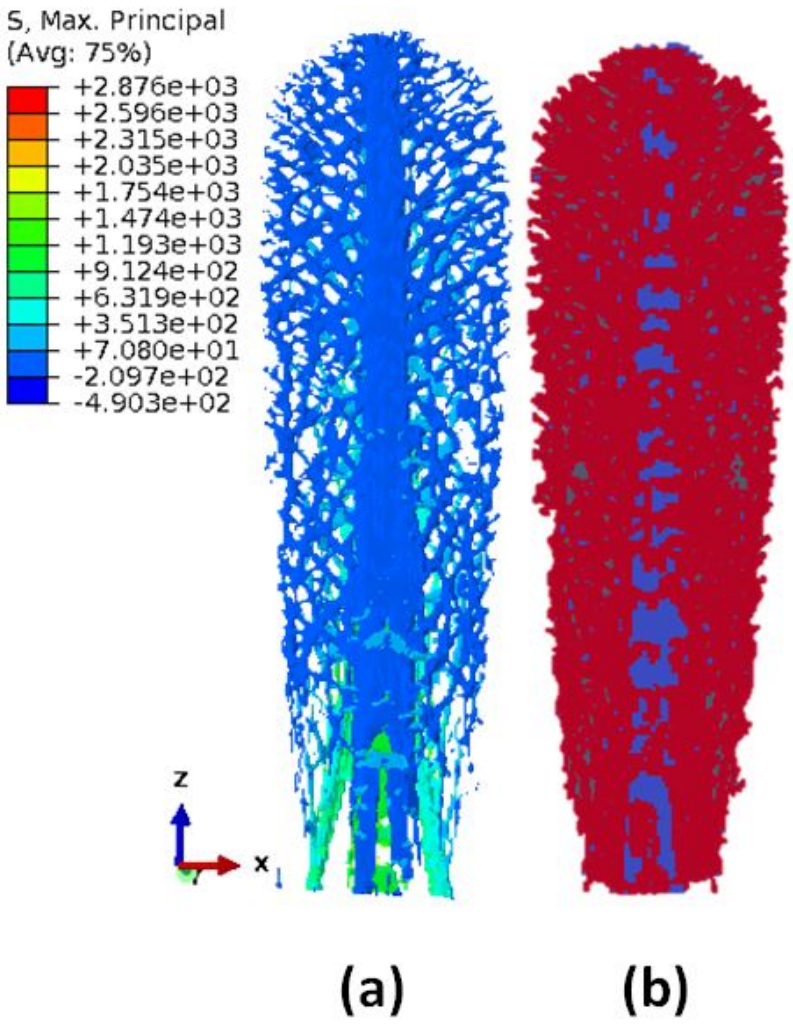

Figure 4.14

(a) Maximum principal stress obtained from finite element analysis (b) Minimum-cut obtained from flow network analysis on bottom surface of rostrum's hard cartilage. The nodes are colored by their respective locations on the source (red) or sink (blue) side of the minimum-cut (Cantilever beam boundary condition).

details that govern the phenomena of failure mechanism are hard to determine from the stresses before failure. Figure 4.15(b) on the contrary shows the minimum-cut obtained by executing the maximum-flow/minimum-cut algorithm. The central part of Figure 4.15(b) clearly highlights the crushing/buckling behavior that is typically seen in compressive failure. Also, a majority of the failure sites are located in the region where there is a change of geometry and material properties. Again, the current methodology has identified the sites of failure in the nascent stages of loading.

Figure 4.16(a) displays the maximum principal stresses on the top surface of the hard cartilage of the rostrum for fixed-fixed boundary condition. The overall stresses progressively increase with the increase in external load. Figure 4.16(b) shows the minimum-cut obtained by the maximum-flow/minimum-cut algorithm. The central part of Figure 4.16(b) clearly highlights the crushing/buckling behavior that is typically seen in compressive failure. Also, a majority of the failure sites in this case are located in the region where there is a change of geometry and material properties.

Figure 4.17(a) displays the maximum principal stresses on the top surface of the hard cartilage of the rostrum for the cantilever boundary condition. The overall stresses progressively increase with the increase in external load as observed for the fixed-plate and fixed-fixed boundary condition. Also, higher stresses are observed on the base of the hard cartilage due to the cantilever beam boundary condition. Figure 4.17(b) shows the minimum-cut obtained by executing the maximum-flow/minimum-cut algorithm. The central part of Figure 4.17(b) clearly highlights the crushing/buckling behavior that is typically seen in compressive failure.

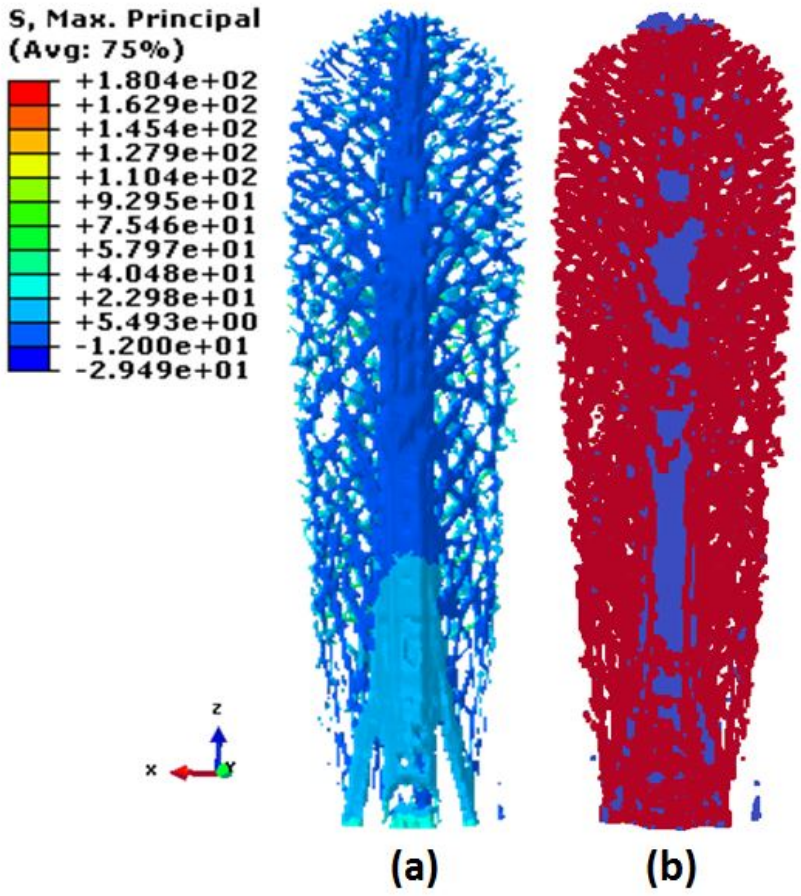

Figure 4.15

(a) Maximum principal stress obtained from finite element analysis (b) Minimum-cut obtained from flow network analysis on top surface of rostrum's hard cartilage. The nodes are colored by their respective locations on the source (red) or sink (blue) side of the minimum-cut (Fixed-plate boundary condition).

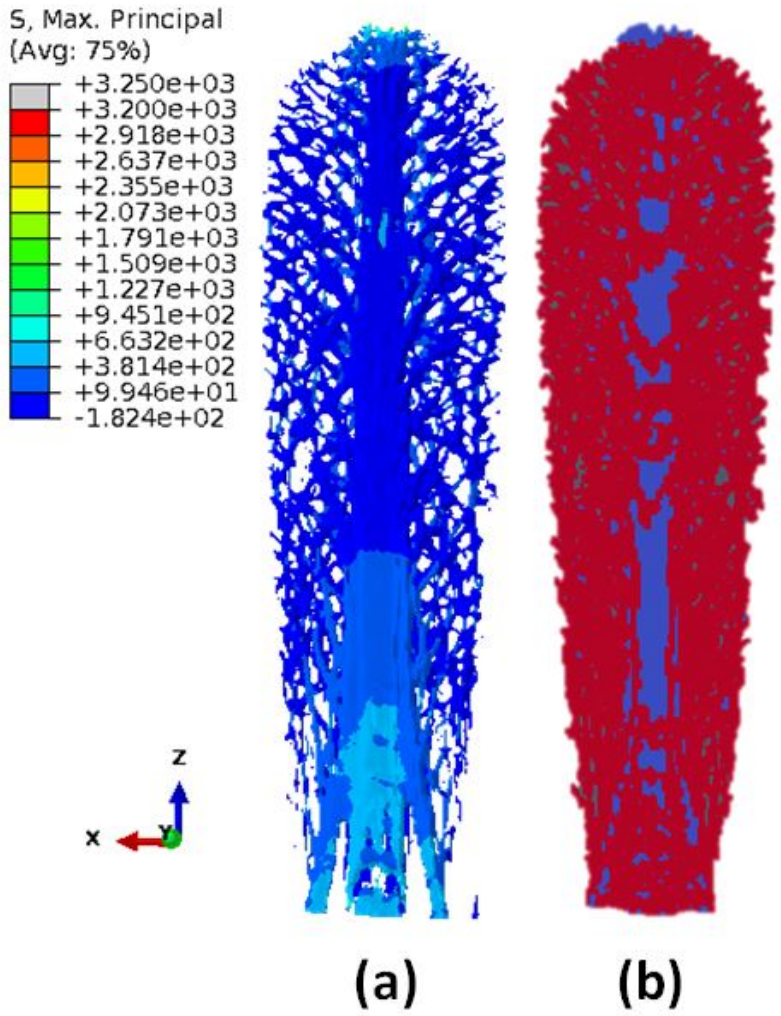

Figure 4.16

(a) Maximum principal stress obtained from finite element analysis (b) Minimum-cut obtained from flow network analysis on top surface of rostrum's hard cartilage. The nodes are colored by their respective locations on the source (red) or sink (blue) side of the minimum-cut (Fixed-fixed boundary condition).

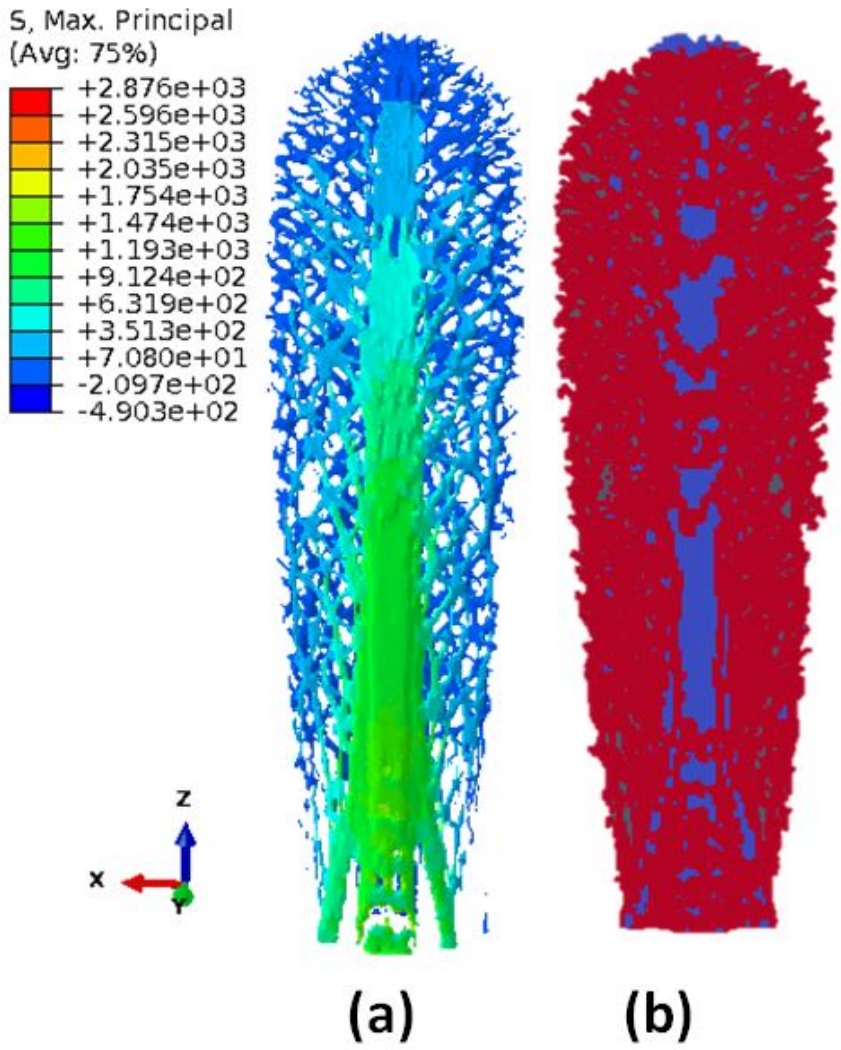

Figure 4.17

(a) Maximum principal stress obtained from finite element analysis (b) Minimum-cut obtained from flow network analysis on top surface of rostrum's hard cartilage. The nodes are colored by their respective locations on the source (red) or sink (blue) side of the minimum-cut (Cantilever beam boundary condition).

4.1.5.3 Flow network analysis on tissue of the rostrum

Figure 4.18(a) shows the minimum-cut obtained from the flow network analysis on the bottom surface of the rostrum using the source-sink combination shown Figure 4.4 for the fixed-plate boundary condition. As seen in Figure 4.18 (a), the flow network captures the failure patterns at much earlier stages of loading that are not evident in the finite element results shown in Figure 4.18(b). At lower pressures, the strain localization patterns are captured on the tip of the central region of Figure 4.18(a). As the pressure increases, strain localization patterns are formed all along the central region of the tissue of the rostrum. Truss-like patterns are captured as seen in Figure 4.18(a). In contrast, the maximum principal stresses seen in Figure 4.18(b) do not show evidence of such patterns. The strain localization patterns captured through the flow network strategy are typically observed in a structural system under tensile loading. Also, at a pressure of 7.143 MPa, Figure 4.18(a) does not show any failure sites at the base of the tissue part of the rostrum indicative of it being stronger than the other components of the rostrum. This is the region that is attached to the mouth of the paddlefish and this particular structural system is optimized for this particular type of restraint. The flow network strategy captures this pattern in the nascent stages of loading when the material is still in the linearly elastic regime.

Figure 4.19(a) shows the minimum-cut obtained from the flow network analysis on the bottom surface of the rostrum using the source-sink combination shown Figure 4.4 for the fixed-fixed boundary condition. As seen in Figure 4.19 (a), the flow network captures the failure patterns at much earlier stages of loading that are not evident in the results shown in Figure 4.19(b). At a pressure of 1.428 MPa, the flow network captures the strain

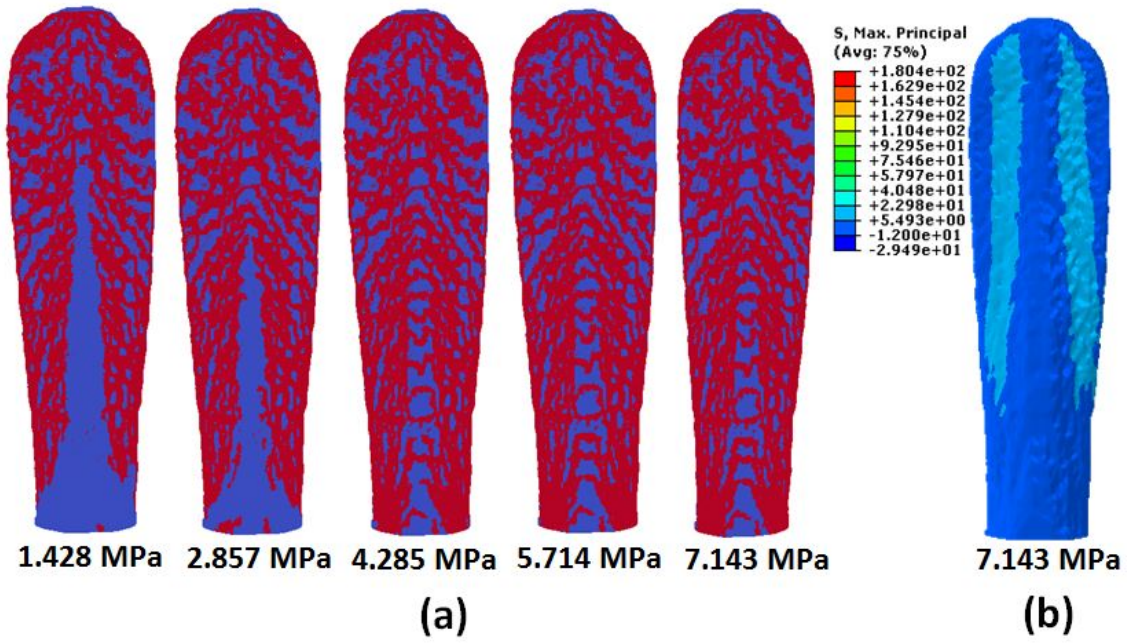

Figure 4.18

(a) Network flow analysis on the bottom surface of rostrum subjected to uniform pressure loading with a fixed-plate boundary condition. The nodes are colored by their respective locations on the source (red) or sink (blue) side of the minimum-cut. (b) Maximum principal stresses on the bottom surface of rostrum (Fixed-plate boundary condition).

localization in the center region as well as patterns on the edges of the rostrum that may be a result of the fixed-fixed boundary condition. As the pressure increases, truss like patterns are again evident. Also, the base of the rostrum does not show any minimum-cuts towards the right and left sides indicating that these are the strongest parts of the rostrum.

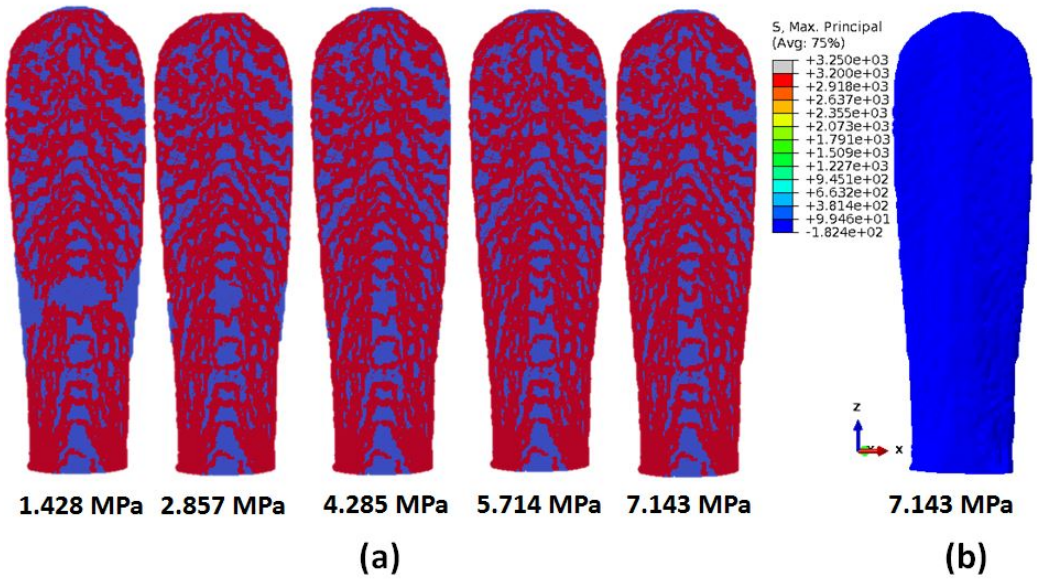

Figure 4.19

(a) Network flow analysis on the bottom surface of rostrum subjected to uniform pressure loading with a fixed-plate boundary condition. The nodes are colored by their respective locations on the source (red) or sink (blue) side of the minimum-cut. (b) Maximum principal stresses on the bottom surface of rostrum (Fixed-fixed boundary condition).

Figure 4.20(a) shows the minimum-cut obtained from the flow network analysis on the bottom surface of the rostrum using the source-sink combination shown in Figure 4.4 for the cantilever beam boundary condition. As seen in Figure 4.20 (a), the flow network captures the anticipated failure patterns at much earlier stages of loading that are not evident in

the computational mechanics results shown in Figure 4.20(b). The flow network displays minimum-cuts towards the base region until the external loading pressure reaches 4.285 MPa. This behaviour may be attributed to the fact that rostrum is optimized in nature for a cantilever beam boundary condition. As the pressure increases, truss-like patterns develop. Also, the base of the rostrum does not show any minimum-cuts towards the right and left sides indicating that these are the strongest parts of the rostrum.

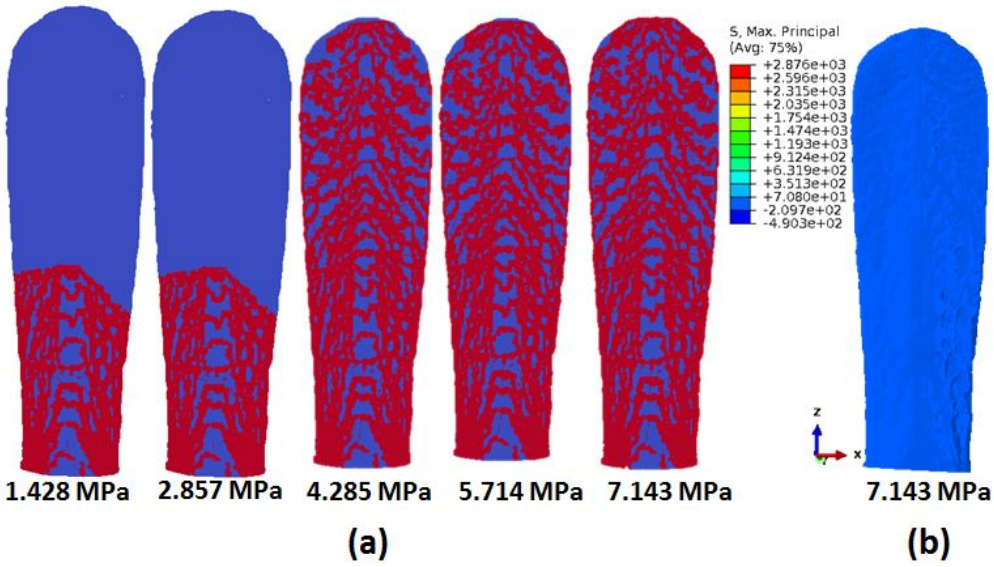

Figure 4.20

(a) Network flow analysis on the bottom surface of rostrum subjected to uniform pressure loading with a fixed-plate boundary condition. The nodes are colored by their respective locations on the source (red) or sink (blue) side of the minimum-cut. (b) Maximum principal stresses on the bottom surface of rostrum (Cantilever beam boundary condition).

Figure 4.21(a) displays the minimum-cut obtained using the flow network approach on the top surface of the rostrum for the fixed-plate boundary condition. As seen in Figure 4.21

(a), at lower stresses, the minimum-cut is clearly formed on the right and left sides of the rostrum. These are the regions where the material properties of this component of the rostrum change drastically. As the pressure increases, patterns are formed in the center and base regions. Also, as the pressure increases in Figure 4.21(a), there is an absence of failure sites at the left and right corners of the base region of the rostrum. This behavior is similar to the one observed on the top surface of the rostrum and is indicative of the identification of the stronger part of the rostrum during the nascent stages of loading.

Figure 4.22(a) displays the minimum-cut obtained using the flow network approach on the top surface of the rostrum for the fixed-fixed boundary condition. As seen in Figure 4.22(a), at lower pressures, minimum-cuts are located at the edges of the rostrum that do not have a displacement boundary condition. As the pressure increases, the patterns observed from the flow network analysis for the fixed-fixed boundary condition are similar to the fixed-plate boundary condition. In contrast, Figure 4.22(b) shows the maximum principal stresses from the finite element analysis. Although the tip of the rostrum shows high pressure, the details captured by the flow network analysis in the nascent stages of loading are missing. Hence, the proposed approach has identified the anticipated failure patterns earlier than a finite element analysis.

Figure 4.23(a) displays the minimum-cut obtained using the flow network approach on the top surface of the rostrum for the cantilever beam boundary condition. As seen in Figure 4.23(a), at lower pressures, the flow network identifies the minumum-cuts towards the base of the rostrum. As the external pressure reaches 4.285 MPa, the minimum-cut grows over the top surface. The minimum-cut shows identical patterns of buckling/crushing be-

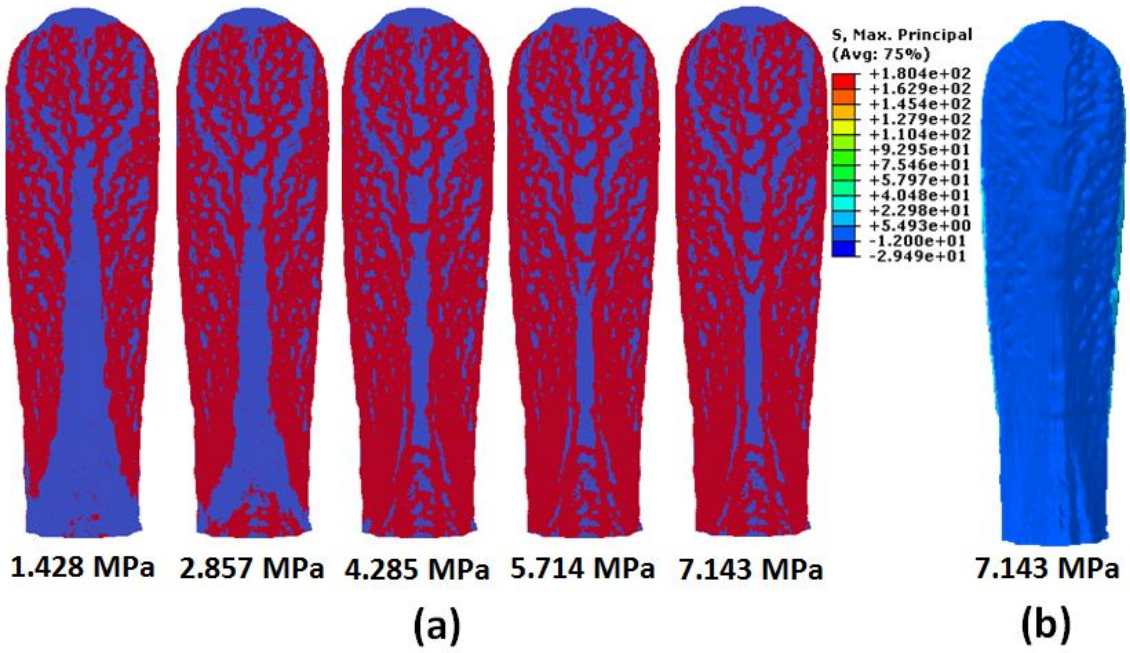

Figure 4.21

(a) Network flow analysis on the top surface of rostrum subjected to uniform pressure loading with a fixed-plate boundary condition. The nodes are colored by their respective locations on the source (red) or sink (blue) side of the minimum-cut. (b) Maximum principal stresses on the bottom surface of rostrum (Fixed-plate boundary condition).

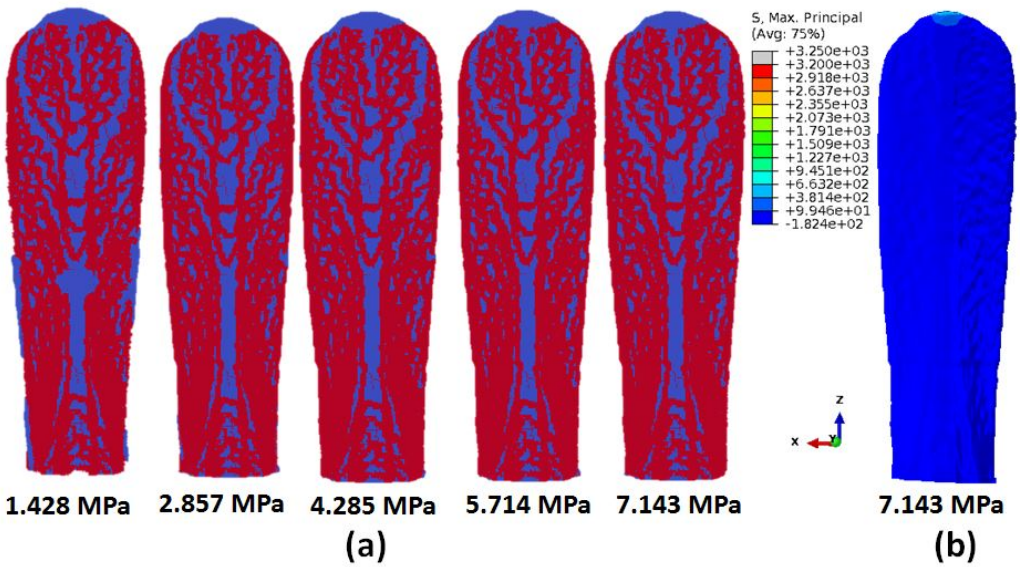

Figure 4.22

(a) Network flow analysis on the top surface of rostrum subjected to uniform pressure loading with a fixed-plate boundary condition. The nodes are colored by their respective locations on the source (red) or sink (blue) side of the minimum-cut. (b) Maximum principal stresses on the bottom surface of rostrum (Fixed-fixed boundary condition).

haviour as seen for the fixed-plate and fixed-fixed boundary condition. The stresses obtained from the finite element analysis show peak values in the center region towards the base of the rostrum as seen in Figure 4.23(b), but the details of the anticipated failure mechanisms captured by the flow network strategy are missing.

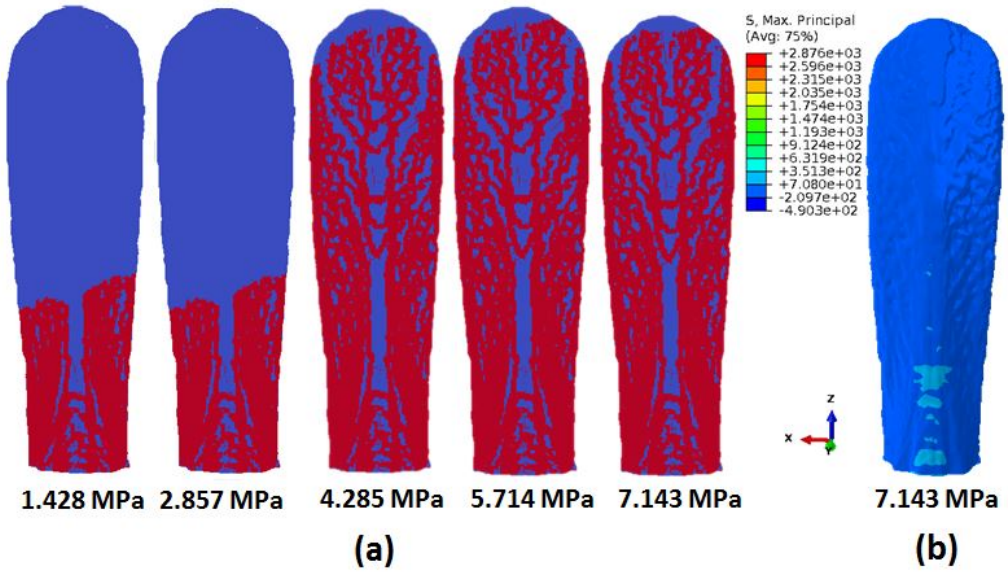

Figure 4.23

(a) Network flow analysis on the top surface of rostrum subjected to uniform pressure loading with a fixed-plate boundary condition. The nodes are colored by their respective locations on the source (red) or sink (blue) side of the minimum-cut. (b) Maximum principal stresses on the bottom surface of rostrum (Cantilever beam boundary condition).

4.1.6 Performance of the software in parallel

The software developed for the current research keeps track of the coordinate information of the nodes when the results from the finite element analysis for the ros-

trum are mapped to the abstract domain to facilitate formulation as a network flow problem. Computations are performed on the abstract, physics-free domain and the solution is mapped back to the physical domain using the coordinate information associated with the nodes. Since the finite element simulations produce large datasets, OpenMP is used to parallelize the procedure developed to formulate the rostrum as a flow network problem. OpenMP (Open Multi-Processing) is an application programming interface (API) that supports multi-platform shared memory multiprocessing programming in C, C++, and FORTRAN [134] on most platforms including Solaris, AIX, HP-UX, Linux, macOS, and Windows. OpenMP is a method of parallelizing in which a master thread forks out a specified number of slave threads and the system distributes the assigned tasks among them. The performance of the software in parallel is presented in the following sub-sections.

4.1.6.1 Run time and speedup

The runtime of a serial program is the time taken for the program to execute on a single processor. The parallel run time is defined as the time taken from the moment that the parallel execution starts to the time that the last processor finishes its assigned task. Figure 4.24 displays the runtime of the software in parallel. The input size is held constant as the number of threads is increased. As seen from Figure 4.24, the software shows a performance improvement until 10 threads are used. As the number of threads increases beyond 10, no performance gain is observed. Therefore, the optimal number of threads for processing the dataset analyzed in this instance is 10.

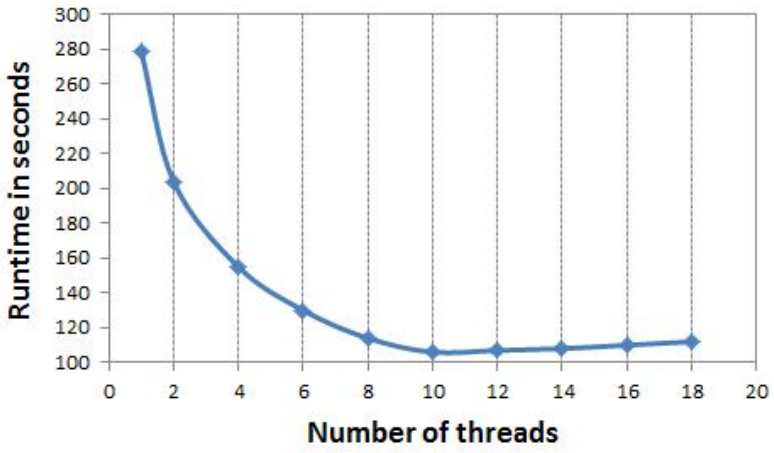

Figure 4.24

Runtime versus number of threads of the software implemented on rostrum

An alternative performance metric is speedup. Speedup establishes the advantage of solving a given problem using parallel computing and is defined as the ratio of the time taken to run a problem using a single processor to the time taken to solve the same problem using parallel computing [135]. Figure 4.25 shows the speedup as a function of number of threads. As seen in Figure 4.25, speedup is 1 for sequential implementation and steadily increases until 10 threads are used. Using threads greater than 10 will not produce any performance gain for the current problem. In fact, the speedup steadily decreases with increasing the threads after the number beyond 10. As before, the problem size is held steady as the number of threads is increased.

4.2 Performance analysis of the bio-inspired structural systems

Lightweight structures are in high demand in many application areas because they deliver an optimum use of available resources. However, lightweight structures are required

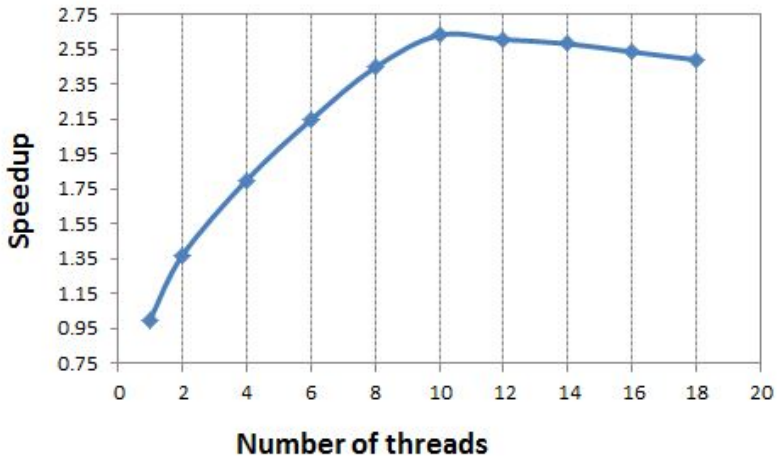

Figure 4.25

Speedup versus number of threads of the software implemented on rostrum

to have acceptable strength for safe usage. This section validates the testable hypothesis presented below by analyzing the performance of five proof-of-concept structural systems based on the rostrum (snout) of the paddlefish. The performance of each model was quantified in terms of deformations and maximum principal stresses experienced under a constant uniform pressure using a fixed-plate boundary condition.

Testable Hypothesis-2: If the failure mechanisms of the resilient lattice bio-structural systems are dependent on the geometrical arrangements, then structures with more complex geometries will have more resilience than structures with lower complexity.

This hypothesis was tested by conducting computational mechanics experiments on conceptual prototypes of bioinspired, energy-dissipative mechanical system models inspired from the rostrum of paddlefish with several lattice patterns.

4.2.1 Bio-inspired model composition

The hypothesis of this research is that the rostrum′s superior performance is a function of its complex lattice architecture and heterogeneous material properties; therefore, the model structures should likewise incorporate lattice architecture and heterogeneous material properties. Five notional representations of bio-inspired structural systems were investigated. Figure 4.26 shows the five lattice patterns (square box, cross box, open box, solid plate, and crisscross box) developed to obtain understanding of the role played by the complexity of the lattice architecture on the resilience of the structural systems. The models were built using Abaqus CAE. Figure 4.27 shows the components of the rostrum and the bio-inspired models. The dimensions of the notional structural systems were similar to those of the rostrum as shown in Figure 4.28. The materials in Table 4.1 were used for these models. Table 4.2 displays the details of the computational mesh of the five models. Details of the analysis follow in the subsequent sections.

Table 4.2

Mesh details of the bio-inspired models used in finite element analysis

Model	Nodes	Elements	Hexahedral elements	Tetrahedral elements	Wedge elements
Open box	228984	213180	213180	0	0
Square box	877532	208152	208152	0	0
Cross box	998739	714264	141552	572712	0
Crisscross box	841152	626809	182683	443966	160
Solid plate	445508	104667	104667	0	0

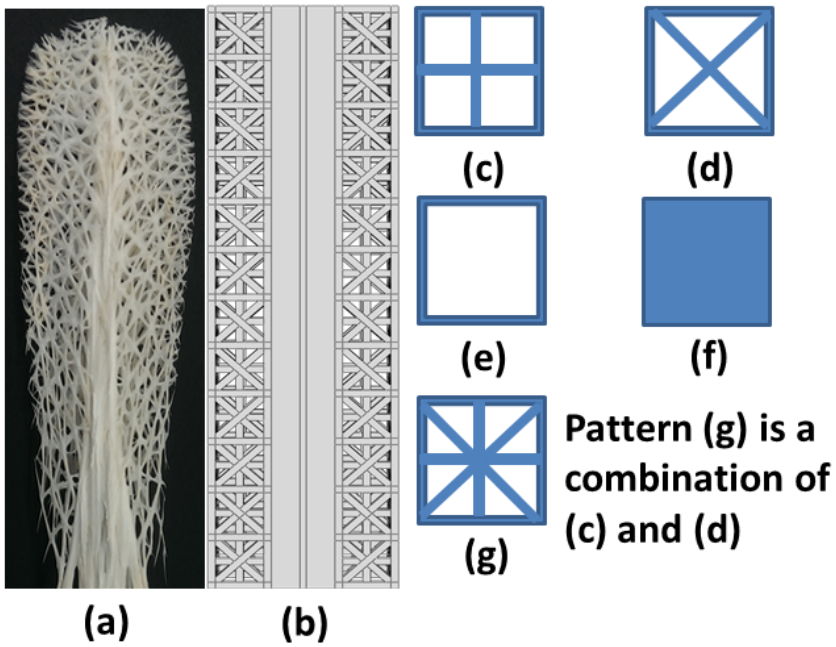

Figure 4.26

(a) Indeterminate lattice architecture of the rostrum. (b) A representative composite structure developed for this study with the different lattice architecture shown (c) square box, (d) cross box, (e) open box, (f) solid plate, and (g) crisscross box pattern.

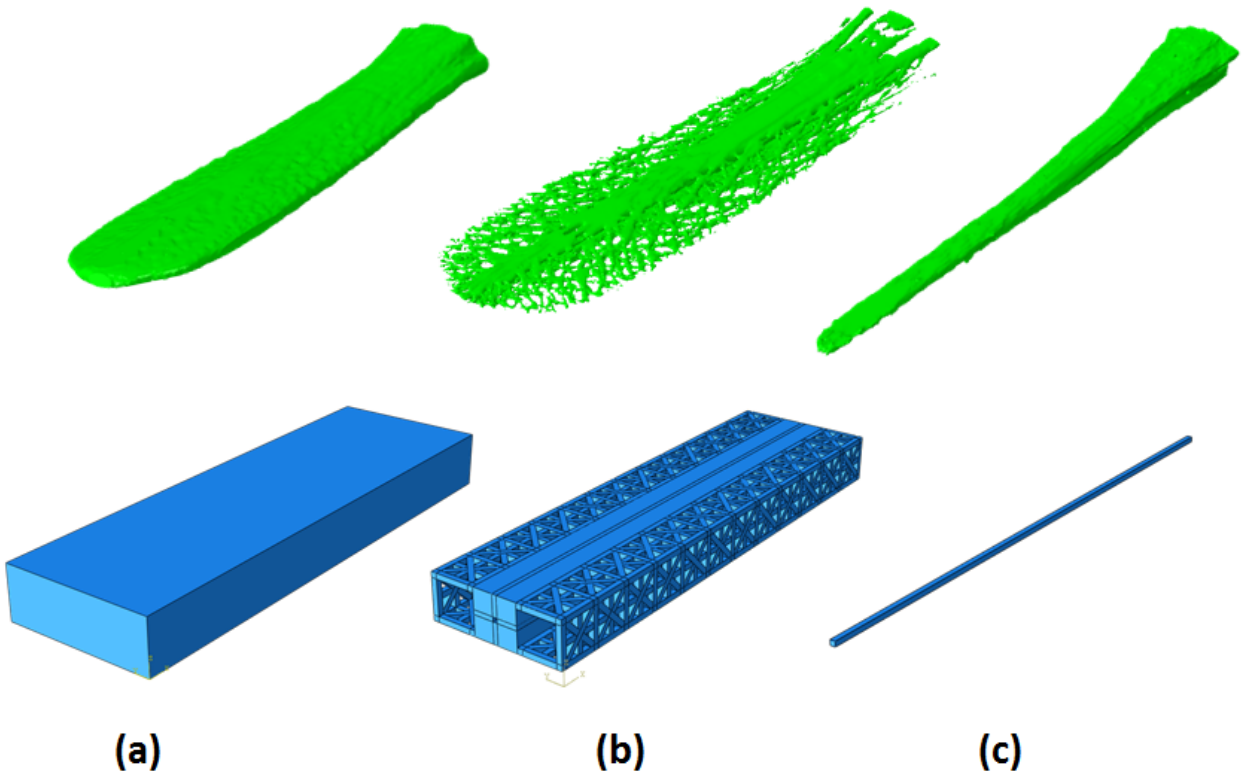

Figure 4.27

Top row (a) tissue, (b) hard cartilage, and (c) soft cartilage of the rostrum, bottom row represents the components of the bio-inspired models

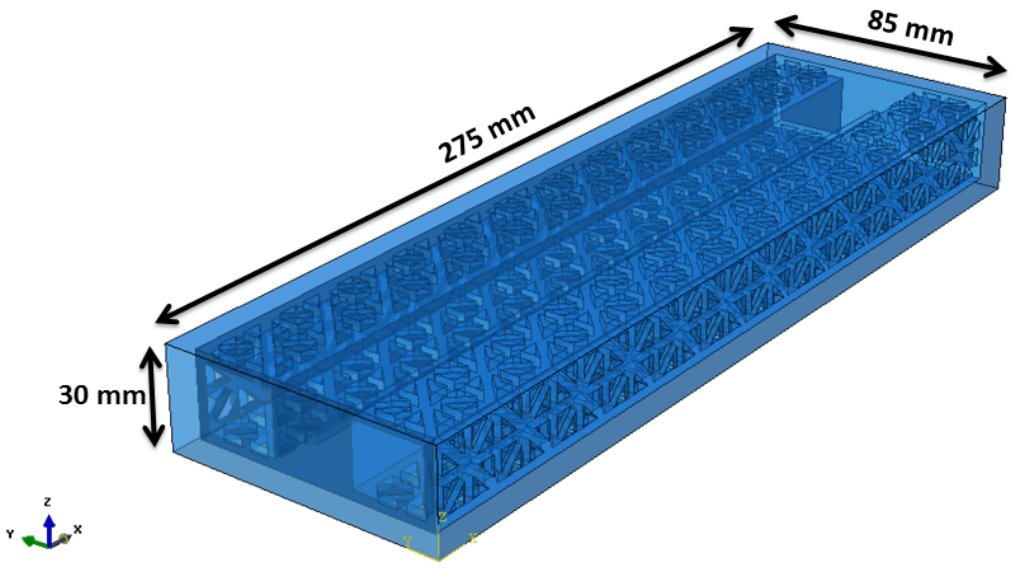

Figure 4.28

Dimensions of the bio-inspired structural systems

4.2.2 Force and displacement boundary conditions

Figure 4.29 displays the uniform pressure loading (50 MPa) applied to the upper surface of the models. A fixed-plate boundary condition is applied by restraining the displacements along the edges as shown in Figure 4.29.

4.2.3 Finite element experiment details

A general static analysis is conducted on the bio-inspired models using Abaqus/Standard [123]. The uniform pressure load is incrementally applied after the initialization starting at zero and increasing linearly to the maximum specified magnitude. Geometric non-linearity was taken into account. Owing to the complexity of the geometry coupled with the non-

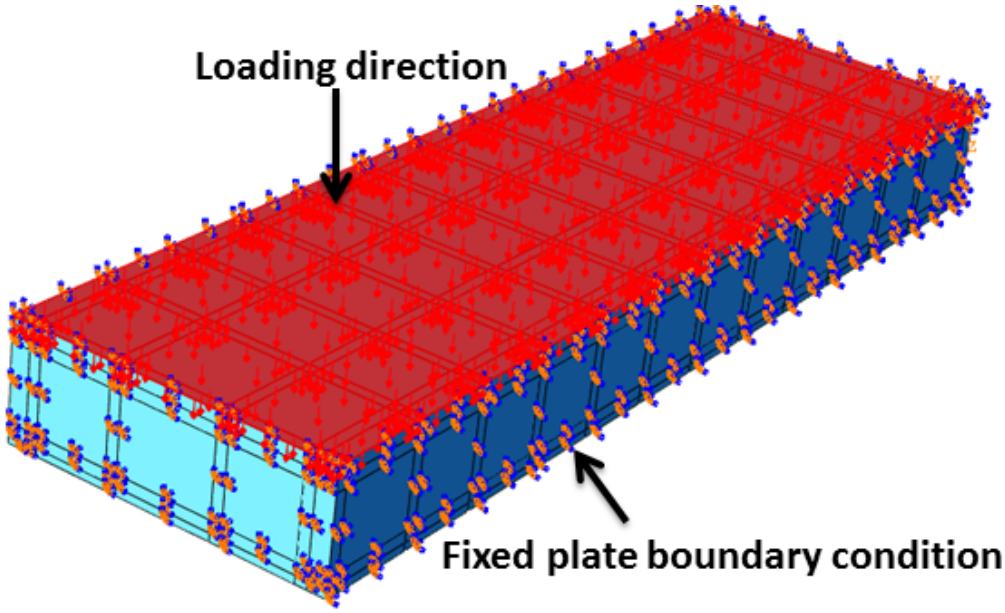

Figure 4.29

Uniform pressure loading on bio-inspired models with fixed-plate boundary condition

linear analysis, each simulation was executed on ERDC's High Performance Computing facilities located in Vicksburg, MS.

4.2.4 Contours of stress and deformation

Contours of stress and deformation are plotted to identify the areas of interest in the model. Figure 4.30(a) shows the maximum principal stresses and Figure 4.30(b) shows the deformations experienced by the crisscross patterned structural system (Figure 4.26(g)). The horizontal axis selected for further analysis passes through the center region (maximum deformation is observed in the center region) as well as the lattice structures of the models. The axis is selected in this manner to provide insight on the effects of the lattice

pattern on the structural response. For the sake of consistency, the same horizontal axis is used for each model investigated in the current study.

4.2.5 Deformation versus distance along the horizontal axis of the bio-inspired models

Figure 4.32 shows the deformation experienced by the five models as a function of true distance along the horizontal axis of the models displayed in Figure 4.30. As seen in Figure 4.32, the structure with the open box lattice (Figure 4.26(e)) pattern experiences the largest deformation. The cross box and square box experience a similar trend in displacement along the region of x=5 mm to x=15 mm. Around the center region, the model with the square box pattern experiences slightly higher deformation as compared to the model with the cross box pattern. In the region x=60 mm to x= 75 mm, the models with the square box and cross box patterns display a similar trend. The model with the crisscross box pattern experiences lower displacements as compared to the models with the open box, cross box, and square box patterns. As anticipated, the solid plate model experiences the least deformation out of the five models evaluated in the current study. Using the solid plate as the reference, the open box model shows an increase of approximately 35% in deformation, the square box model shows an increase of approximately 23% in deformation, the cross box model shows an increase of approximately 18% in deformation, and the crisscross box model shows an increase of approximately 13% in deformation. Table 4.4 summarizes these observations. Increasing the complexity of the lattice pattern significantly decreases the deformation experienced by the center region of the bio-inspired models as seen in Figure 4.32; however, increasing the complexity of the structure also increases its weight.

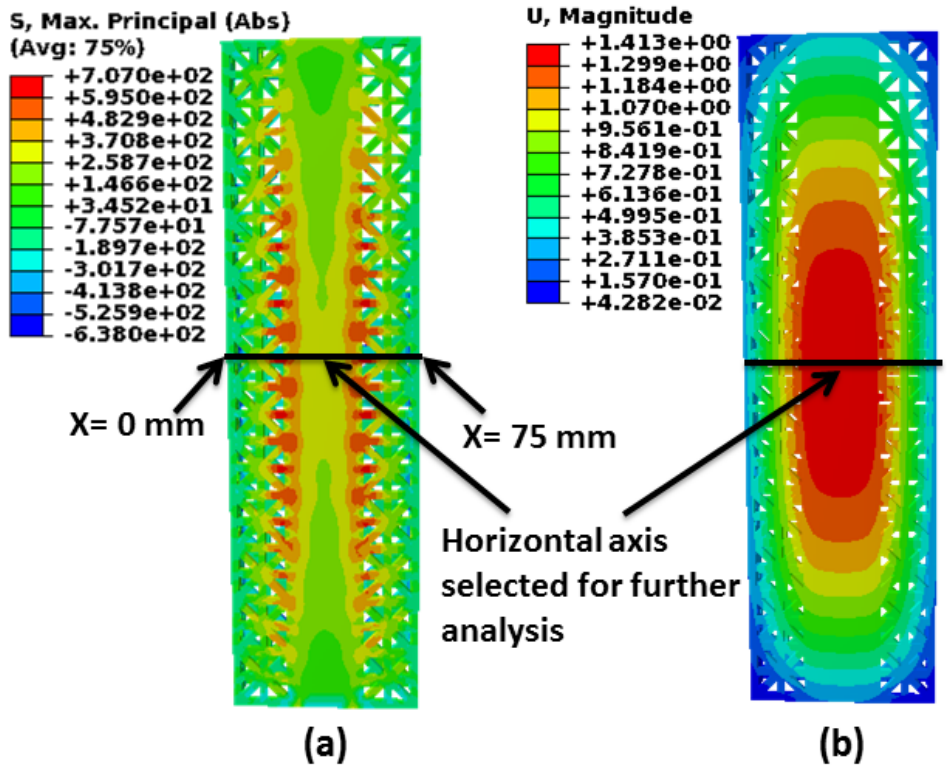

Figure 4.30

(a) Maximum principal stress (MPa) (b) Magnitude of displacement (mm)

The performance of the five bio-inspired models is analyzed in terms of maximum deformation and mass. Table 4.3 displays the maximum deformation and mass of the five models. The mass of the models includes the mass of the lattice structure and the mass of the central region. Figure 4.31 shows the decrease in deformation and increase in mass as the geometrical complexity of the models increases. The percentage decrease in deformation and percentage increase in mass with increasing geometrical complexity is shown in Table 4.4.

Table 4.3

Maximum deformation and mass of the bio-inspired models.

Lattice Pattern	Maximum deformation (mm)	Mass (Metric Tons)
Open box	1.51600	0.183331
Square box	1.38369	0.204356
Cross box	1.36397	0.212019
Crisscross box	1.29972	0.227944
Solid plate	1.26624	0.255615

4.2.6 Maximum principal stress versus distance along the horizontal axis of the bio-inspired models

Figure 4.33 displays the maximum principal stress for the five structural systems in the current study. In the center region, i.e., x=30 mm to x=45 mm, the five structural systems display a similar stress trend. However, at x=5 mm and x=69 mm, the square box pattern experiences higher stress as compared to all other models in the study. The open box pattern shows the second highest stresses at these locations. The models with the cross

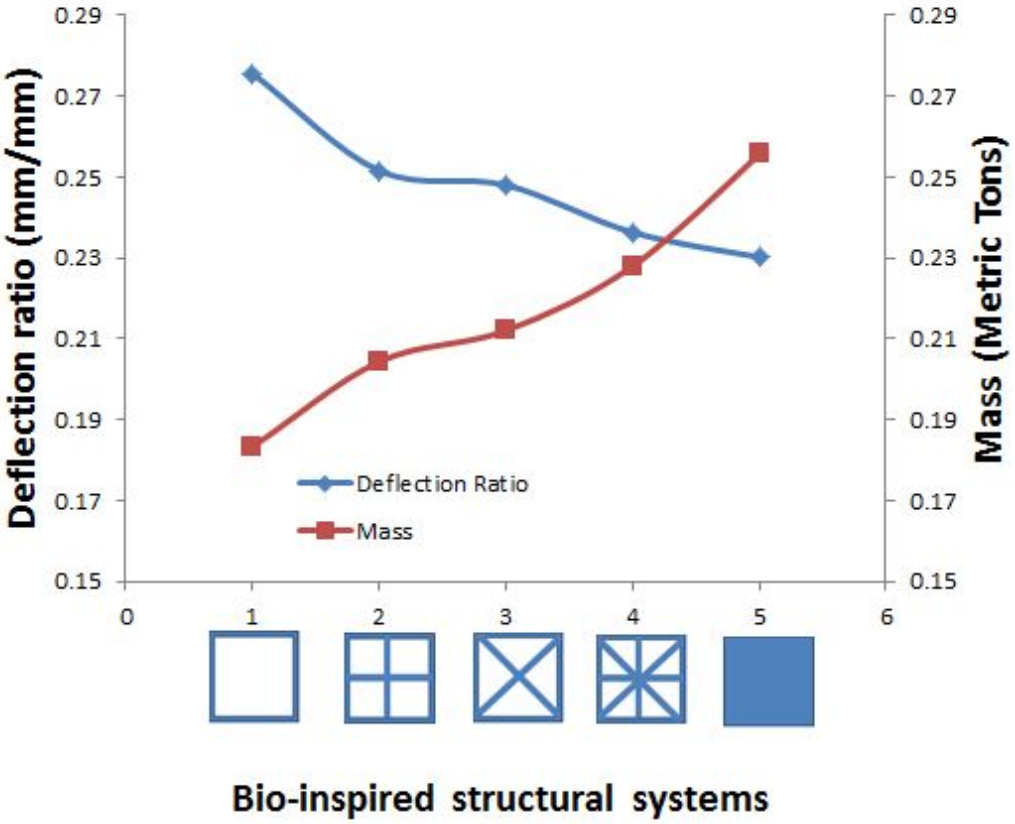

Figure 4.31

Deformation and mass of bio-inspired models.

Table 4.4

Percentage decrease in deformation and percentage increase in mass with increasing geometrical complexity.

Increasing geometrical complexity	Percentage decrease in deformation	Percentage increase in mass
Open box to square box	8.727573	11.4683
Square box to cross box	1.425175	3.74983
Cross box to crisscross box	4.710514	7.51112
Crisscross box to solid plate	2.575939	12.1394

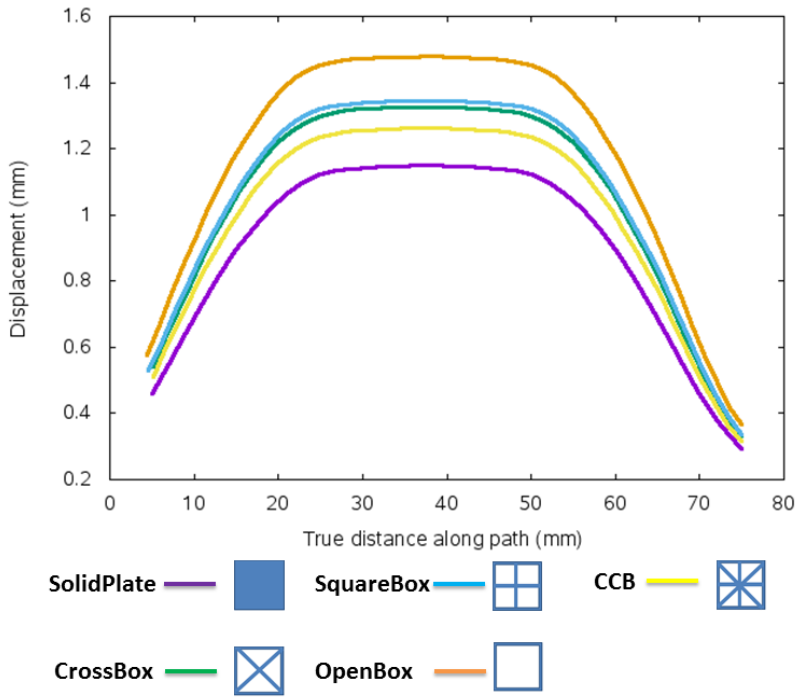

Figure 4.32

Deformation as a function of distance along the horizontal axis of bio-inspired models

box, the crisscross box, and solid plate patterns show similar trends at these locations. The model with the solid plate pattern displays stress peaks at x=25 mm and at x=50 mm that do not appear in the other models at those locations. The lattice acts as a load bearing member thereby providing stability to the center region. The stress in the center region is independent of the complexity of the lattice pattern for the fixed-plate boundary condition coupled with a uniformly distributed load.

4.2.7 Stress contours of the bio-inspired models

Figure 4.34 shows the maximum principal stress experienced by the lattices of the five bio-inspired models investigated in the current study. Stress peaks are seen in the region where the lattice pattern is attached to the center region for all of the models, i.e., a change in geometry. As seen in Figure 4.34 (d), the crisscross lattice structure shows the lowest peak stress value of $6.290e^{+02}$ MPa. Increasing the complexity of the lattice pattern resulted in a decrease in the peak stress as seen in Figure 4.34. Also, the crisscross box lattice pattern shows fewer stress peaks as compared to the four other patterns in the current study. This is because of the quad directional stability provided by this lattice pattern. The diagonal elements in the crisscross box lattice pattern reduce the stress without adding significant mass.

While the results in terms of deformations shown in Figure 4.32 are inconclusive, the stress results demonstrate that there is a significant decrease in stress for only a minimal increase in area. The addition of diagonal elements decrease the maximum stress by almost 50 %. Hence, as seen in Figure 4.34, the crisscross box pattern provides fewer stress

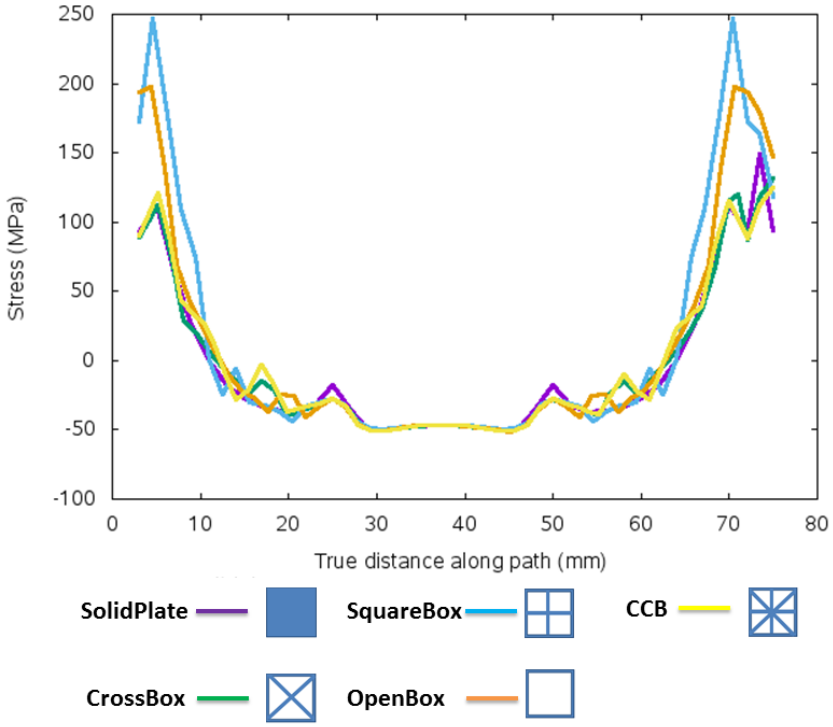

Figure 4.33

Maximum principal stress as a function of distance along the horizontal axis of bio-inspired models

peaks because of the quad directional stability provided by its members. Fewer stress peak implies greater resiliency. This proves the hypothesis – that increasing the geometrical complexity results in greater resiliency – true.

4.3 Application of scaling laws to bio-inspired structural systems

One of five bio-inspired structural systems described in Section 4.2.1 was selected for applying the scaling laws developed for a blast load in Appendix A. In the current study, similitude is used to scale the results from a small-scale computational prototype to a larger-scale model. The procedure to develop a set of scaling parameters using the Buckingham *Pi* theorem is explained in detail in Appendix A.

As illustrated in Appendix A, the Buckingham *Pi* theorem can be used to derive a set of non-dimensional *Pi* terms for a structure subjected to a blast load. The deformation d experienced by a structure impacted by blast loading is dependent on the linear dimension L, stress or pressure σ, density ρ, energy e, velocity v, mass m, force f, and time t. The number of parameters $n = 9$, the number of fundamental dimensions $k = 3$. Hence, there will be $(n - k) = 6$ non-dimensional pi terms. (L, σ, v) are picked as repeating variables that will be used to non-dimensionalize the others. Based on the procedure discussed in Appendix A, the non-dimensional *Pi* terms are as follows:

$$\frac{d}{L} = f(\frac{\sigma}{\rho v^2}, \frac{e}{\rho v^2 L^3}, \frac{m}{L^3 \rho}, \frac{f}{L^2 v^2 \rho}, \frac{tv}{L}) \tag{4.1}$$

Assuming that the strain rate is constant, Table 4.5 shows how to scale selected variables using the repeating variables (L, σ, v) listed above.

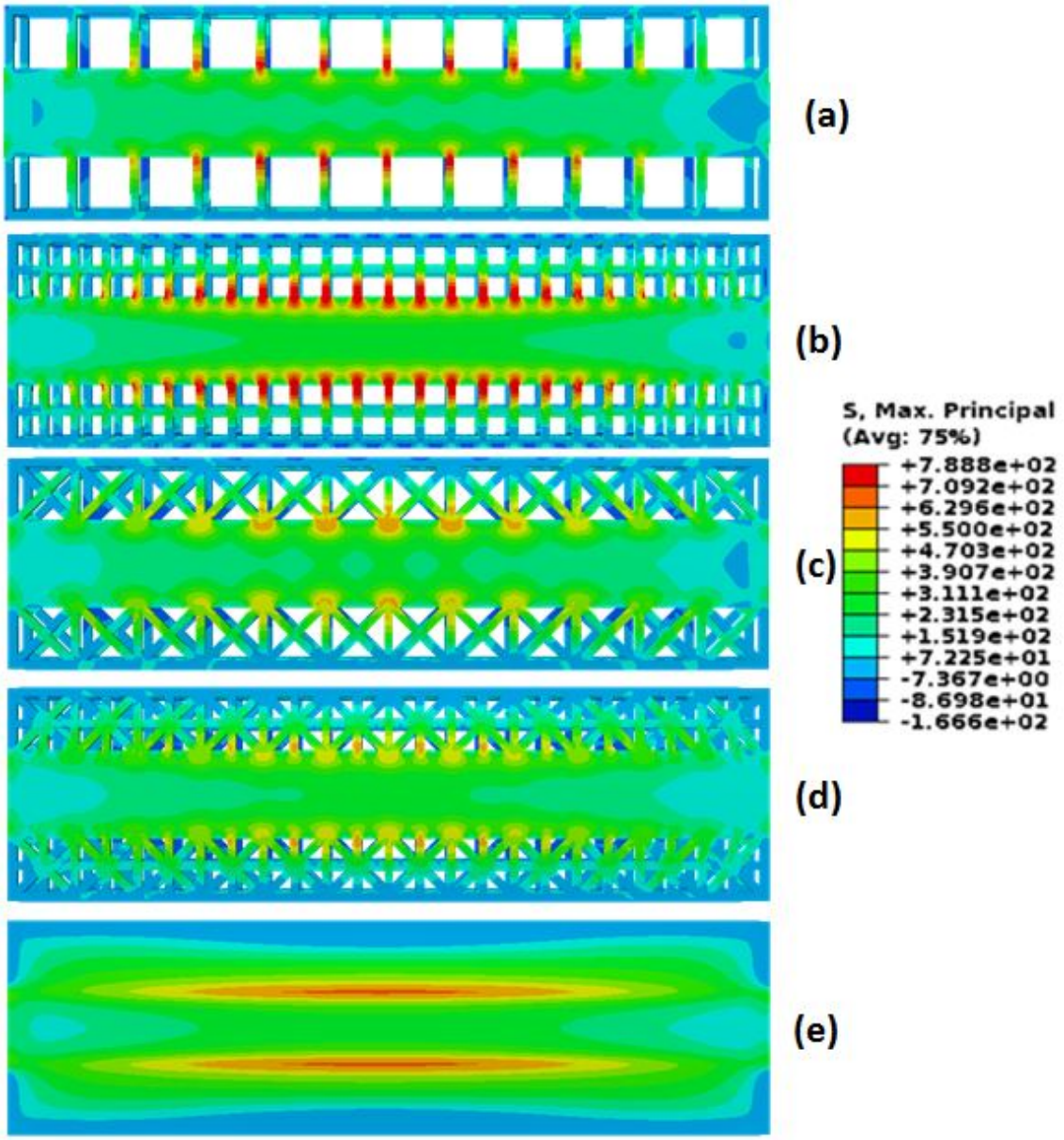

Figure 4.34

Maximum principal stress for the bio-inspired models. (a) open box, (b) square box, (c) cross box, (d) crisscross box, and (e)solid plate

Table 4.5

Relationship between the model and prototype for the variables used for blast load.

Parameters	Scale Factor	Scale =1	Scale=2	Scale=4
Length (L)	α	1	2	4
Mass (M)	α^3	1	8	64
Stress (α)	1	1	1	1
Time (t)	α	1	2	4
Velocity (V)	1	1	1	1
Displacement (U)	α	1	2	4
Strain (ϵ)	1	1	1	1
Acceleration (A)	$\frac{1}{\alpha}$	1	0.5	0.25

4.3.1 Model details

The bio-inspired model with a square box lattice pattern was selected for application of the scaling laws. The three component parts of the model are shown in Figure 4.35. The model comprises of 223,212 nodes, and 208,152 linear hexahedral elements. The dimensions of the model are shown in Figure 4.36. The Abaqus/Explicit solver was used to conduct the dynamic analysis. The point charge was placed 1000 mm away from the center region. Numerical experiments were carried to study the effect of blast loadings on the model. In the two cases considered, the model was scaled two and four times its initial size. The components of the bio-inspired model are represented by the same commercial materials selected for the rostrum. The details of the materials are provided in Section 4.1.2. Table 4.6 shows the details of the trinitrotoluene (TNT) weights and time durations of the numerical experiments performed in the current study. Displacement boundary conditions on the edges of the model are fixed for all degrees of motion. Fixed

boundary conditions were chosen for the edges to hold the model in a stationary position when it is under the influence of the blast load.

Table 4.6

Numerical experiment details (square box).

Scale	Length of model (mm)	Weight of TNT (kg)	Time duration (Sec)	Distance between model and TNT (mm)
1	275	0.02	0.025	1000
2	550	0.16	0.05	2000
4	1100	1.28	0.1	4000

4.3.2 Displacement contours of the bio-inspired structural system

Figure 4.37 shows the non-dimensionalized deformation for the model and the prototype of the bio-inspired model with the square box lattice pattern. Using the *Pi* terms from equation 4.1, the non-dimensional deformation is plotted. As seen from Figure 4.37, the non-dimensional deformation shows identical trends for the prototype and the scaled model. Since the model has a fixed-plate boundary condition around all of the edges, the center of the model experiences maximum deformation as expected. Figure 4.38 shows the non-dimensional deformation on the top surface of the hard cartilage component of the bio-inspired model. As expected, the maximum deformation is observed at the center of the mode, which is consistent with the location of the charge. The deformation steadily decreases near the edges of the hard cartilage. An identical deformation trend is seen for the prototype and the scaled models. Thus, the numerical simulation has achieved

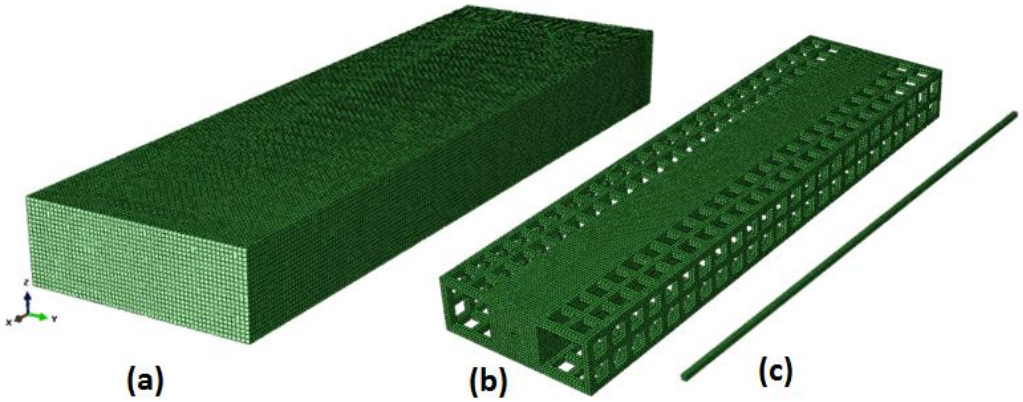

Figure 4.35

Bio-inspired model details (Square Box) (a) outermost tissue, (b) inner hard cartilage, and (c) innermost soft cartilage.

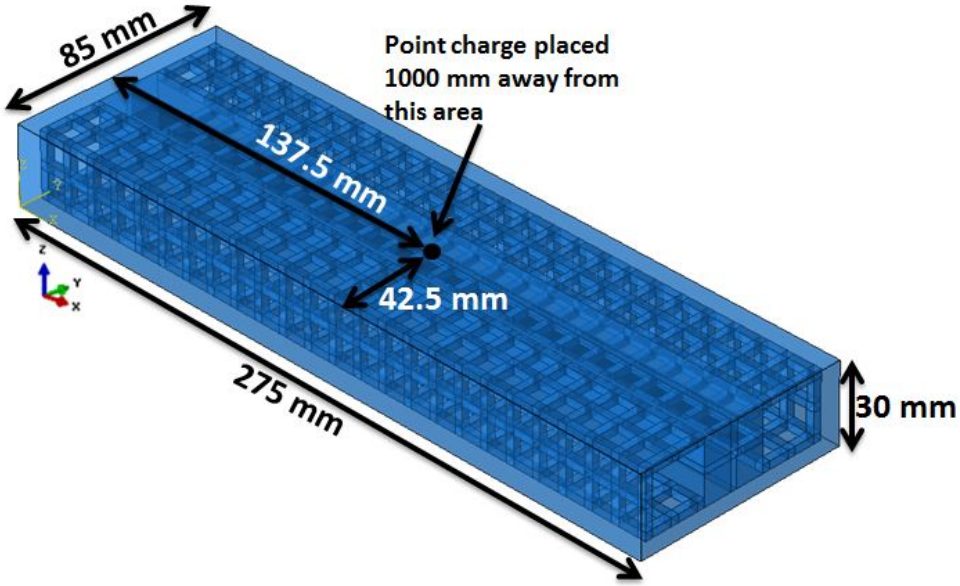

Figure 4.36

Dimension of the bio-inspired model (square box).

the expected values as reflected by the Buckingham *Pi* theorem. This shows that correct parameters were selected for the non-dimensional Pi terms.

4.3.3 Maximum principal stress contours of the bio-inspired structural system

Based on the similitude relations used for the current analysis, the stress should be the same for the scaled models. Figure 4.39 displays the maximum principal stress on the top surface of the bio-inspired prototype and the models.

Identical values of stresses are seen for the scaled models as seen in Figure 4.39. In each case, the stresses are higher at the center of the top surface and gradually diffuse throughout the surface. Figure 4.40 displays the stresses on the top surface of the hard cartilage of the bio-inspired prototype and scaled models. Stresses show a peak value in the region when the geometry of the system is changing, i.e., where the lattice structure is attached to the center region. This behaviour is observed in the prototype and the scaled models. The stress pattern, as well as the values follow, the laws of similitude for the prototype and the both scaled cases. This proves that correct parameters were selected for the derivation of the non-dimensional Pi terms for this problem.

4.4 Summary

The results of the proposed transdisciplinary research approach are now summarized:

1. This work has successfully identified stress flow patterns in a large, complex dataset generated from high performance computational mechanics experiments of bio-structure. The transdisciplinary approach used in the current work reduces the computational time, and cost, and increases the efficiency of the design-test-biuld cycle for rapid prototyping of novel bio-inspired structures.
2. This work has successfully formulated a complex bio-structure as a network flow problem to identify the stress flow patterns in the nascent stages of loading when

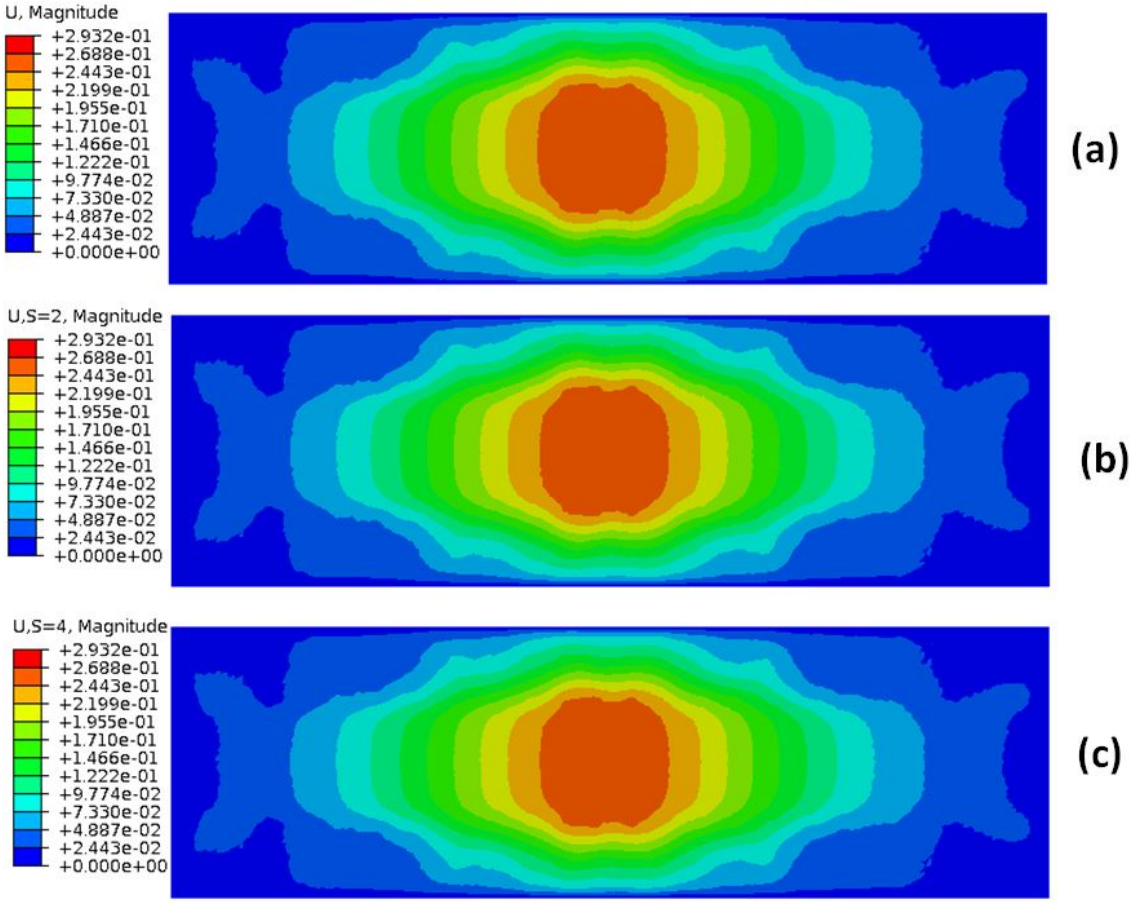

Figure 4.37

Non-dimensional deformation contours on top surface of bio-inspired model (square box). (a) prototype, (b) model scale factor = 2, (c) model scale factor = 4.

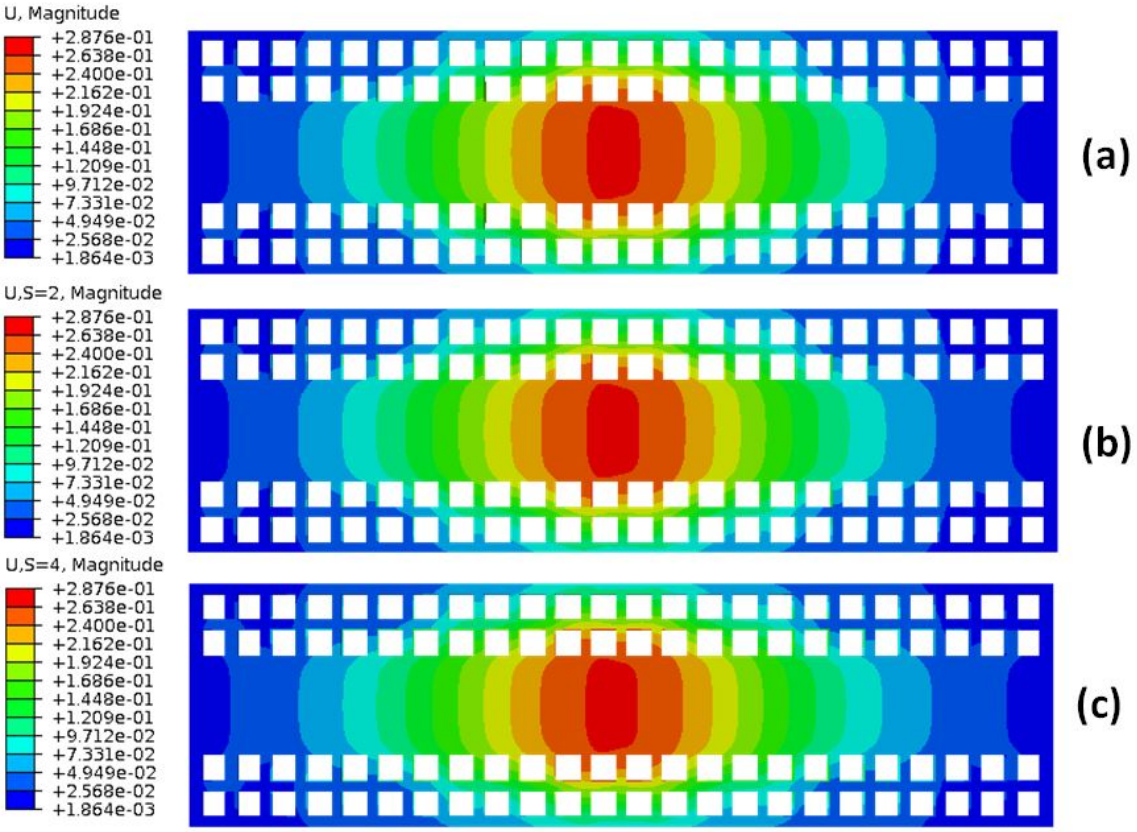

Figure 4.38

Non-dimensional deformation contours of hard cartilage bio-inspired model (square box).(a) prototype, (b) model scale factor = 2, (c) model scale factor = 4.

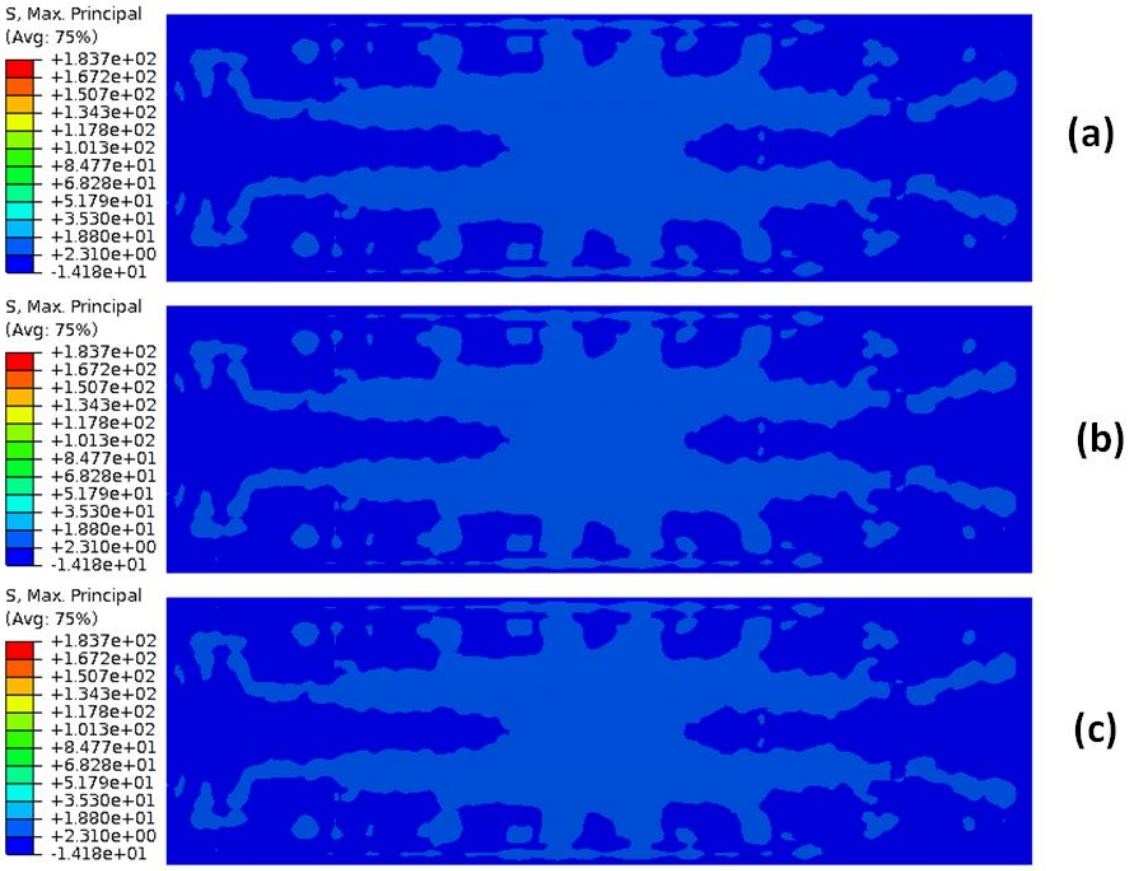

Figure 4.39

Stress contours of tissue part of bio-inspired model (square box). (a) prototype, (b) model scale factor = 2, (c) model scale factor = 4.

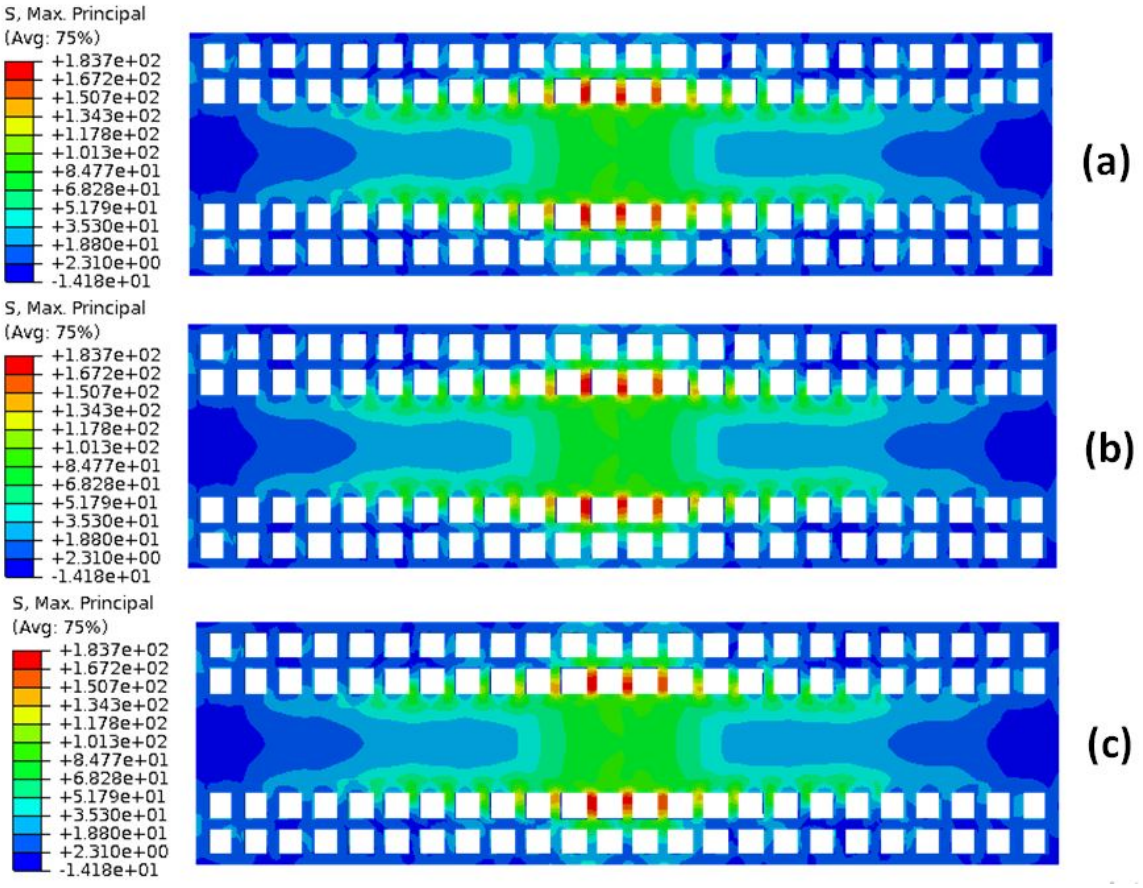

Figure 4.40

Stress contours of hard cartilage bio-inspired model (square box). (a) prototype, (b) model scale factor = 2, (c) model scale factor = 4.

the material is still in the linearly elastic region of the stress-strain curve. The flow network approach reduces the size of the problem since we are concentrating on the parameter of interest, i.e., stress. Also, since the stress flow patterns are captured in the linearly elastic regime, a full non-linear finite element analysis is not required. This will reduce the cost and computational time required for the analysis.

3. The flow network strategy was able to identify strain localization in the tensile regions, and crushing behavior in the compressive regions of the rostrum. Additionally, the flow network approach identified the failure sites to be at the locations where the material properties and geometry of components of the rostrum changes , i.e., at the interface regions. Also, the network flow approach captured the intrinsic structural response to an external load. The new flow network methodology is not sensitive to boundary conditions.

4. The source and sink nodes were identified from the stress and deformation contours obtained from the computational mechanics experiments on the rostrum. However, the flow network analysis is not sensitive to the locations selected for these special nodes.

5. Five proof-of-concept, bio-inspired, energy dissisipative structural systems with varying lattice patterns were developed to validate one of the research hypothesis. The maximum principal stress versus distance plots show that, the maximum principal stress decreases by almost 50 % by adding the diagonal element. The stress contours of the five bio-inspired models show that the crisscross box pattern provides fewer as well as lower stress peaks because of quad directional stability in the members. This proves the hypothesis - that increasing the geometrical complexity results in greater resiliency - true. The lattice architecture and the combination of three materials provides structural stability to the center region producing a low value for the maximum principal stress in the center region.

6. Deformation caused by blast impact on a bio-inspired model was represented in terms of dimensionless *Pi* terms by application of the Buckingham *Pi* theorem. Numerical experiments were carried out on the bio-inspired model to demonstrate the application of similitude laws for blast loading. The deformation and stress contours for the prototype and scaled models display that correct parameters were selected. These parameters can be used to scale the prototype to full scale model dimensions.

CHAPTER V

CONCLUSION

Biostructures in general exhibit superior characteristics because they have evolved to serve multiple and specific functions. This research seeks to identify and understand the phenomena of failure mechanisms in a complex bio-structure, i.e., the rostrum of the paddlefish. The novel transdisciplinary approach presented in this study is a means to identify the stress flow patterns in the nascent stages of loading through efficient application of the maximum-flow/minimum-cut algorithm. The novel approach presented in this study lays the foundation for understanding the influence of local topology on the global structural response.

5.1 Stress distribution patterns in the rostrum

In this study, the maximum flow optimization problem and the maximum-flow/minimum-cut pathways for a general flow network that was formulated from the node and connectivity information of the rostrum under a uniform pressure loading and blast loading condition were considered. The objective was to examine the stress distribution in the flow network that was weighted based on the stresses experienced by the structural system. The lattice of the rostrum is an indeterminate, non-linear structure with varying material types, and material properties, with non-uniform stiffness and irregularly-shaped members. The

maximum-flow /minimum-cut approach facilitated in the analysis of the indeterminate lattice architecture. The flow network approach developed in the current study was verified using two classical problems. The flow network approach was able to identify failure for the problem involving three-point bending of a simply-supported concrete beam. The developed approach was able to identify the shear and flexure patterns for four-point bending of a simply-supported concrete beam. The shear and flexure patterns indentified by the flow network approach govern the failure mechanism in this classical problem. Failure patterns were identified at the onset of loading when the material was still in the linearly elastic regime. By using the flow network strategy, the size of the problem is reduced since we are concentrating on a parameter of interest, i.e., stress in the current study. Also, since failure patterns are identified in the linearly elastic regime, the finite element element analysis does not have to be run until the structure fails thereby reducing the computational cost and the use of damage models in the analysis.

When applied to the model of the rostrum, the flow network strategy was able to identify strain localization in the tensile regions, and crushing behavior in the compressive regions of the rostrum. Additionally, the flow network approach identified the failure sites as the locations where the material properties, as well as the geometry, of component parts of the rostrum change, i.e., at the interfaces between different components of the rostrum. The guidance regarding the selection of the source and sink nodes was obtained from the stress and deformation contours obtained from the computational mechanics experiments. However, it was also demonstrated that the results were not sensitive to the location of the source and sink nodes, provided those locations are ”sensible.” Also, the flow network

analysis was not sensitive to the boundary conditions. The flow network approach captured the instrinsic response of the structural system to an external loading condition.

5.2 Runtime and speedup of the methodology used in the current research

This study has demonstrated novel software developed to process large datasets produced by high performance computational mechanics experiments on complex biostructures. The software developed for the current research was implemented on the rostrum of a paddlefish subjected to a uniform loading. The model for the computational mechanics experiments was developed in a Windows environment because of restrictions imposed by the finite element software. Owing to the complexity of the biostructure, the computational mechanics experiments were performed in parallel on a Linux cluster. The software developed for analyzing the stress distribution pattern is sufficiently robust to handle any structural system comprising variable constituent parts, parallelized to handle large datasets, and platform independent to deal with datasets generated across multiple platforms.

5.3 Performance analysis of bio-inspired structural systems

This work has developed five proof-of-concept, bio-inspired energy dissipative system with varying lattice patterns. The lattice architecture and the heterogenous materials provide structural stability to the center region. Five different bio-inspired models of different complexity were considered: square box, cross box, open box, solid plate, and crisscross box. Although the deflection versus distance plots are inconclusive, the maximum principal stress versus distance plots show that, the maximum principal stress decreases by almost 50 % by increasing the complexity of the structure by adding a diagonal element.

The stress contours show that the crisscross box pattern provides fewer and lower stress peaks because of the added quad directional stability in the members. This proves the hypothesis- that increasing the geometrical complexity results in greater resiliency-true.

5.4 Dimensional analysis of structural response of complex biostructure

This research has successfully conducted a series of numerical experiments on the rostrum of a paddlefish to apply similitude laws to predict the performance of complex, full-scale structural components subjected to blast loads. Similitude can be used to draw formal similarity in the behavior of models at different scales. The current research has demonstrated that structural deformation caused by blast can be represented in terms of dimensionless *Pi* terms by application of the Buckingham *Pi* theorem. This study has presented the development of similitude relationship for a simple system where the solution is known to verify the application of a similitude-based approach. Numerical experiments were carried out on the rostrum the of paddlefish to demonstrate the development and application of similitude laws for blast loading for complex structural models. From the analysis presented, it is evident that deformation, stress, velocity, and strains have been successfully scaled within a reasonably acceptable error range. This confirms that the correct parameters were selected for non-dimensionalization.

5.5 Future work

Based on the findings of the current study, the following recommendations are suggested for future work:

1. The flow patterns captured in nascent stages of loading were presented for three different boundary conditions. In these simulations, the material was still in the

linearly elastic regime. Future work will involve defining the magnitude of the load at which the failure mechanisms identified by network theory will occur, which will require the use of damage models as well as significantly longer run times for the finite element analysis.

2. The flow network approach used in the present work was verified using classical problems of three- and four-point bending of a simply-supported concrete beam. Future work will involve verification with physical experiments conducted on the rostrum.

3. The similitude laws derived in this research will be used to scale the geometrical and material properties of the 3D printed bio-inspired models. Physical experiments will be conducted for smaller scale models. These models will be scaled based on the material-geometry combination to full-scale structural systems.

REFERENCES

[1] C. A. Jennings and S. Zigler. Biology and life history of paddlefish in north america: An update. pages 1-22 in c. p. paukert and g. d. scholten (eds) paddlefish management, propagation, and conservation in the 21st century: Building from 20 years of research and management. bethesda, md: American fisheries society. Technical report, 2009.

[2] J. Hoover, E. Perkins, and P. Allison. Structural and material properties of the paddlefish rostrum. In *In proceedings to Technical Directors, Vicksburg, MS*. US Army Engineer Research and Development Center, February 2013.

[3] J. M. Gere and S. P. Timoshenko. *Mechanics of materials*. PWS Publishing Company, fourth edition edition, 1996.

[4] D. Sen. *A Parallel Execution Model for Prolog*. PhD thesis, Massachusetts Institute of Technology, Cambridge, Massachusetts, 2011.

[5] M Meyers, A Lin, Y Lin, E Olevsky, and S Georgalis. The cutting edge: Sharp biological materials. *Journal of the Minerals Metals and Materials Society*, 60(3):19–24, 2008.

[6] Sang-Hee Yoon and Sungmin Park. A mechanical analysis of woodpecker drumming and its application to shock-absorbing systems. In *Park 2011 Bioinspir. Biomim. 6 016003*. DOI: https://doi.org/10.1088/1748-3182/6/1/016003.

[7] G. A. Riveros, R. R. Patel, and J. J. Hoover. Swimming and energy dissipation enhancement induced by the rostrum of the paddlefish (polyodon spathula): A multiphysics, fluid-structure interaction analysis. *Materials Research Society Fall Meeting.*, 2015.

[8] J D Pettigrew and L Wilkens. Paddlefish and platypus: Parallel evolution of passive electroreception in a rostral bill organ. *Sensory Processing in Aquatic Environments*, pages 420–433, 2003.

[9] D.F. Williamson. Caviar and conservation status, management, and trade of north american sturgeon and paddlefish. *TRAFFIC North America, Washington, D. C.: World Wildlife Fund*, 2003.

[10] W. S. Tower. The passing of the sturgeon a case of the unparalleled, 1908.

[11] C. R. Stockard. Our new caviar fisheries. Century Magazine 76(Series 54), 1908.

[12] I. Saffron. *Caviar The strange history and uncertain future of the worlds most coveted delicacy*. Broadway Books, New York, 2002.

[13] U. s. geological survey. http://www.umesc.usgs.gov/aquatic/fish/paddlefish/risk.html.

[14] M. J. Buchler and Y. C. Yung. Deformation and failure of protein materials in physiologically extreme conditions and disease. *Nat Mater*, 8(3):175–188, 2009.

[15] M. J. Buchler. Tu(r)ning weakness to strength. *Nano Today*, 5(5):379–383, 2010.

[16] F. A. Forbes. The food of illinois fishes. *Bull III. State Lab. Nat. Hist.*, 1:71–89, 1878.

[17] F. A. Forbes. Studies of the food of freshwater fishes. *Ibid.*, 2:433–473, 1888.

[18] F. A. Forbes. On the food relations of freshwater fishes: A summary and discussion. *Ibid.*, 2:475–538, 1888.

[19] D. S. Jordan and B. W. Evermann. The fishes of north and middle america. *Bull. US Natl. Mus.*, 47:1–1240, 1896.

[20] C. R. Stockard. Observations on the natural history of polyodon spathula. *Amer. Nat.*, 41:753–766, 1907.

[21] M. Alexander. The paddle-fish (polyodon spathula). *Trans. Amer. Fish. Soc.*, 44:73–78, 1914.

[22] H. W. Norris. On function of the paddle of the paddlefish. *Proc. Iowa Acad. Sci.*, 30:135–137, 1923.

[23] H. Beach. The paddlefish, polyodon spathula. *Bull. Wis. Nat. Hist. Soc.*, 2:85–86, 1902.

[24] J. W. Sprague. Report of fisheries investigations during the sixth year of impoundment of fort randall reservoir, south dakota: South dakota dep. game fish parks dingell-johnson project f-i-r-8. Technical report, 1959.

[25] F. P. Meyer. *Life history of Marispometra Hastata and the biology of its host, Polyodon Spathula*. PhD thesis, Iowa State University, 1960.

[26] C. Gurgens, D. F. Russell, and L. A. Wilkens. Electrosensory avoidance of metal obstacles by the paddlefish. *Journal of Fish Biology*, 57:277–290, 2013.

[27] L. A. Wilkens, D. F. Russell, X. Pei, and C. Gurgens. The paddlefish rostrum functions as an electrosensory antenna in plankton feeding. *Proc. R. Soc. Lond*, 264:1723–1729, 1997.

[28] L. A. Wilkens and M. H. Hofmann. The paddlefish rostrum as an electrosensory organ: a novel adaptation for plankton feeding. *Bioscience*, 57:399–407, 2007.

[29] J. B. Allen and G. A. Riveros. Hydrodynamic characterization of the polyodon spathula rostrum using cfd. *Journal of applied mathematics*, 2013.

[30] U. G. Wegst, H. Bai, E. Saiz, A. P. Tomsia, and R. O. Ritchie. Bioinspired structural materials, Nat mater 2014.

[31] P. G. Dixon and L. J. Gibson. The structure and mechanics of moso bamboo material. *J R Soc Interface*, 11:20140321 2014.

[32] A. L. Gershon, H. A. Bruckand, S. Xu, M. A. Sutton, and V. Tiwari. Multiscale mechanical and structural characterizations of palmetto wood for bio-inspired hierarchically structured polymer composites. *Mater Sci Eng*, 30:235–244, 2010.

[33] A. V. Singh, A. Rahman, N. V. G. Sudhir Kumar, A. S. Aditi, M. Galluzzi, S. Bovio, S. Barozzi, E. Montani, and D. Parazzoli. Bio-inspired approaches to design smart fabrics. *Materials and Design*, 36:829–839, 2012.

[34] J. Gallant. The shape of the eiffel tower. *American Journal of Physics*, 70.2:160–162, 2002.

[35] M. K. Habibi, A. T. Samaei, B. Gheshlaghi, J. Lu, and Y. Lu. Asymmetric flexural behavior from bamboos functionally graded hierarchical structure: Underlying mechanisms. *Acta Biomaterialia*, 16:178–186, 2015.

[36] S. Bargmann, I. Scheider, T. Xiao, E. Yilmaz, G. A. Schneider, and N. Huber. Towards bio-inspired engineering materials: Modeling and simulation of the mechanical behavior of hierarchical bovine dental structure. *Computational Materials Science*, 79:390–401, 2013.

[37] L. F. Wang, J. H. Song, C. Ortiz, and M. C. Boyce. Anisotropic design of a multilayered biological exoskeleton. *J. Mater. Res.*, 24:3477–3494, 2009.

[38] L. F. Wang, J. H. Song, C. Ortiz, and M. C. Boyce. Enamel-a metallic-like deformable biocomposite. *Journal of Dentistry*, 35:431–427, 2007.

[39] L. Burns, A.P. Mouritz, D. Pook, and S. Feih. Bio-inspired hierarchical design of composite t-joints with improved structural properties. *Composites: Part B*, 69:222–231, 2015.

[40] C. Knipprath, I. Bond, and R. Trask. Biologically inspired crack delocalization in a high strain-rate environment. *J R Soc Interface*, 9(69):665–676, 2012.

[41] F. Barthelat, A. Dastjerdi, and R. Rabiei. An improved failure criterion for biological and engineered staggered composites. *J R Soc Interface*, 10(79), 2013.

[42] W. Cousins. Elastic modulus of lignin as related to moisture content. *Wood Sci Technol*, 10(1):9–17, 1976.

[43] E.A. Flores-Johnson, L. Shen, I. Guiamatsia, and G. D. Nguyen. A numerical study of bioinspired nacre-like composite plates under blast loading. *Composite Structures*, 126:329–336, 2015.

[44] J. E. Rim, P. Zavattieri, A. Juster, and H. D. Espinosa. Dimensional analysis and parametric studies for designing artificial nacre. *J Mech Behav Biomed Mater*, 4(2):190–211, 2011.

[45] K. Hideki and S. Taro. The toughening mechanism of nacre and structural materials inspired by nacre. *Sci Technol Adv Mater*, 12(6), 2011. 064710.

[46] P. Tran, T. D. Ngo, and P. Mendis. Bio-inspired composite structures subjected to underwater impulsive loading. *Comput Mater Sci*, 82:134–139, 2014.

[47] A. Schrijver. On the history of the transportation and maximum flow problems. *Mathematical Programming*, 91.3:437–445, 2002.

[48] S. Vitali, J. B. Glattfelder, and S. Battiston. The network of global corporate control. *PLoS ONE*, 6(10), 2011. e25995. doi:10.1371/journal.pone.0025995.

[49] A. Barrat, M. Barthelemy, R. Pastor-Satorras, and A. Vespignani. The architecture of complex weighted networks. *PNAS*, (101), 2004.

[50] E. Bullmore and O. Sporns. Complex brain networks: graph theoretical analysis of structural and functional systems. *Nature Reviews. Neuroscience*, 10:186–198, 2009.

[51] R. Dewil, P. Vansteenwegen, D. Cattrysse, and D. Van Oudheusden. A minimum cost network flow model for the maximum covering and patrol routing problem, european journal of operational research. *Nature Reviews. Neuroscience*, 247:27–36, 2015.

[52] B. B. Keskin, S. R. Li, D. Steil, and S. Spiller. Analysis of an integrated maximum covering and patrol routing problem. *Transportation Research PartE:Logistics and Transportation Review*, 1:215–232, 2012. doi:10.1016/j.tre.2011.07.005.

[53] J. Duran. *An Introduction to the Physics of Granular Materials*. Springer-Verlag, 2000.

[54] F. Radjai, D. E. Wolf, M. Jean, and J. J. Moreau. Bimodal character of stress transmission in granular packings. *Physical Review Letters*, 80:61–64, 1998.

[55] A. Tordesillas. Force chain buckling, unjamming transitions and shear banding in dense granular assemblies. *Philosophical Magazine*, 87:4987–5016, 2007.

[56] A. Tordesillas, D. M. Walker, G. Froyland, J. Zhang, and R.P. Behringer. Transition dynamics and magic-number-like behavior of frictional granular clusters. *Physical Review E*, 86, 2012. 011306.

[57] Q. Lin and A. Tordesillas. Towards an optimization theory for deforming dense granular materials: Minimum cost maximum flow solutions. *Journal of industrial and management optimization*, 10(1):337–362, 2014.

[58] X. Wei, P. Tran, A. Vaucorbeil, R. B. Ramaswamy, F. Latourte, and H. D. Espinosa. Three dimensional numerical modeling of composite panels subjected to underwater blast. *Journal of the Mechanics and Physics of Solids*, pages 1319–1336, June 2013.

[59] F. Latourte, D. Grgoire, D. Zenkert, X. Wei, and H. D. Espinosa. Failure mechanisms in composite panels subjected to underwater impulsive loads. *Journal of the Mechanics and Physics of Solids*, 59(8):1623–1646, August 2011.

[60] E.I. S. Flores and M.I. Friswell. Multi-scale finite element model for a new material inspired by the mechanics and structure of wood cell-walls. *Journal of the Mechanics and Physics of Solids*, 60(7):1296–1309, July 2012.

[61] F. J. Vernerey, K. Musiket, and F. Barthelat. Mechanics of fish skin: A computational approach for bio-inspired flexible composites. *International Journal of Solids and Structures*, 51:274–283, 2014.

[62] S. Mann. Biomineralization: Principles and concepts in bioinorganic materials chemistry. Oxford Univ. Press, 2001.

[63] N. Pugno. Spiderman gloves. *Nano Today*, 3(56):35–41, 2008.

[64] C. Menon and M. Sitti. A biomimetic climbing robot based on the gecko. *Journal of Bionic Engineering*, 3:115–125, 2006.

[65] K. Autumn, Y. Liang, T. Hsieh, W. Zesch, W. P. Chan, T. Kenny, R. Fearing, and R. J. Full. Adhesive force of a single gecko foor hair. *Nature*, 405:681–685, 2000.

[66] J. D. Logan. *Applied Mathematics*. Fourth edition.

[67] E. Buckingham. On physically similar systems: illustrations of the use of dimensional equations. *Phys Rev*, 4:345e76, 1914.

[68] A. Matuszak. Dimensional analysis can improve equations of the model. *Procedia Engineering*, 108:526–535, 2015.

[69] A. Carpinteri, P. Cornetti, and S. Puzzi. Scaling laws and multiscale approach in the mechanics of heterogeneous and disordered materials. *Applied Mechanics Reviews*, 59:283–305, 2006.

[70] J.D. Clayton. Penetration resistance of armor ceramics: Dimensional analysis and property correlations. *International Journal of Impact Engineering*, 85:124–131, 2015.

[71] Q. Zong, T. Zheng, H. Liu, and C. Li. Development of head loss equations for self- cleaning screen filters in drip irrigation systems using dimensional analysis. *Biosystems Engineering*, 133:116–127, 2015.

[72] M.E. Ephraim, O.T. Thom-Manue, and E.O. Rowland-Lato. Structural modeling of stability of plane sway frames. *Int. J.Civ. Eng. Reas.*, 2(4), 2012.

[73] Sh. Torkamani, H.M. Navazi, A.A. Jafari, and M. Bagheri. Structural similitude in free vibration of orthogonally stiffened cylindrical shells. *Thin-Walled Struct*, 47:1316–1330, 2009.

[74] S.J. Kline Springer. *Similitude and Approximation Theory*. 2011.

[75] M. Safoniuk, J.R. Grace, L. Hackman, and C.A. Mcknight. Use of dimensional similitude for scale-up of hydrodynamics in three -phase fluidised beds. *Chem. Eng. Sci.*, 54:4961–4966, 1999.

[76] C.S. Chouchaoui, P. Parks, and O.O. Ochoa. Similitude study for a laminated cylindrical tube under tension, torsion, bending, internal and external pressure. *Compos. Struct*, 44:231–236, 1999.

[77] A. Yazdi and J. Rezaeepazhand. Structural similitude for flutter of delaminated composite beam-plates. *Composite Structures*, 93:1918–1922, 2011.

[78] M. Ramu, V. P. Raja, and P. R. Thyla. Establishment of structural similitude for elastic models and validation of scaling laws. *KSCE Journal of Civil Engineering*, 17(1):139–144, 2013.

[79] G. J. Simitses and J. Rezaeepazhand. Structural similitude for laminated structures. *Compos Eng*, 3(7-8):751–765, 1993.

[80] G. J. Simitses and J. Rezaeepazhand. Structural similitude and scaling laws for cross-ply laminated plates. In *In: Proceedings of the American Society for Composites*, pages 265–274. Ohio Aerospace Institute Technomic Publishing Co. Inc, 1994.

[81] J. Rezaeepazhand, G. J. Simitses, and J. H. Starnes Jr. Design of scaled down models for stability of laminated plates. *AIAA J*, 33(3):515–519, 1995.

[82] G. J. Simitses, Starnes Jr JH, and J. Rezaeepazhand. Structural similitude and scaling laws for plates and shells: a review. In *In: Collection of Technical Papers-AIAA/ASME/ASCE/AHS/ASC Structures*, pages 393–403. Structural Dynamics and Materials Conference, 2000.

[83] V. Ungbhakorn and P. Singhatanadgid. Similitude invariants and scaling laws for buckling experiments on anti-symmetrically laminated plates subjected to biaxial loading. *Composite Structures*, 59:455–465, 2003.

[84] A. Farhidzadeha, A. C. Mpalaskasb, T. E. Matikasb, H. Farhidzadehc, and D. G. Aggelis. Fracture mode identification in cementitious materials using supervised pattern recognition of acoustic emission features. *Construction and Building Materials*, 67(Part B):129–138, September 2014.

[85] D.G. Aggelis. Classification of cracking mode in concrete by acoustic emission parameters. *Mech Res Commun*, 38:153–157, 2011.

[86] A. Farhidzadeh, S. Salamone, and P. Singla. A probabilistic approach for damage identification and crack classification in reinforced concrete structures. *J Intell Mater Syst Struct*, 2013.

[87] K. Kageyama, H. Murayama, I. Ohsawa, M. Kanai, K. Nagata, and Y. Machijima. Acoustic emission monitoring of a reinforced concrete structure by applying new fiber-optic sensors. *Smart Mater Struct*, 14:s52–s59, 2005.

[88] M. Ohtsu, M. Uchida, T. Okamoto, and S. Yuyama. Damage assessment of reinforced concrete beams qualified by acoustic emission. *ACI Struct J*, pages 411–417, 2002.

[89] T. Shiotani, D.G. Aggelis, and O. Makishima. Global monitoring of large concrete structures using acoustic emission and ultrasonic techniques: case study. *J Bridge Eng*, 14(3):188–192, 2009.

[90] A. Carpinteri, G. Lacidogna, G. Niccolini, and S. Puzzi. Critical defect size distributions in concrete structures detected by the acoustic emission technique. *Meccanica*, pages 349–363, 2008.

[91] G. L.G. Gonzles, J. A.O. Gonzlez, J. T.P. Castro, and J. L.F. Freirei. A j-integral approach using digital image correlation for evaluating stress intensity factors in fatigue cracks with closure effects. *Theoretical and Applied Fracture Mechanics*, 2017.

[92] M. A. Sutton, S. R. McNeill, J. D. Helm, and Y.J. Chao. Advances in two-dimensional and three dimensional computer vision. *Photomechanics, Springer*, pages 323–372, 2000.

[93] M.A. Sutton, J.J. Orteu, and H. Schreier. *Image Correlation for Shape, Motion and Deformation Measurements: Basic Concepts, Theory and Applications*. Springer Science, Business Media, 2009.

[94] J. Carroll, C. Efstathiou, J. Lambros, H. Sehitoglu, B. Hauber, S. Spottswood, and R. Chona. Investigation of fatigue crack closure using multiscale image correlation experiments. *Eng. Fract. Mech.*, 76:2384–2398, 2000.

[95] P. Lopez-Crespo, A. Shterenlikht, J. Yates, E. Patterson, and P. Withers. Some experimental observations on crack closure and crack-tip plasticity. *Fatigue Fract. Eng. Mater. Struct.*, 32:418–429, 2009.

[96] J. Vasco-Olmo, F. Daz, A. Garca-Collado, and R. Dorado-Vicente. Experimental evaluation of crack shielding during fatigue crack growth using digital image correlation. *Fatigue Fract. Eng. Mater. Struct.*, 38:223–237, 2015.

[97] M. Fazzini, S. Mistou, and M. Karama. Identification of elastomers by digital image correlation. *(Paris, France) 5th European Conference on Constitutive Modelsfor Rubber*, 2007.

[98] C.P. Goh, M.M. Ratnam, and H. Ismail. Large in-plane deformation mapping and determination of young's modulus of rubber using scanner-based digital image correlation. *Exp. Tech.*, 40(3):1117–1127, 2015.

[99] N. Bahlouli, S.M. Guil, S. Ahzi, and M. Laberge. Stress-strain response of biomaterials by a digital image correlation method: application to tecoflex. *J. Mater. Sci. Technol.*, 20(1):114–116, 2004.

[100] A. A. Mudassar and S. Butt. Improved digital image correlation method. *Opt. Lasers Eng.*, 87:156–167, 2016.

[101] M. Hallgren and M. Bjerke. Non-linear finite element analyses of punching shear failure of column footings. *Cement Concr Compos*, 24(6):491–6, 2002.

[102] N. F. Mamede, A. P. Ramos, and D. M. Faria. Experimental and parametric 3d nonlinear finite element analysis on punching of flat slabs with orthogonal reinforcement. *Eng Struct.*, 48:442–457, 2013.

[103] J. Shu, M. Plos, K. Zandi, M. Johansson, and F. Nilenius. Prediction of punching behavior of rc slabs using continuum non-linear fe analysis. *Eng Struct.*, 15(125):15–25, 2016.

[104] C. La Borderie, C. Lawrence, and A. Menou. Approche msoscopique du comportement du bton: apport de la reprsentation gomtrique. *Revue europenne de gnie civil*, 11(4):407–21, 2007.

[105] P. Grassl, P. D. Grgoire, L.B. Rojas-Solano, and G. Pijaudier-Cabot. Meso-scale modelling of the size effect on the fracture process zone of concrete. *Int J Solids Struct.*, 49(13):1818–1827, 2012.

[106] D. Grgoire, L. B. Verdon, Lefort V, P. Grassl, J. Saliba J, and J-P Regoin. Mesoscale analysis of failure in quasi-brittle materials: comparison between lattice model and acoustic emission data. *Int J Numer Anal Methods Geomech*, 2015. http://dx.doi.org/10.1002/nag.2363.

[107] A. Tordesillas, S. Pucilowski, D. M. Walker, J. F. Peters, and L. E. Walizer. Micromechanics of vortices in granular media: connection to shear bands and implications for continuum modelling of failure in geomaterials. *Int. J. Numer. Anal. Methods Geomech*, 38:1247–1252, 2014.

[108] V. Lefort, G. Pijaudier-Cabot, and D. Grgoire. Analysis by ripleys function of the correlations involved during failure in quasi-brittle materials: Experimental and numerical investigations at the mesoscale. *Engineering Fracture Mechanics*, 147:449–467, 2015.

[109] A. Tordesillas, D. M. Walker, E. And, and G Viggiani. Revisiting localized deformation in sand with complex systems. *Proc R Soc A*, 469, 2012. http://dx.doi.org/10.1098/rspa.2012.0606.

[110] J. F. Peters and L. E. Walizer. Patterned nonaffine motion in granular media. *J. Eng. Mech.*, 139(10):1479–1490, 2013. DOI:10.1061/(ASCE)EM.1943-7889.0000556.

[111] A. Tordesillas, S. T. Tobin, M. Cil, K. Alshibli, and R. P. Behringer. Network flow model of force transmission in unbonded and bonded granular media. *Phys. Rev. E*, 91(062204), 2015.

[112] D. M. Walker, A. Tordesillas, J. Ren, J. A. Dijksman, and R. P. Behringer. Uncovering temporal transitions and self-organization during slow aging of dense granular media in the absence of shear bands. *EPL (Europhysics Letters)*, 107(1). DOI: https://doi.org/10.1209/0295-5075/107/18005.

[113] D. P. Bertsekas. Network optimization: Continuous and discrete models. *(Optimization, Computation, and Control).*, 1998.

[114] Q. Lin and A. Tordesillas. Towards an optimization theory for deforming dense granular materials: Minimum cost maximum flow solutions. *J. Ind. Manag. Optim.*, 10:337, 2014.

[115] J. W. Rudnicki and J. R. Rice. Resolving structural modifications of colloidal glasses by combining x-ray scattering and rheology. *J. Mech. Phys. Solids*, 23:371, 1975.

[116] B. D. Ripley. Modelling spatial patterns. *J R Stat Soc Ser B (Meth)*, 39(2):172–212, 1977.

[117] R. P. Duncan. Flood disturbance and the coexistence of species in a lowland podocarp forest, south westland, new zealand. *Journal of Ecology*, 81(3):403–416, 1933. DOI: 10.2307/2261519.

[118] N. E. Stamp and J. R. Lucas. Spatial patterns and dispersal distances of explosively dispersing plants in florida sandhill vegetation. *Journal of Ecology*, 78(3):589–600, September 1990. DOI: 10.2307/2260886.

[119] P. J. Diggle and A. G. Chetwynd. Second-order analysis of spatial clustering for inhomogeneous populations. *Biometrics*, 47(3):1155–1163, September 1991. DOI: 10.2307/2532668.

[120] R. R. Patel and G. A. Riveros. Towards development of innovative bio-inspired materials by analyzing the hydrodynamic properties of polyodon spathula (paddlefish) rostrum. ERDC/ITL TR 13-4, Engineer Research and Development Center, 2013.

[121] J. Deang, M. Horstemeyer, L. Williams, E. Perkins, P. Allison, and G. Riveros. Paddlefish rostrum as a structure for bioinspiration: Analysis and modeling of the of the stress state and strain rate dependence behavior of cartilage. TMS Annual Meeting and Exhibition, 2016.

[122] P. G. Allison, J. F. Deang, A. J. Diaz, A. R. Poda, J. J. Hoover, M. F. Horstemeyer, and E. J. Perkins. Characterization of paddlefish (polyodon spathula) rostrum stellate bones. *Bioinspired, Biomimetic, and Nanobiomaterials*, 1(3):63–68, 2014.

[123] Dassault Systmes, Providence, RI, USA. *Abaqus 6.13 Analysis User's Guide. Online Documentation Help*, 2013.

[124] R. K. Ahuja, T. L. Magnanti, and J. B. Orlin. *Network flows theory, algorithms, and applications.* 1993.

[125] M. E. J. Newman. *Networks: An Introduction*. Oxford University Press, Oxford, 2010.

[126] J. R. Bondy and U. S. R. Murty. *Graph theory (Graduate texts in mathematics)*. Springer, New York, 2008.

[127] D. Jungnicke. *Graphs, networks and algorithms*. Springer, Berlin GE, third edition edition, 2008.

[128] G. A. Riveros and V. S. Gopalaratnam. Shear response of reinforced concrete deep beam: Validating fracture mechanics based numerical modelling with experiments. *ACI, SP-300 Fracture Mechanics Applications in Concrete*, 2015.

[129] G. A. Riveros and V. S. Gopalaratnam. Fracture response of reinforced concrete deep beams finite element investigation of strength and beam size. *Journal of Applied Mathematics*, 4(11), 2013.

[130] T. H. Cormen, C. E. Leiserson, and R. L. Rivest. Introduction to algorithms. The MIT electrical engineering and computer science series, 1990.

[131] http://dimacs.rutgers.edu/.

[132] Y. Boykov and V. Kolmogorov. An experimental comparison of min-cut/max-flow algorithms for energy minimization in vision. *IEEE Transactions on Pattern Analysis and Machine Intelligence (PAMI)*, 26(9):1124–1137, 2004.

[133] J. Ahrens, B. Geveci, and C. Law. Paraview: An end-user tool for large data visualization, visualization handbook. *Elsevier*, 2005.

[134] Abraham Silberschatz, Peter Baer Galvin, and Greg Gagne. Operating system concepts. Wiley.

[135] Vipin Kumar, Ananth Grama, Anshul Gupta, and George Karypis. Introduction to parallel computing. design and analysis algorithms. ISBN 0-8053-3170-0.

[136] W. C. Yound and R. G. Budynas. *Roark's formulas for stress and strain*. McGraw-Hill.

[137] R. R. Patel and G. A. Riveros. Towards development of innovative bio-inspired materials by analyzing the hydrodynamic properties of polodon spathula (paddlefish) rostrum. TR 13-4, ERDC/ITL, 2013.

APPENDIX A

DEVELOPMENT AND APPLICATION OF SIMILITUDE LAWS

The solution for a typical engineering problems is obtained through the application of analytical, computational and experimental methodologies. In many cases, due to cost or size constraints, it is not possible to test the full-scale article. Similitude is used in this scenario wherein the observations made in the laboratory can be used to estimate the behavior of a real-world system by establishing a relationship between the results of the scaled experiment and those observed in the real-world application. This section demonstrates the development and application of similitude laws for complex structural models subjected to blast loads.

Generally, similitude has been used to scale the parameters from a larger scale prototype to a smaller scale model. In the current study, similitude is used to scale results obtained from the small-scale computational prototype to a larger-scale model. The computational prototype in the current research is the rostrum of the paddlefish. In preliminary computational experiments, the rostrum exhibited better energy dissipation and load bearing capacity when compared to a homogenous material with a similar geometry. Accordingly, this section shows the procedure to develop a set of scaling parameters to scale the computational prototype to a larger size and to verify the similitude laws.

A.1 Example: Buckingham *Pi* theorem for uniform load on a fixed plate

As an example of application of the Buckingham Pi theorem, consider a rectangular plate with all edges fixed (as shown in Figure A.1) with a uniformly distributed load w over the entire plate. This case is chosen for analytic validation of similitude because of the resemblance of its boundary conditions to the boundary conditions used in the blast

analysis. The critical load P_{cr} of the plate is dependent on the distributed load w on the plate, Young's modulus E, the cross sectional moment of inertia I, the vertical deflection u, and the length of the beam l. P_{cr} can be written for this case as follows:

$$P_{cr} = g(w, E, I, u, l) \tag{A.1}$$

Application of the Buckingham *P*i theorem to a general problem can be described as follows. Consider a dimensional quantity *F* that represents a physical phenomenon and suppose that the dimensional quantities or factors influencing this phenomenon are $\delta_1, \delta_2, \delta_3, ...\delta_n$. The relation between *F* and the dimensional parameters $\delta_1, \delta_2, \delta_3, ...\delta_n$ is given by the following equation:

$$F = g(\delta_1, \delta_2, \delta_3, ...\delta_n) \tag{A.2}$$

In Equation A.2, *F* is the dependent variable and $\delta_n (n = 1, 2, 3, ...n)$ are the independent variables. Equation A.2 can be non-dimensionalized and expressed as shown in Equation A.3:

$$\pi_1 = f(\pi_2, \pi_3, \pi_4, ...\pi_{n-k}) \tag{A.3}$$

where $\pi_2, \pi_3, \pi_4, ...\pi_{n-k}$ are the dimensionless products of *n* physical parameters and *k* is the number of fundamental dimensions (Force, Length, Time) or (Mass, Length, Time) involved in the physical phenomenon.

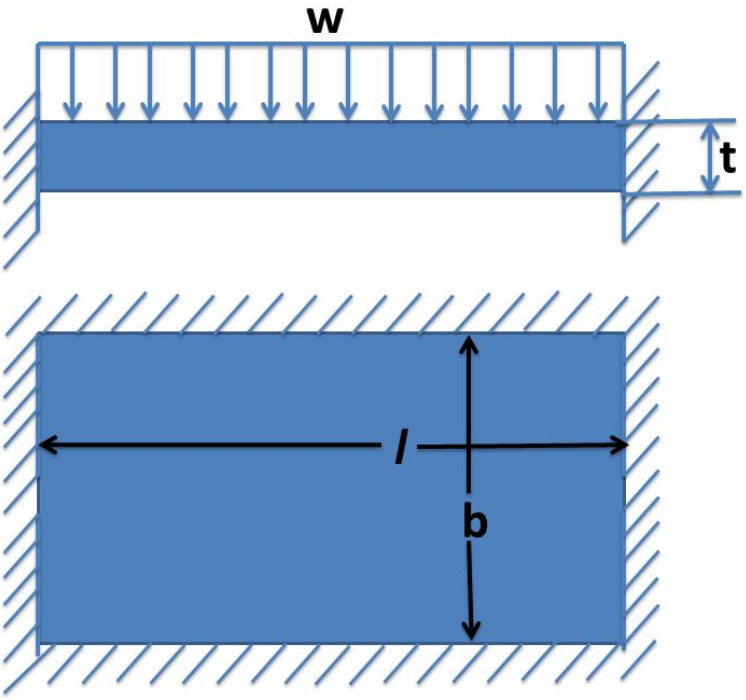

Figure A.1

Uniformly loaded plate with all edges fixed

The similitude requirement stipulates that the π terms $\pi_2, \pi_3, \pi_4, ...\pi_{n-k}$ must be equal for the model and the prototype if the functional relationship, (i.e., $(\pi_1)_m = (\pi_1)_p$), is to be satisfied.

In this example, the number of physical variables, $n = 6$, and the number of dimensions, $k = 2$. Therefore, there are *n-k* = 4 pi groups. The independent quantities namely $P_{cr}, w, E, I, b, t,$ and u need to be represented in terms of non-dimensional pi products as indicated by Equation A.3 . The repeating variables are selected in such a way that all the relevant dimensions are represented within them. For this example *(E, l)* are selected as repeating variables that will be used to non-dimensionalize the remaining quantities.

$$P_{cr} = g(w, E, I, u, l) \tag{A.4}$$

$\pi_1 = P_{cr} E^a l^b$

$\pi_1 = F(\frac{F}{L^2}^a) L^b$

$a = 1; b = -2$

$$\pi_1 = \frac{P_{cr}}{EL^2} \tag{A.5}$$

$\pi_2 = W E^a l^b$

$\pi_2 = \frac{F}{L^2}(\frac{F}{L^2})^a L^b$

$a = -1; b = 0$

$$\pi_2 = \frac{W}{E} \tag{A.6}$$

$\pi_3 = IE^a l^b$

$\pi_3 = L^4(\frac{F}{L^2})^a L^b$

$a = 0; b = -4$

$$\pi_3 = \frac{I}{l^4} \tag{A.7}$$

$\pi_4 = uE^a l^b$

$\pi_4 = L(\frac{F}{L^2})^a L^b$

$a = 0; b = -1$

$$\pi_4 = \frac{u}{l} \tag{A.8}$$

The pi products represented by Equations A.5 through A.8 are dimensionless. Based on this analysis, the prediction equation given by Equation A.3 is:

$$\pi_1 = f(\pi_2, \pi_3, \pi_4) \tag{A.9}$$

Hence,

$$\frac{P_{cr}}{El^2} = f(\frac{W}{E}, \frac{I}{l^4}, \frac{u}{l}) \tag{A.10}$$

The quantities affecting the physical phenomenon under study are represented in Equation A.10 in terms of the dimensionless pi products. The functional relationship will be

satisfied, (i.e., $(\pi_1)_{model} = (\pi_1)_{prototype}$), if the three non-dimensional parameters π_2, π_3, π_4 are equal for the model and the prototype.

Equation A.10 is a generalized equation and can be used to represent any system that is described by the same quantities. Consider the dimensionless term $(\pi_3)_{model} = (\pi_3)_{prototype}$.

Therefore,

$\frac{I_m}{l_m} = \frac{I_p}{l_p}$

$I_m = I_p(\frac{l_m^4}{l_p^4})$

where, $S = \frac{L_m}{L_p}$

Now, consider the dimensionless term $(\pi_1)_{model} = (\pi_1)_{prototype}$

$\frac{W_m}{E_m} = \frac{W_p}{E_p}$

$W_m = W_p(\frac{E_m}{E_p})$

$W_m = W_p * S_E$

where, $S_E = \frac{E_m}{E_p}$

Using the repeating variables *E* and *l* listed above, Table A.1 shows how selected variables are non-dimensionalized.

A.2 Buckingham *Pi* theorem for blast loading

Analysis using scaling laws can aid in determining the behavior of a structure from the response of a similar model that is scaled geometrically by a parameter α. Carrying out experiments on the full-scale model can be expensive and often dangerous if the experiments involve explosives. For example, to analyze the deformation of a wall under blast load, the

Table A.1

Similitude relations

Physical Parameters	Scale Factor
Length	S
Area	S^2
Volume	S^3
Linear Displacement	S
Moment of Inertia	S^4
Point Load	$S_E S^2$
Line Load	$S_E S$
Uniformly Distributed Surface Load	S_E
Stress	S_E

tests carried out on the full-scale article will be very expensive and complex. Hence, in such cases, experiments are done on a smaller-scale model and the results are interpreted based on a set of scaling laws that relate the model to the prototype.

The following section will illustrate the use of the Buckingham *Pi* theorem to derive a set of non- dimensionalized *Pi* terms for a structure subjected to a blast load. The deformation d experienced by a structure impacted by blast loading is dependent on the linear dimension L, stress or pressure σ, density ρ, energy e, velocity v, mass m, force F, and time t. The number of parameters $n = 9$, the number of fundamental dimensions $k = 3$. Hence, there will be $(n - k) = 6$ non-dimensional pi terms. For this case, Equation A.2 can be written in the following form

$$d = g(L, \sigma, \rho, e, v, m, F, t). \tag{A.11}$$

(L, σ, v) are picked as repeating variables that will be used to non-dimensionalize the others.

$\pi_1 = dL^a \rho^b v^c$

$\pi_1 = LL^a (\frac{FT^2}{L^{-4}})^a (\frac{L}{T^{-1}})^c$

$a = -1; b = 0; c = 0$

$$\pi_1 = \frac{d}{L} \tag{A.12}$$

$\pi_2 = \sigma L^a \rho^b v^c$

$\pi_2 = (\frac{F}{L^2}) L^a (\frac{FT^2}{L^{-4}})^b (\frac{L}{T^{-1}})^c$

$a = 0; b = -1; c = -2$

$$\pi_2 = \frac{\sigma}{\rho v^2} \tag{A.13}$$

$\pi_3 = eL^a \rho^b v^c$

$\pi_3 = FLL^a (\frac{FT^2}{L^{-4}})^b (\frac{L}{T^{-1}})^c$

$a = -3; b = -1; c = -2$

$$\pi_3 = \frac{e}{\rho v^2 L^3} \tag{A.14}$$

$\pi_4 = mL^a \rho^b v^c$

$\pi_4 = FT^2 L^- 1 L^a (\frac{FT^2}{L^{-4}})^b (\frac{L}{T^{-1}})^c$

$a = -3; b = -1; c = 0$

$$\pi_4 = \frac{m}{L^3\rho} \tag{A.15}$$

$\pi_5 = fL^a\rho^b v^c$

$\pi_5 = FL^a(\frac{FT^2}{L^{-4}})^b(\frac{L}{T^{-1}})^c$

$a = -2; b = -1; c = -2$

$$\pi_4 = \frac{f}{L^2v^2\rho} \tag{A.16}$$

$\pi_6 = tL^a\rho^b v^c$

$\pi_6 = TL^a(\frac{FT^2}{L^{-4}})^b(\frac{L}{T^{-1}})^c$

$a = -1; b = 0; c = 1$

$$\pi_6 = \frac{tv}{L} \tag{A.17}$$

The pi products displayed by Equations A.13 through A.17 are dimensionless. Based on this, the prediction equation given by Equation A.3 will result in the following equation:

$$\pi_1 = f(\pi_2, \pi_3, \pi_4, \pi_5, \pi_6). \tag{A.18}$$

Hence,

$$\frac{d}{L} = f(\frac{\sigma}{\rho v^2}, \frac{e}{\rho v^2 L^3}, \frac{m}{L^3\rho}, \frac{f}{L^2v^2\rho}, \frac{tv}{L}). \tag{A.19}$$

Assuming that the strain rate is constant Table A.2 shows how to scale selected variables using the repeating variables (L, σ, v) listed above.

Table A.2

Relationship between the model and prototype for the variables used in the current analysis.

Parameters	Scale Factor	Scale =1	Scale=2	Scale=4
Length (L)	α	1	2	4
Mass (M)	α^3	1	8	64
Stress (α)	1	1	1	1
Time (t)	α	1	2	4
Velocity (V)	1	1	1	1
Displacement (U)	α	1	2	4
Strain (ϵ)	1	1	1	1
Acceleration (A)	$\frac{1}{\alpha}$	1	0.5	0.25

A.3 Analytic verification of similitude relation

Consider a rectangular plate, with all edges fixed as shown in Figure A.1, loaded by a uniformly distributed w over the entire plate. The length of the plate L is 216 in, Young's Modulus E is $435.11e^{06}psi$, width b is 36in, and thickness t is 6 in subjected to a uniform load w of $10lbs$. Table A.3 shows the effect of scaling on parameters such as weight, maximum displacement, and maximum stress. The values of the constants α, β_1 can be obtained from Table 11.4 in Roark's formulas for stress and strain [136].

Table A.3

Analytical verification of similitude relation

Scale	Weight ρLbt	Maximum displacement $U_{max} = \frac{\alpha w b^4}{Et^3}$	Maximum stress $\sigma_{max} = \frac{-\beta_1 w b^2}{t^2}$
S=1	$\rho * (216 * 36 * 6) = \rho * 46656$	$\frac{\rho w}{E} * 7776$	$-\beta_1 w * 36$
S=2	$\rho * (432 * 72 * 12) = \rho * 186624$ $= \rho * 46656 * S^3$	$\frac{\rho w}{E} * 7776 * 2$ $= \frac{\rho w}{E} * 7776 * S$	$-\beta_1 w * 36$
S=4	$\rho * (864 * 144 * 24) = \rho * 2985984$ $= \rho * 46656 * S^3$	$\frac{\rho w}{E} * 7776 * 4$ $= \frac{\rho w}{E} * 7776 * S$	$-\beta_1 w * 36$

A.4 Numerical validation of similitude relation

The developed scaling laws are applied to a complex biological model. In the current research, the commercial software package Abaqus^{TM} [123] is used to perform computational mechanics experiments on the biological model of interest. The description of the model and analysis details follows in the subsequent sections.

A.4.1 Model description

The bio-structure of interest in the current study is rostrum of the paddlefish. An earlier feasibility study conducted on the rostrum led to the conclusion that the non-uniform geometry is a toughening mechanism used to mitigate failure [7, 29, 137]. Numerical experiments are carried out on the rostrum of paddlefish to study the effect of blast loadings on this complex bio-structure. In the two cases considered, the rostrum is scaled 2 and 4 times its initial size. Similitude theory is applied to scale the weight of the TNT utilized in the analysis. The parameters involved in the simulation are scaled based on Table A.1

and Table A.2. Figure A.2 shows the numerical model of the rostrum used in the current simulations. The length, width, and the thickness of the model are 275 mm, 80 mm, and 27 mm, respectively. Table A.4 gives details of the mesh used in the analysis.

Table A.4

Rostrum mesh details used in the numerical experiments

Rostrum Part	Element Type [123]	Element Shape	Geometric Order	Elements
Hard Cartilage	C3D8	Hexahedral	Linear	10943
	C4D4	Tetrahedral	Linear	303203
	Total nodes	105747		
	Total elements	314146		
Soft Cartilage	C3D8	Hexahedral	Linear	15745
	C4D4	Tetrahedral	Linear	146476
	Total nodes	53991		
	Total elements	162221		
Tissue	C3D8	Hexahedral	Linear	93024
	C4D4	Tetrahedral	Linear	850772
	Total nodes	303263		
	Total elements	943796		

A.4.2 Material property

Since the three components of the rostrum exhibit differences in material properties, the numerical model is constructed with a similar variation of material properties. These properties were determined from experimental nano-indentation studies carried out on the rostrum [121]. The three materials selected to represent the behavior of the components

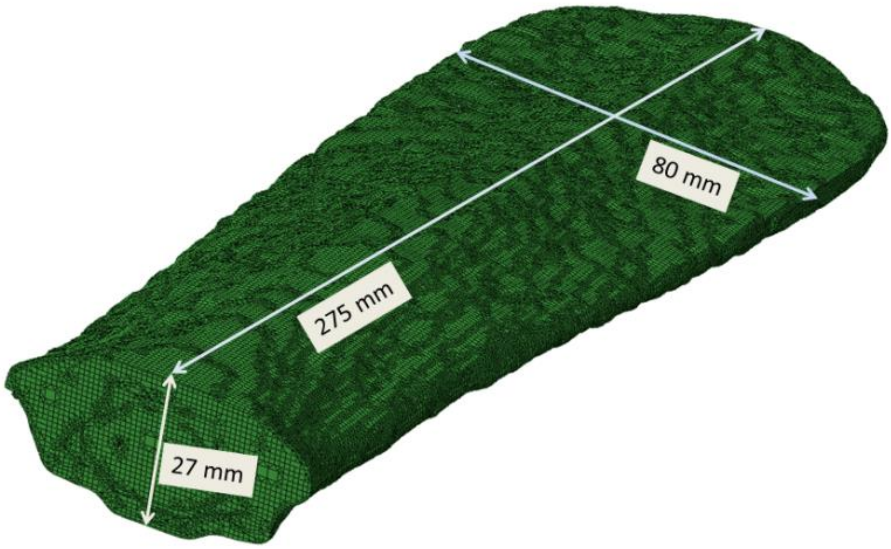

Figure A.2

Dimension of the rostrum.

of the rostrum are shown in Table A.5. Table A.6, Table A.7, and Table A.8 depict the material properties of the components of the rostrum model.

Table A.5

Materials used for component parts of rostrum.

Part	Material
Tissue	Vinyl ester Epoxy
Hard Cartilage	Polyethylene Fibers
Soft Cartilage	Polyethylene/Epoxy (as isotropic)

A.4.3 Force and displacement boundary conditions

The Abaqus/Explicit solver is used for performing the dynamic analysis. Three sets of numerical experiments are carried out on the rostrum. Table A.9 shows the details of the trinitrotoluene (TNT) weights and time durations of the numerical experiments performed in the current study. Displacement boundary conditions on the edges of the rostrum are fixed for all degrees of motion as depicted in Figure A.3. Fixed boundary conditions are chosen for the edges to hold the rostrum in a stationary position when it is under the influence of the shock wave from the blast load.

A.5 Numerical validation of scaling laws

The scaling laws are validated by comparing the values obtained from the numerical prototype and scaled models with the theoretically expected values from application of Buckingham Pi theorem. The displacement contours for the prototype and model are plot-

Table A.6

Vinyl ester epoxy for the Tissue component in rostrum

Commercial Name	Ashland Derakane 8084
Elastic Modulus	2.9 GPa
Elongation	8-10%
Ultimate Tensile Strength	76 MPa
Mass Density	1.14 g/cc

Table A.7

Polyethylene fibers for hard cartilage component in rostrum

Commercial Name	Honeywell Spectra Fiber S-900 5600
Elastic Modulus	66 GPa
Elongation	3.5%
Ultimate Tensile Strength	2.18 GPa
Mass Density	1 g/cc

Table A.8

Polyethylele /Epoxy (as isotropic) for soft cartilage component in rostrum

Commercial Name	Polyethylene/Epoxy (as isotropic)
E1	49,762 MPa
E2	1,470 MPa
G12	455 MPa
n12	0.27
Mass Density	1.05 g/cc
F1t	896.32 MPa
F1c	112.31MPa
F2t	4.19 MPa
F2c	4.19 MPa
F12	7.53MPa

Table A.9

Numerical experiment details.

Scale	Length of Rostrum (mm)	Weight of TNT (kg)	Time duration (Sec)	Distance between model and TNT (mm)
1	275	0.02	0.025	1000
2	550	0.16	0.05	2000
4	1100	1.28	0.1	4000

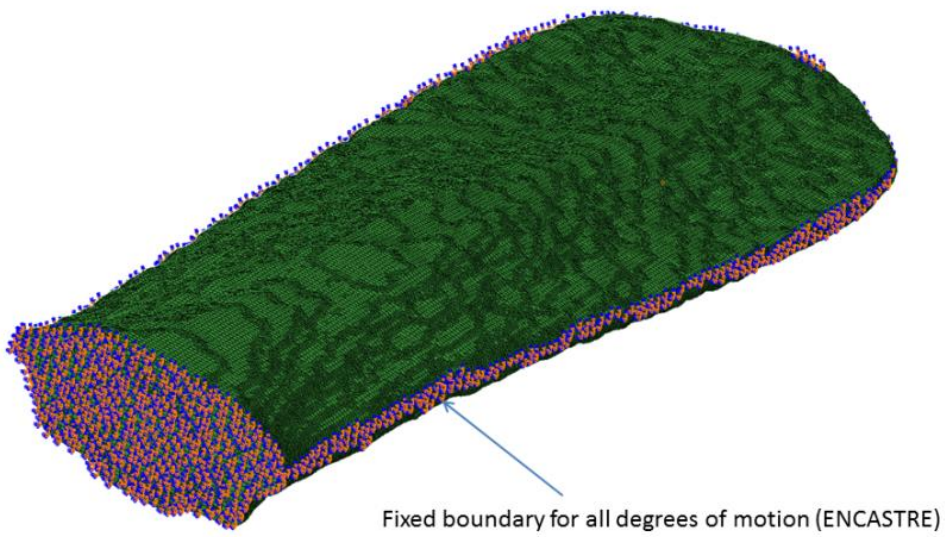

Figure A.3

Boundary condition on the rostrum

ted. Parameters such as displacement and stresses are used for comparison along vertical and horizontal axis of the rostrum. Also, nodal values of displacement, stresses, velocity, and strain are compared for estimating the percentage deviation from the values predicted from the scaling laws.

A.5.1 Displacement contours of the rostrum

Figure A.4 displays the non-dimensionalize displacement for the model and the prototype of the rostrum. Using the pi term from Equation A.12, the non-dimensional displacement is plotted. As seen from Figure A.4, displacement shows an identical trend for the prototype and scaled model. Since the rostrum has fixed-plate boundary conditions around all the edges, the center of the rostrum experiences maximum displacement. To further analyze the displacement trend, subsequent sections plot the non-dimensional displacement along the horizontal and vertical axis of the rostrum. The horizontal and vertical axis chosen for plotting the non-dimensional displacement in the subsequent sections pass through the region of the rostrum that is experiencing maximum displacement. The minor differences observed in the non-dimensional displacement in Figure A.4 may be attributed to the discretization error of the numerical scheme.

A.5.2 Displacement versus distance along horizontal and vertical axis of rostrum

Figure A.5 displays the non-dimensional displacement along the central vertical axis on the top surface of the rostrum. Displacements along the vertical axis of the rostrum are plotted as a function of distance for the prototype and scaled models. Since the rostrum is restrained along its edges, as shown in Figure A.3, zero displacement is observed in these

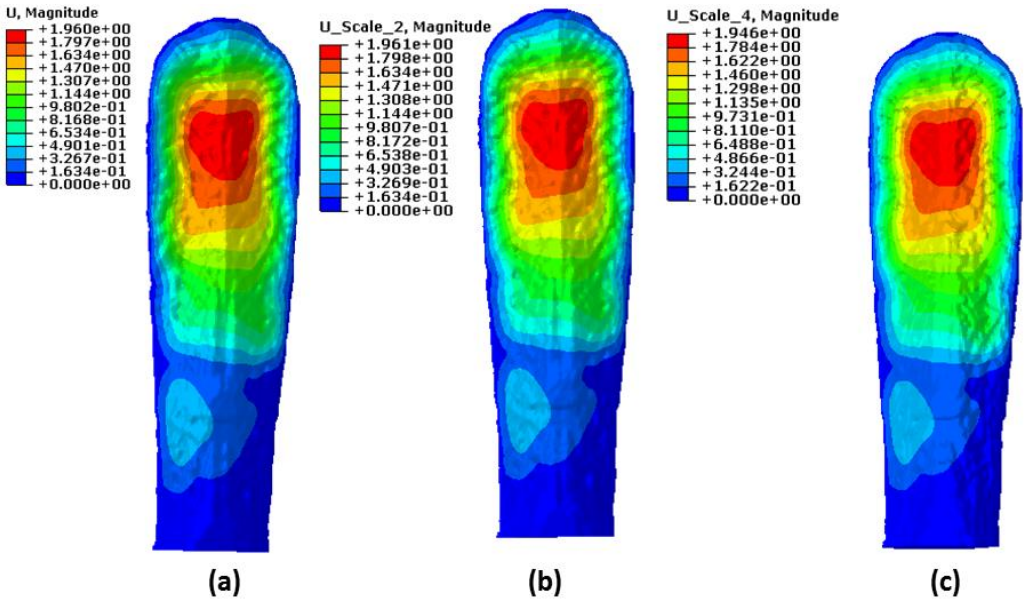

Figure A.4

Non-dimensional displacement on top surface of rostrum (a) prototype (b) model scale factor = 2 (c) model scale factor = 4

locations. For the models scaled to two and four times the original model dimensions, the displacement shows an identical trend along the vertical axis of the rostrum as displayed in Figure A.5. The maximum displacement is observed along the center of the rostrum. This may be because the center region is far from the restrained boundary conditions along the rostrum edges. As seen in Figure A.5, two peaks in displacement are observed at distances of approximately x=25 mm and x=50 mm from the tip of the rostrum. The restrained boundary condition on the rostrum edges may be influencing these maxima. A third peak is observed at approximately a distance of 110 mm from the tip of the rostrum, which also corresponds to the maximum displacement observed along the central vertical axis. This is because the point charge is placed in close proximity to this area. The displacement

steadily decreases along the vertical axis as displayed in Figure A.5. A very small peak is observed around x=250 mm distance from the tip of the rostrum. The center cartilage is stiffer in this region providing strength and rigidity, thus influencing the displacement.

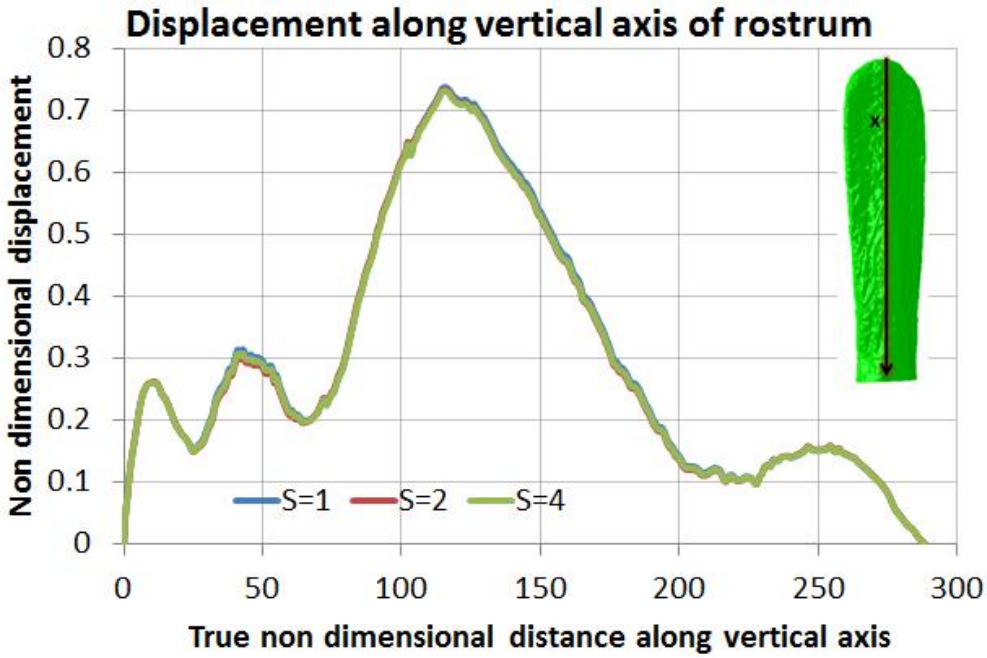

Figure A.5

Displacement versus true distance along vertical axis passing through the center of rostrum

The non-dimensional displacement shows a similar trend along the vertical axis of the rostrum for the prototype and scaled models as expected from the similitude theory. The scale factors used in the current analysis are S = 2 and S = 4, since the base model is scaled up to twice and four times its original size to analyze the applicability of similitude theory. Thus, the numerical simulation achieved the expected values as reflected by the Buckingham Pi theorem.

Figure A.6 shows the displacement along the horizontal axis of the rostrum located approximately 63.5 mm from the tip of the rostrum. This position was selected for the horizontal axis because maximum displacement was observed along this axis of the rostrum as depicted in Figure A.4. As before, the non-dimensional displacement is plotted along the horizontal axis of the rostrum for the prototype and the scaled models. The same displacement trend is observed in the rostrum prototype and scaled models. As seen in Figure A.6, zero displacement is observed along the edges of the rostrum owing to the restrained boundary condition. A peak is observed in displacement at a distance of 15 mm from the left edge of the rostrum. The displacement decreases as near the center bone of the rostrum at a distance of 40 mm from the left edge of the rostrum. It is observed that the center bone provides stability as indicated by the decrease in displacement. At x =70 mm, another displacement peak is observed. The two displacement peaks are observed near the region of the complex lattice architecture signifying that they are the major load bearing members. Therefore, the lattice architecture bears the load while the center bone provides stiffness/stability to the structural system.

A.5.3 Von-Mises Stress versus distance along horizontal and vertical axis of rostrum

Based on the similitude relations used for the current analysis, the stress should be the same for scaled models. Figure A.7 shows the Von-Mises stress along the center bone of the rostrum model used in the current study.

Identical values of stresses are obtained for the scaled model along the vertical axis of the rostrum when the rostrum is scaled to two and four times its original size. Also, the

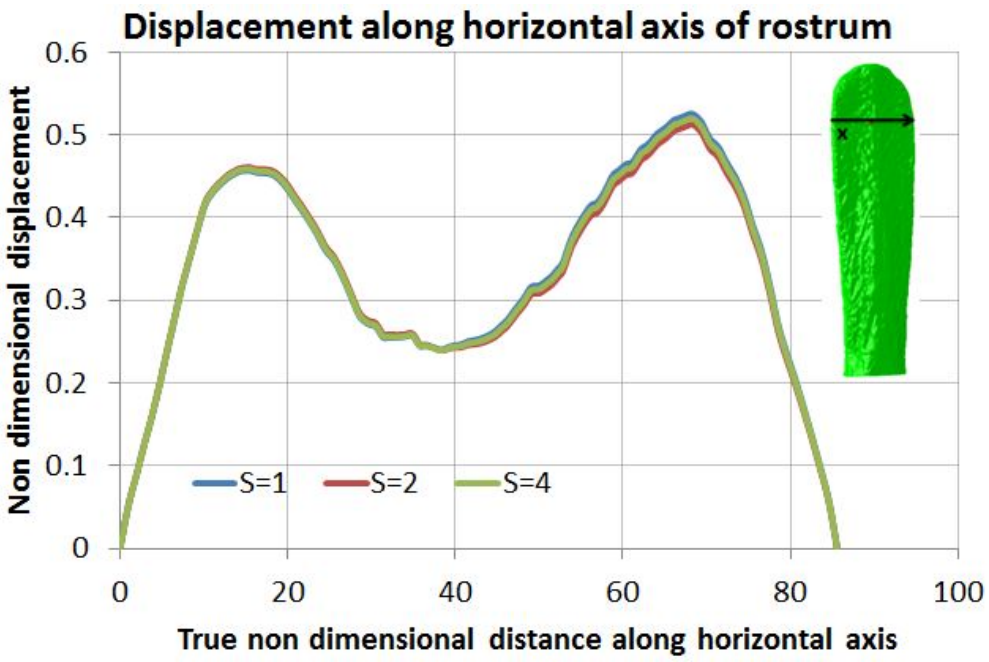

Figure A.6

Displacement versus true distance along horizontal axis of rostrum

stresses observed along the center bone of the rostrum have not crossed the yield stress represented by the purple line in Figure A.7.

Figure A.8 represents the Von-Mises stress along the horizontal axis of the rostrum. The stress pattern and value follows the laws of similitude for the prototype and both scaled cases. The material has reached yield stress in areas where the maximum displacement was observed. Owing to the unsymmetrical geometry of the rostrum, the load distribution exhibits an unsymmetrical distribution. The left side of the rostrum shows stresses reaching beyond the yield stress while the right side shows stresses well below the yield stress. Also, the center bone located between 30 mm and 60 mm shows a pronounced reduction in the

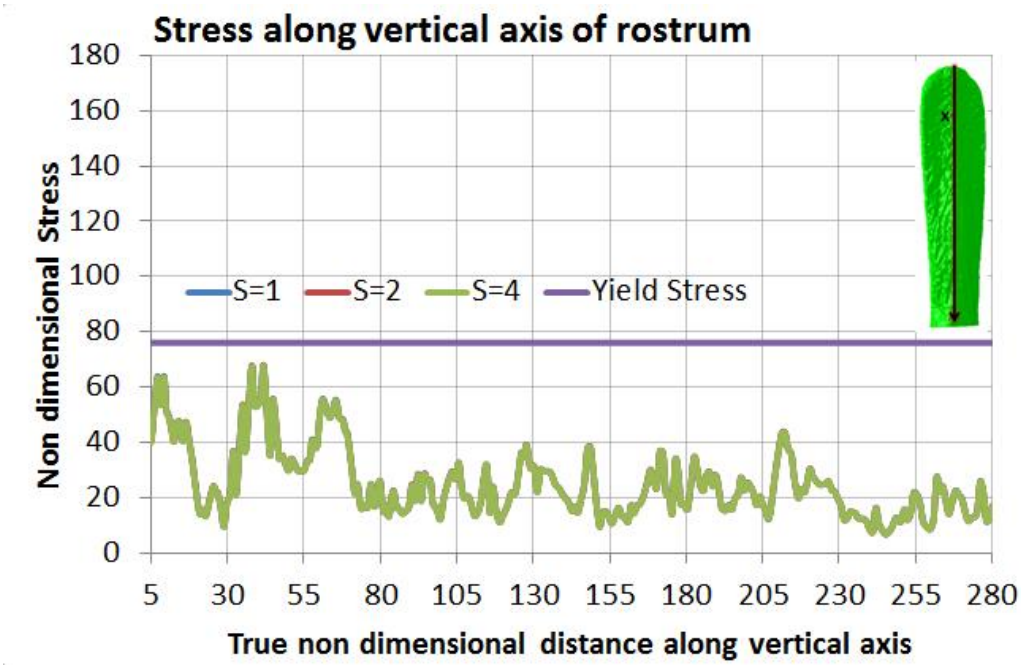

Figure A.7

Stress (MPa) versus true distance along vertical axis of rostrum

stresses. The center bone is pivotal in providing stability to the system and experiences a significantly lower stress level.

A.6 Comparison of scaling laws using numerical studies

Table A.10 and Table A.11 show the comparison of the values obtained from the scaling laws and the numerical studies conducted on the rostrum. A node on the top surface of the rostrum was selected to monitor. Since the TNT was placed 1000 mm away from the center of the rostrum, the center node shown in Figure A.9 was selected for comparing the scaling laws with numerical results. The numerical values for the same node are compared for the prototype and the scaled models. As seen in the comparison table the errors are

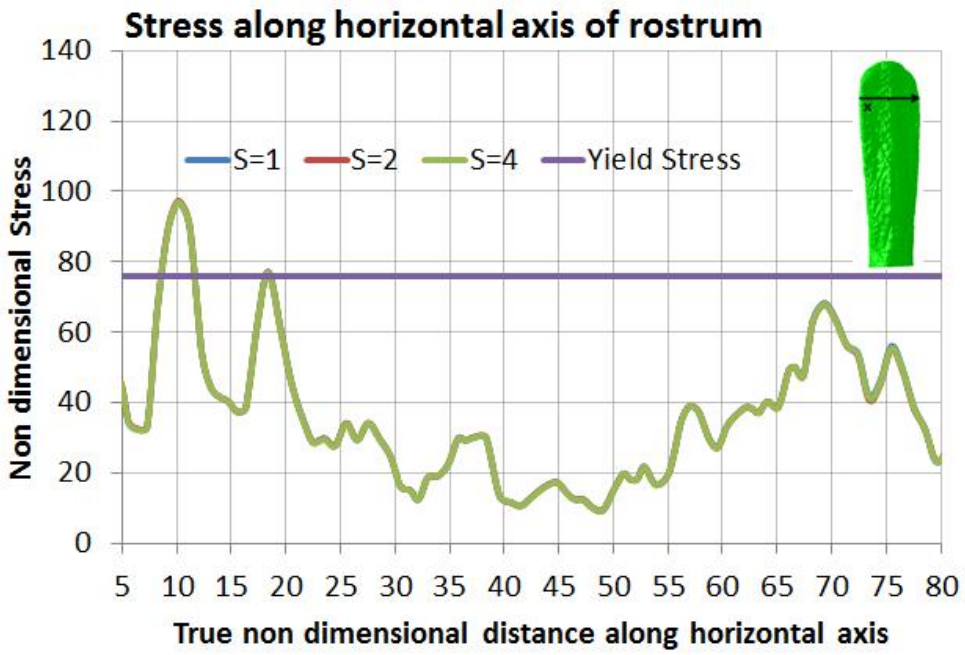

Figure A.8

Stress (MPa) versus true distance along horizontal axis of rostrum

within a maximum of 3.39% percentage. Hence, the numerical experiments have verified the similitude parameters identified by the Buckingham Pi theorem within a reasonably acceptable error range. The numerical errors may be the result of the discretization error involved in the scheme.

A.7 Conclusion

Similitude analysis can be employed to identify similarities in the behavior of models at different scales. The current research has demonstrated that deformation of a structure due to blast impact can be represented in terms of dimensionless pi terms by application of the Buckingham Pi theorem. This study presents the development of similitude re-

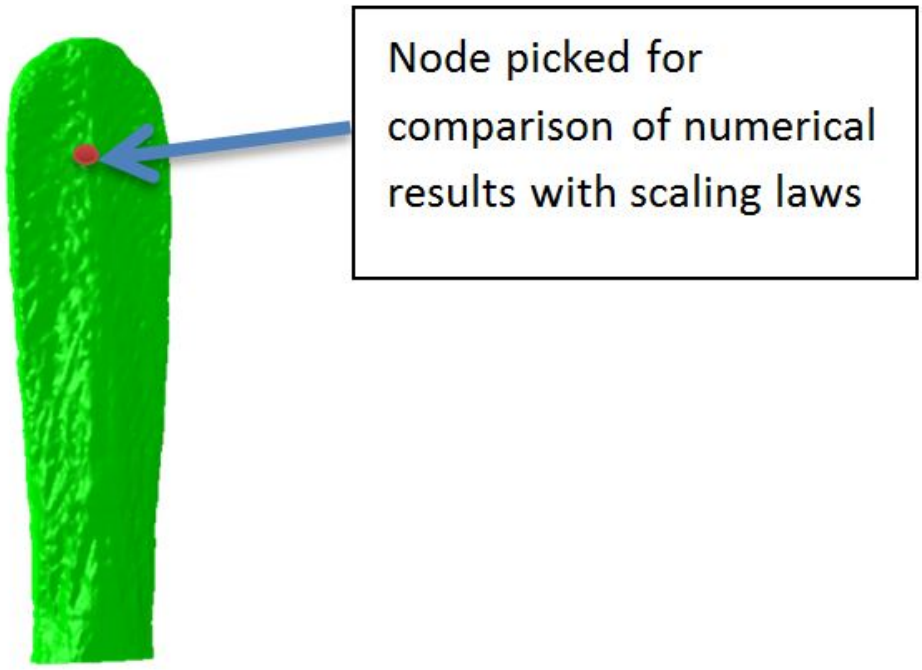

Figure A.9

Node picked for comparison of numerical results with scaling laws

Table A.10

Comparison of physical parameters obtained from scaling laws and numerical experiments on the rostrum between prototype and model scaled by a factor of 2

Prototype		Scaled model (S=2)		Percentage Error
		From Scaling Laws	From numerical experiment	
Von Mises stresses in MPa	21.9543	21.9543	22.0979	0.6541
Maximum principal stresses in MPa	0.618881	0.618881	0.601492	2.8097
Spatial displacement in mm	1.92884	3.85768	3.86485	0.1859
Spatial velocity in mm/s	514.26	514.26	507.276	1.3581
Logarithmic strain in mm/mm	0.00250712	0.00250712	0.00251508	0.3175

Table A.11

Comparison of physical parameters obtained from scaling laws and numerical experiments on rostrum between prototype and model scaled by a factor of 4

Prototype		Scaled model (S=4)		Percentage Error
		From Scaling Laws	From numerical experiment	
Von Mises stresses in MPa	21.9543	21.9543	22.0753	0.5511
Maximum principal stresses in MPa	0.618881	0.618881	0.597848	3.3986
Spatial displacement in mm	1.92884	7.71536	7.66811	0.6124
Spatial velocity in mm/s	514.26	514.26	506.477	1.5134
Logarithmic strain in mm/mm	0.00250712	0.00250712	0.00251336	0.2489

lationships for a simple system where the solution is known to verify the application of similitude approach. Numerical experiments were carried out on the rostrum of the paddlefish to demonstrate the development and application of similitude laws for blast loading for complex structural models. From the analysis presented, it is evident that deformation, stress, velocity, and strains have been successfully scaled within a reasonably acceptable error range. The strategy presented in this study can be employed to develop and apply similitude relations through the application of Buckingham Pi theorem.